NASA Technical Memorandum 104606, Vol. 12

Technical Report Series on Global Modeling and Data Assimilation

Max J. Suarez, Editor
Goddard Space Flight Center
Greenbelt, Maryland

Volume 12

Comparison of Satellite Global Rainfall Algorithms

Alfred T. C. Chang
Long S. Chiu
Goddard Space Flight Center
Greenbelt, Maryland

National Aeronautics and
Space Administration

Goddard Space Flight Center
Greenbelt, Maryland
1997

This publication is available from the NASA Center for AeroSpace Information,
800 Elkridge Landing Road, Linthicum Heights, MD 21090-2934, (301) 621-0390.

Abstract

Seventeen months of rainfall data (August 1987–December 1988) from nine satellite rainfall algorithms (Adler, Chang, Kummerow, Prabhakara, Huffman, Spencer, Susskind, and Wu) were analyzed to examine the uncertainty of satellite–derived rainfall estimates. The variability among algorithms, measured as the standard deviation computed from the ensemble of algorithms, shows regions of high algorithm variability tend to coincide with regions of high rain rates. The ratio of the annual mean algorithm variability to the annual mean (August 1987–July 1988) rain rate is generally less than 0.5 over most of the regions between 50°N and 50°S. Exceptions are found in the oceanic dry zones and the Himalayan region. High algorithm variability in the oceanic dry zones points to the different approaches in the treatment of low rain rates. Arkin's algorithm, which uses cloud top temperature, tend to over–estimate in the mountainous Himalayas and in the Indian monsoon region. The over-estimate over the Himalayas is attributed to the cold surface. Over the Indian Ocean, the frequent occurrence of non-raining high clouds contributed to the high estimates. The global annual rainfall (over the latitude belts ±50° and for August 1987–July 1988) ranges from 2.5 to 3.5 mm/day, with higher variability over land than over ocean. The variability of zonal averaged rain rates is in the range of about 0.5 mm/day in the subtropical dry zones and increases to 2 mm/day in the tropical rain belts. Histograms of pattern correlation (PC) between algorithms suggest a bimodal distribution, with separation at a PC value of about 0.85. Applying this threshold as a criteria for similarity, our analyses show that algorithms using the same sensor or satellite input tend to be similar, suggesting the dominance of sampling errors in these satellite estimates.

The sensitivity of the algorithms to the 1986–87 El Niño Southern Oscillation event was examined using paired-t tests and PC analyses. Paired-t statistics results indicate that the algorithms of Chang, Prabhakara, and Spencer show significant difference between August 1987 and 1988, assuming the difference field is spatially uncorrelated. This assumption needs to be further examined.

Contents

List of Figures

List of Tables

1 INTRODUCTION

The reality of Global Circulation Models (GCMs) to predict future climate changes hinges on their ability to realistically reproduce current climate. Although most of the GCMs are based on the same laws of thermodynamics and dynamics, they emphasize different physical processes or used different parameterization schemes for many of the important climate components. The Atmospheric Model Intercomparison Project (AMIP) was established to evaluate the operational GCMs and to diagnostically compare products of the GCMs. Ten years (1979-1988) of GCM runs were performed in a controlled situation for the cases with and without actual sea surface temperature forcing.

Precipitation is an important climate parameter. Theoretical studies have shown the importance of the release of latent heat of condensation associated with precipitation in driving atmospheric circulation. Observational studies have also demonstrated the association between precipitation pattern changes and climate variations. However, the spatial and temporal variability of rainfall at all scales poses a great challenge in estimating space/time rainfall.

In response to this challenge, the National Aeronautics and Space Administration (NASA) of the United States (U.S.) and the National Space Development Agency (NASDA) of Japan jointly sponsored the Tropical Rainfall Measuring Mission (TRMM). With TRMM well underway, the science community saw the opportunity for improved global rainfall estimation. Techniques for estimating rainfall from space-borne measurements flourished. To compare and calibrate these techniques, a number of projects to intercompare satellite rain retrieval techniques have been conducted. The First Algorithm Intercomparison Project (AIP-1) was organized by the Global Precipitation Climatology Project (GPCP). AIP-1 compared a variety of rainfall estimates derived from geostationary meteorological satellite visible and IR observations and Special Sensor Microwave/Imager Microwave (SSM/I) observations with rainfall derived from a combination of surface radar and rain gage data over the Japan and the adjacent sea region during June and mid-July through mid-August of 1989 (Lee et al., 1991). Subsequently, AIP-2 and AIP-3 were organized to evaluate the rainfall over England and the Tropical Ocean-Global Atmosphere Coupled Ocean Atmosphere Response Experiment (TOGA-COARE) region respectively. Under the NASA- led WetNet Project, a series of Precipitation Intercomparison Projects (PIPs) were organized to compare rainfall derived from a common SSM/I microwave data set. PIP-1 was undertaken in 1992 and 1993, with global rainfall for the months of August through November 1987 as its subject (Barrett, 1994). PIP-2 (Smith et al., 1995) and PIP-3 (Ebert, 1996) were organized to evaluate and compare SSM/I derived rainfall for pre-selected rainfall cases and global patterns. These intercomparison activities were designed to fulfill specific goals and were usually restricted to a limited domain.

There are several ongoing satellite rain estimation activities at NASAs Goddard Space Flight Center (GSFC). At the request of GSFC management, an in-house ad hoc committee

was formed in October 1993. The main charters of this committee were to: (1) review and evaluate the GSFC satellite rain estimation efforts, (2) discuss duplications and/or need for diversity, and (3) develop a plan for coordinating the GSFC efforts, including an intercomparison of the algorithms at various space and time scales. This study extended the comparison effort to include other operational or semi-operational rain rate algorithms.

Algorithm developers were requested to submit monthly data for the comparison effort. Two types of comparison were conducted: snapshot comparison and time series comparison. The snapshot comparison focuses on the global rain estimates for the months of August 1987 and May 1988. The time series comparison focused on the time period during which the SSM/I measurements overlap the AMIP period (July 1987 through December 1988). During this period, the algorithms went through at least one seasonal cycle, allowing examination of the seasonal differences of the algorithms. This period also saw the demise of the 1986-1987 El Niño Southern Oscillation (ENSO) episode and the return of the atmosphere to its relatively normal state. This provided the opportunity to intercompare the sensitivity of the algorithms to the same external forcing.

The remainder of this report is divided into 5 sections. Section 2 describes the algorithms. Section 3 describes the preprocessing of these data sets. Results of the comparison of the annual mean, seasonal and regional differences, and for individual months (August 1987 - July 1988) are described in Sections 4. Section 5 examines the responses of the algorithms to the 1986-87 ENSO event. Section 6 summarizes the results and discusses possible mutually beneficial avenues of collaborations between the algorithms.

2 ALGORITHMS

The satellite rain algorithms included in this study are:

(1) The Goddard Scattering Algorithm by Adler, Huffman and Negri (Adler),

(2) Calibrating GOES Precipitation Index (GPI) infrared (IR) data with microwave data by Adler, Huffman and Negri (Huffman),

(3) Monthly oceanic rainfall using SSM/I brightness temperature histogram by Chang, Chiu and Wilheit (Chang),

(4) Theoretical regression method by Kummerow (Kummerow),

(5) Precipitation area dependent technique by Prabhakara (Prabhakara),

(6) GOES Precipitation Index (GPI) Technique by Arkin (Arkin),

(7) Oceanic rainfall from Microwave Sounding Unit (MSU) by Spencer (Spencer),

(8) Global precipitation from TIROS Operational Vertical Sounder (TOVS) by Susskind (Susskind) and

(9) Multi-spectral rainfall algorithm by Wu (Wu).

In addition, the gridded gauge rainfall data set prepared by the Global Precipitation Climatology Center (GPCC) (Rudolf et al., 1994) was included for validation over land.

The characteristics of these algorithms are summarized in Table 1. The algorithms are described below.

2.1 GSFC Scattering Algorithm, Adler, Huffman and Negri (Adler)

This algorithm is based on the technique described by Adler et al. (1993). The first step is the screening of SSM/I data for missing and physically unrealistic data and jumps in scan-average values. The SSM/I brightness temperatures are then interpolated to 12.5 km resolution pixels. Pixels that are unlikely to precipitate are identified and screened out. The remaining pixels are tested for the scattering signal at 85.5 GHz due to frozen hydrometeors. A precipitation rate is calculated based on radiative computation using numerical cloud model results (Adler et al. 1991). The relationship they derived is:

$$T_b(85.5V) = 251.0 - 4.19R, \tag{1}$$

where $T_b(85.5V)$ is the SSM/I brightness temperature of the vertically polarized 85.5 GHz channel, and R is the rain rate in mm/hr. A rain/no-rain cutoff was set at 1 mm/hr ($T_b = 247K$). The cutoff is applied to each individual SSM/I pixels. However, no cutoff is applied to subsequent averages. Comparison with rain gage data collected over the Pacific atolls (Morrissey, 1991) showed that the rain rate derived from (1) consistently underestimated precipitation by a factor of two over the atolls, so the slope in (1) was adjusted for oceanic regions to yield:

$$T_b(85.5V) = 251.0 - 2.09R \tag{2}$$

while keeping the same rain/no-rain cutoff. In coastal regions, the slope is an average of the land and ocean value. In the areas where sea ice is possible, land value is used.

2.2 Calibrating Geostationary IR Data with Microwave Data, Adler, Huffman and Negri (Huffman)

This method takes advantage of the frequent temporal sampling by the geostationary satellite (8 times per day) and the physically based microwave rain signal by the Defense Meteorological Satellite Program (DMSP) SSM/I (twice per day) (Huffman et al., 1993). Coincident SSM/I and geostationary IR data are compared to derive an IR-rain rate relationship consistent with the microwave-inferred rain rate. It is assumed that these microwave calibrated IR-rain rate relationships vary slowly in space and time. The calibrated IR-rain rate relationships are then applied to all the geostationary satellite data to take advantage of the superior IR time sampling. At present, the microwave rain estimates are based on the 85.5 GHz measurements of the SSM/I. The algorithm can, however, accommodate any rain estimates derived from microwave techniques if they are deemed to be superior.

2.3 GOES Precipitation Index (GPI) Technique (Arkin)

The GPI technique (described in detail in Arkin and Meisner, 1987) was developed over the Global Atmospheric Research Program Atlantic Tropical Experiment (GATE) domain in the Atlantic Inter-tropical Convergence Zone (ITCZ) region west of the African continent. From linear regression analyses between cloud-top temperature as inferred from satellite IR data, and radar derived rainfall, a linear relationship between the fraction of high cloud as inferred from IR histogram and rain rate is established. The method is a simple cloud-top temperature thresholding algorithm that assumes that satellite pixels with IR equivalent blackbody temperatures at or below 235K precipitate at a constant rainfall rate of 3 mm/hr, and pixels warmer than 235K do not precipitate. Although the GPI was developed exclusively over the GATE region, the technique has been applied to satellite data over the entire global tropics (40°N-40°S).

2.4 Probability Distribution Functions Algorithm, Chang, Chiu and Wilheit (Chang)

This algorithm is used to derive the oceanic monthly SSM/I rainfall estimates for the GPCP. It is based on a plane parallel radiative transfer model for the 19 and 22 GHz radiance (Wilheit et al., 1991). A Marshall-Palmer rain drop distribution was assumed, and water vapor and non-raining cloud are also included in the model. However, frozen hydrometeor and surface wind speed are excluded. An analytic function of the rain rate and brightness temperature (R-Tb relationship) is obtained based on radiative transfer calculations.

Monthly histograms of brightness temperatures and linear combinations of brightness temperatures are collected over 5° x 5° grid boxes. The probability distribution of the rainfall

is assumed to follow a mixed log-normal distribution. Using the $R - T_b$ relationship, the mixed log-normal rainfall distribution is transformed into an expected brightness temperature histogram. The parameters of the log-normal distribution are obtained by adjusting the fitting parameters of the expected histogram to the observed histogram. The freezing height, which is needed for converting the brightness temperature to rain rates, is estimated from the Tb (19V) and Tb (22V) histograms by an objective technique using the $R - T_b$ relationships.

No empirical calibration has been applied to this data set. The principal parameter that needs to be studied is a beam-filling correction factor. The beam filling correction factor depends on the $R - T_b$ relationship and the spatial variance of the rain fields (Chiu et al., 1990). At present, an empirically derived correction factor of 1.5, estimated from observed radar rain rates, is applied to the entire data set.

2.5 Linear Regression Algorithm (Kummerow)

This algorithm makes use of an inversion technique based on theoretically calculated relationship between rainfall rates and SSM/I brightness temperatures. The algorithm uses 18 convective and 9 stratiform distinct rain structures. These structures, which are based primarily on dynamic cloud model output, consist of five vertical layers. Hydrometeor distributions in each of the layers are specified based on the surface rainfall rate. Potential errors introduced into the theoretical calculation by the unknown vertical distribution of hydrometeors are minimized by explicitly accounting for the diverse hydrometeor profiles. Detail descriptions of this algorithm can be found in Kummerow et al. (1989) and Kummerow and Giglio (1994).

One unique feature of the cloud structures is the fact that hydrometeor contents are not assumed uniform over a given cloud structure. This is necessary to avoid the classical beam-filling problem. To account for the variability within each retrieved pixel (50 km), the 85.5 GHz variability is used as a proxy indicator for the true variability. The proxy indicator is defined as the standard deviation of the 85.5 GHz measurements divided by the mean rainfall within a given pixel. Rainfall is then assumed to be log-normally distributed with a standard deviation that is consistent with the 85.5 GHz measurements.

Due to the strong dependence of the upwelling radiance on the vertical distribution of hydrometeors, the retrieval algorithm selects the optimal structure from among the 27 cloud structures. This is accomplished by comparing the observed and calculated brightness temperatures at all frequencies and polarizations. The vertical structure and rainfall rate which produces the smallest brightness temperature deviations in the root mean square (rms) sense is selected as the optimal solution for any given pixel.

2.6 Rain Area Dependent Algorithm (Prabhakara)

SSM/I data were used to develop a model to discriminate heavy convective and light stratiform rain in mesoscale convective systems. Weather radar data from Japan and Florida were used to calibrate this model. This discrimination is done on the basis of the packing of rain cells in the field-of-view of the radiometer. From the SSM/I data, it is inferred that strong convective rain cells normally associated with downdrafts and/or entrainment produce relatively large "holes" or clearances between cells. This leads to a loose packing of rain cells of a few kilometers in size in a large radiometer footprint. Clouds with diffused cell structure appear to produce uniform light rain. This model is used to determine the effective rain area over oceans. The effective rain areas are then related to the area averaged rain intensity empirically. Monthly rainfall maps using the Scanning Multi-channel Microwave Radiometer (SMMR) and SSM/I data have been produced at a resolution of 3° latitude by 5° longitude.

2.7 Oceanic Rainfall from MSU (Spencer)

The Spencer algorithm for oceanic rainfall is based on observations of the Microwave Sounding Unit (MSU) onboard the TIROS-N series of NOAA polar orbiting satellites. The MSU measures the microwave radiance at 4 frequencies in the 50-70 GHz oxygen absorption band. Although the instrument was designed primarily to measure atmospheric temperature profiles, rain and cloud signals within these frequencies were exploited. The 50.3 GHz channel has the least atmospheric absorption and approaches a window channel measurement such as the 37 GHz channel of the SSM/I. The rain rate is assumed to be proportional to the brightness temperature warming above a threshold. The algorithm is calibrated by comparing 7 to 10 years of monthly rainfall records at 122 island and coastal locations at both high and low latitudes and in both hemispheres. Detailed descriptions of this algorithm are given by Spencer (1993).

2.8 Global Precipitation from TOVS (Susskind)

This technique is primarily based on a relationship between cloud volume and rain rate (Susskind et al., 1984). Products from the TOVS sounding retrievals are used. The retrieval provides global coverage of geophysical parameters at 60 km spatial resolution twice per day. The retrieved data is potentially useful for initialization of general circulation models as well as climate studies. Currently the algorithm estimates precipitation based on the cloud top pressure, effective cloud fraction, and temperature-humidity profile with a nominal 60 km resolution. Empirically obtained proportionality constants have been developed for different seasons and different surface types (land or water) (Susskind and Pfaendtner, 1989) by comparisons with rain gage data for 1979. Production of a 16 year TOVS global data

set has begun as part of the Pathfinder activity. Different empirical coefficients may have to be generated to relate precipitation to sounding data from different satellites.

2.9 Multi-spectral Rainfall Algorithm (Wu)

Wu's (1991) rainfall algorithm is based on cloud top altitude, emissivity, cloud amount, and diurnal variation of surface temperature derived from TOVS sounding data. It uses long-wave cloud radiative forcing (LCRF) together with the difference between day-time and night-time clear sky outgoing long-wave radiation (DCLR). A linear relationship between rainfall (rain gage data over land) and LCRF and DCLR is established. The correlation coefficient between the rainfall estimates and gage data for 4°latitude by 5° longitude boxes is 0.8. Global ten-day and monthly mean rainfall maps have been produced for 1979 and 1980. Multi-year (1979-1995) rainfall estimates will be produced in the coming years using results generated from the TOVS pathfinder activities.

As part of the GPCP, the Global Precipitation Climatology Center (GPCC) is responsible for assembling rain gauge data over land (Rudolf et al., 1994). The GPCC data were included for comparison over land.

3 DATA PRE-PROCESSING

Table 2 shows the data available from each algorithm. There are substantial missing data in the SSM/I radiance for December 1987, hence that month is missing for algorithms using SSM/I as input. Due to the evolutionary nature of some of these algorithms, data sets are often updated after they are first acquired for our analysis. For example, a revised version of Spencers data set came into existence in the middle of our analysis. The newer version has been used in comparison with GCM results (Lau et al., 1996) and was used in our comparison study. Since this change, the data sets for our comparison study have been frozen.

These rain rate data sets have different spatial and temporal resolutions. Some of the algorithms have produced pentad (five day) data and monthly means were derived by averaging the pentad data. There are six pentads for all the months except August when the monthly mean is the average of seven pentads. Other algorithms have used calendar months. For comparison purpose, the data are resampled to the lowest spatial resolution of the data sets (5° by 5°) without area weighting. For example, Prabhakara's data has a resolution of 3° latitude by 5° longitude, hence latitudinal weights of [3,2], [1,3,1], or [2,3] were used where appropriate. All units are converted to mm/day by dividing the monthly mean by the appropriate number of days in the month. This reduces the mismatch for data sets using pentad and calendar month.

While most of the algorithms are applicable over both land and ocean, some are ocean-specific algorithms. To compare the performance over land and ocean, a land-sea mask, with 5° by 5° resolution, was created. Statistics are computed for oceanic and land areas, respectively. The ocean is further divided into three ocean sectors: Atlantic, Pacific, and Indian Ocean. Land areas are divided into five land masks: North America, South America, Eurasia, Africa, and Australia. Figure 1 shows the land-sea mask used in this study.

We first pre-screened the data by computing the histograms of the rain rates. Data points of unrealistically high values occur in most of the SSM/I algorithms. Inspection showed that these pixels may be contaminated by land or islands. Hence, all rain rates with values greater than 30 mm/day are screened out and assigned a missing value. The maximum and minimum rain rate, the rain rate histograms, and the number of data points screened out are listed in Appendix A. In general, one to two data points are screened out by this procedure each month for most SSM/I-based algorithms. The number of data points screened out is much less for other algorithms. In examining the mean fields, a large jump across the 50°S latitude was noted. This may be due to the 50° boundary for most algorithms.

The number of data points screened out from Kummerow's algorithm is generally higher than average. We also noted that unrealistically high rain rates occur over the Himalayas. Only oceanic rain rates from Kummerow's algorithm were included in our comparison.

4 COMPARISON RESULTS

4.1 Annual mean (August 1987 - July 1988)

The annual mean (August 1987 - July 1988) rain rate distributions for each algorithms were computed. The upper panel of Figure 2 shows the annual mean rain rate averaged over all algorithms. The annual mean map shows all the major features of the global precipitation field: Inter-tropical Convergence Zone (ITCZ), South Pacific Convergence Zone (SPCZ), South Atlantic Convergence Zone (SACZ), Monsoon regions, mid-latitude storm tracks, and major rain areas in the Amazon and equatorial Africa. The oceanic dry zones in the Atlantic and Pacific are also evident. There is a rain band in the southern mid-latitudes (30°-60°S), and a sudden decrease at about 50°S which is due to the difference in the number of algorithms across this boundary.

The standard deviation (SD) averaged over the algorithms for the annual mean is depicted in the middle panel of Figure 2. Areas of high SD tend to coincide with high rain rate areas. There is a region of high SD in the Himalayas region. The high SD in this region is attributed to high rain rate estimates from Arkins algorithm during the northern winter months, as demonstrated later in Section 4.4.

The ratio of SD to the mean is shown in the lower panel of Figure 2. Over the oceans, this

ratio is less than 0.5, except in the oceanic dry zones. There is a jump in the ratio across the 50°S boundary, which is probably due to the sudden decrease in the mean across the boundary (see upper panel).

Figure 3 shows the algorithm with the maximum (upper panel) and the minimum (lower panel) rain rates. Algorithms with the maximum rainfall tend to orient in the zonal direction. Arkins algorithm display the largest rain rate in most land areas and in the Indian Ocean, while Prabhakara's rain rate is the highest in most of the oceanic regions. Wu's rain rate is the highest over the oceanic dry regions. The lower panel of Figure 3 shows the algorithms of minimum rain rate. Kummerow's is the lowest in most of the tropical ocean area. Prabhakara's also reveals the minimum in the 40°-50°S latitude band. Poleward of 50°, where only algorithms of Adler, Kummerow, Susskind, and Wu have coverage, Adler and Wu's algorithm display the minimum in the southern and northern hemisphere, respectively.

4.2 Monthly Comparison

Figures 4.1-4.17 show the mean (averaged over all algorithms), SD, and the ratio of SD to the mean for August 1987 to December 1988.

In August 1987 (Figure 4.1), all algorithms show the major patterns of precipitation: ITCZ, SPCZ, and the oceanic dry areas in the western north Atlantic and south Pacific. Over land, the maximum over the Amazon, equatorial Africa, and over the Indian continent are evident. The maximum and minimum intensities at the location of the maximum and minimum are quite varied, however. The dry oceanic regions show the largest ratios. This is probably due to the small rain rates over these regions and the deficiency in some algorithms in estimating the low rain rates. Again, as in the annual mean case, the regions of high SD correspond generally to regions of high mean rain rate. The ratio in the range of 0.5. in most areas.

The upper panel of Figure 5.1 shows the algorithm which produces the maximum rain rate at each grid point for August 1987. Arkins algorithm displays the largest rain rate over the Indian continent and northern Indian Ocean. This is consistent with earlier results of Chiu et al. (1993) who attributed the high rain rates to the presence of non-precipitating high cirrus in these areas. Arkin's rain rate is also the maximum in Africa between the latitudes of 10°S to 20°N, and in most of the latitude band between 35°S to 40°S. In the oceanic dry regions, such as the eastern north and south Pacific, and western south Atlantic, Wu's algorithm shows the maximum. The high variability may be due to the use of cloud radiative forcing in Wu's algorithm and the low cutoff threshold imposed in some microwave algorithms. Most of the algorithms are confined to latitudes of 50° -60° latitude. Poleward of 60° latitude, algorithms of Adler, Susskind, and Huffman show the maximum rain rate.

The lower panel of Figure 5.1 shows the algorithm that produces the minimum rain rate for

August 1987. Adler and Kummerows algorithms are the minimum in most of the regions between 60°N and 60°S. At the 45°-50°S latitude band, Prabhakara's is the minimum. Poleward of 60° latitude, Wu's algorithm is the minimum.

In September 1987 (Figure 4.2), streaks of large rainfall areas, oriented in a north-south direction, are seen in the north Pacific. These large rainfall areas are associated with typhoon tracks. The corresponding SD is also high. Figure 6 shows the rainfall distribution for all nine algorithms. SSM/I-based algorithms generally have the largest rain rates in the typhoon track areas, followed by the algorithms of Arkin and Spencer. The algorithms of Susskind and Wu also show streaks of high rain rate areas associated with the typhoon tracks, but the rainfall intensity are lower than other algorithms. The lower panel of Figure 6 shows the ratio of the SD to the mean rain rate. Large ratios appear south of the equatorial rain band and in the oceanic dry zones.

Over the Himalayan region the ratio is high in general. The ratio reaches a value above 2 in October 1987 (Figure 4.3) and remains high till June 1988.

We examined the similarity between the different algorithms. Table 3 shows the pattern correlation coefficients (PCs) between the different algorithms for August 1987. All coefficients greater than 0.85 were highlighted. The PCs range from 0.6 to 0.95. Figure 7 shows the histogram of the PCs for August 1987. The histograms suggests a bi-modal distribution, with peaks around 0.75 and 0.90. If we consider a PC value of 0.85 as a threshold for similarity, i.e., algorithms with PC higher than 0.85 are similar, then the algorithms tend to cluster. For example, there is similarity between the algorithms of Huffman, Adler, Chang, and Kummerow, all of which use SSM/I data as input. The highest correlation of 0.94 is found between Susskind and Wu, which are based on TOVS retrieved parameters. There is also a high PC between Arkin's and Huffman's algorithm, which may be due to the incorporation of GPI data in Huffman's algorithm. Spencer's algorithm, which is the only one using MSU data, has no PC values greater than 0.85 with any of the other algorithms. This pattern suggests that algorithms that use the same sensor data (SSM/I or MSU) or retrieved parameters (TOVS) tend to be similar. The reason for this similarity may be due to the error inherent in these algorithms. There are essentially two kinds of errors in satellite retrieval algorithms: retrieval and sampling error(Wilheit, 1988). The above result indicates that the rainfall pattern derived from these retrieval algorithms are extremely dependent on the sampling of the sensors.

To ascertain that our results are not fortuitous, we repeated the computation for May 1988. Table 4 shows the PCs between the algorithms for May 1988. The histogram of correlation coefficients are also shown in figure 7. If we again impose a PC threshold of 0.85 as a criteria for similarity, similar conclusion to the August 1987 analysis can be reached.

There is a general degradation of the pattern correlation between Huffmans algorithm and the other algorithms in 1988. Figure 8 shows the rain fields for all nine algorithms for April 1988. Huffmans algorithm shows a very strong precipitating region in the equatorial Indian

ocean which is not present in other algorithms except that of Arkin.

4.3 Zonal Means

Zonal mean rain rate for all algorithms were computed for the annual mean, August 1987, and May 1988. The results are presented in Figures 9-11. Figure 9 shows the annual zonal means over ocean (upper panel), over land (middle panel), and over both land and ocean (lower panel). The variability over oceans is comparable to that over land. Over the ocean, Kummerow's rain rate is the minimum throughout most of the tropics and in the northern extra-tropics. Prabhakara's is the highest in the latitudes between 10°N - 25°N. Over land, Arkin's rain rate is highest in most of the latitude bands, with large departure from the mean particularly in the latitudes between 30°-40°. Rain rates over land compiled by the GPCC were plotted on the same figure. Most of the algorithms, except Arkin's in latitudes north of 20°N, are very close to the GPCC estimate.

Figure 10 shows the zonal average rain rate for August 1987. The range of oceanic zonal mean is about 3 mm/day near the equator and about 1.5 mm/day in the subtropics around 20° latitudes. All oceanic algorithms show zonal maximum at latitude 5°N-10°N, except that of Prabhakara, which shows a maximum further north in the latitude 10°N-15°N. At the zonal mean rain rate minimum (20°S), the algorithms tend to cluster into two groups. The first group, consisting of Chang, Prabhakara, Wu, and Spencer has a zonal average of about 2 mm/day. The second group, consisting of Adler, Huffman, Kummerow, Arkin, and Susskind has a zonal average of less than 1 mm/day.

The variability over land (middle panel) is higher than that over the oceans. At the rain rate peak between 10°-15°N, the algorithms range from about 6 to 11 mm/day. Arkin's rain rates is the highest at this latitude. All algorithms peak at 10°N-15°N, whereas the GPCC data show a maximum at a latitude south of 10°N-15°N.

When averaged over ocean and land, the global zonal averages for all algorithms track each other well (lower panel). At the global zonal peak (5°-10°N), the algorithms range from about 7 to 10 mm/day. Arkin's rain rate is much higher than the rest at 35°-40°S.

Figure 11 shows the same statistics as those depicted in Figure 10 for May 1988. The peak in the oceanic zonal mean (4-7 mm/hr) is much smaller than that in August 1987 (7-10 mm/hr). There is also more variability among algorithms, with a range (maximum-minimum) of 3-4 mm/day for most of the latitude bands (upper panel). Over land (middle panel), the latitude of maximum rain shifted southward, and peaks between 50°S - 50°N. The high rain rate of Arkin's algorithm at the 35°-40° latitudes is also quite discernible.

Figure 12 shows the time series (August 1987- December 1988) of the global average rain rate over ocean (upper panel), over land (middle panel), and over both land and ocean (lower panel). Zonal averages derived from the GPCC are also included. The algorithm

variability over the oceans is of the order of 1.5 mm/day. Over land, the variability is higher, with Arkins rain rates distinctly higher than the average, especially during January - April 1988. If Arkin's data is excluded from the comparison, the range of globally averaged rainfall over land is comparable to that over the ocean. The global ocean average is about 3 mm/day, whereas that over land is about 2 - 2.5 mm/day. The combined average (land and ocean) are fairly stable for most algorithms, with a median of about 3 mm/day.

4.4 Regional Comparison

To investigate regional discrepancies, we partitioned the globe into three ocean sectors: Pacific, Atlantic, and Indian Ocean, and five land masses: North and South America, Eurasia, Australia, and Africa. Monthly zonal means for these ocean and land sectors were computed and their temporal variability examined.

Figures 13.1-13.17 shows the monthly zonal means for the Atlantic, Pacific, and Indian Ocean sectors for the period August 1987 through December 1988. In August 1987, the mean position of the ITCZ is located at 5°N-10°N. A secondary peak appears at 5°S-10°S. The secondary zonal peak strengthens in time. By December 1987, the intensity of the secondary peak is comparable to that of the ITCZ. The two zonal peaks then weakens. By March 1988, these peaks are no longer the prominent features in the zonal mean. In May 1988, the ITCZ re-establishes itself and continues to be the dominant zonal peak until November 1988. By December 1988, the peak in the southern hemisphere (10°S-15°S) re-emerges. All algorithms show this change.

The dominant feature in the Atlantic is the SACZ which shows a very pronounced seasonal displacement. The zonal maximum is situated at 5°N-10°N from August 1987 to November 1987. Its southward migration took place in January 1988, and a band of maximum rainfall is found in 5°S-5°N from February to April 1988. The return of the zonal maximum to its northern position started in May 1988. By June 1988, the zonal maximum is again seen at 5°N-10°N. Most of the algorithms follow this trend.

The main feature in the Indian Ocean is the Monsoon. The range of rain rates is highest in the equatorial and northern Indian Ocean (5°S-20°N). A band of maximum zonal rainfall is situated in the north Indian Ocean from August 1987 - October 1987. In November 1988, the maximum zonal rainfall is seem in the southern hemisphere. By December 1988, the zonal peak in the south equatorial Indian Ocean peak is clearly established. The zonal peak maintains its position till April 1988 when its northward excursion takes place. Arkin's rain rate is the largest, followed by Wu's for all the summer months at the zonal peak. The only exception is Huffman's rain rate in April 1988- it shows a peak at 10°S-15°S.

Figure 14.1-14.17 shows the zonal average for the land sectors. High variability are seen over South America (especially in the Amazon basin region), at the low latitudes of Eurasia,

and in the tropics in Africa. In South America the variability of algorithms seems to show seasonal dependency. For example, the rain rate range at 0°-5°N is 3 mm/day in August 1987, and reaches a range of 7 mm/day in February 1988. Arkin's rain rates is much higher then the rest of the algorithms at latitudes north of 25°N in Eurasia from October 1987 to May 1988. This period corresponds to the snow season in these latitudes, and IR rain estimates may be contaminated by the cold ground surface.

5 RESPONSE TO 1986-87 ENSO

Our study period saw the demise of the 1986-1987 (El Niño Southern Oscillation) (ENSO) episode and the return of the atmosphere to a relatively normal state. It therefore provides an opportunity to compare the responses of the algorithms to the same climate (ENSO) signal.

Figure 15 shows the rain rate distribution for August 1987 (upper panel), August 1988 (middle panel), and the normalized difference between August 1987 and August 1988 (difference divided by the mean, lower panel). The normalized difference is an index that ranges from -2 to +2. The extreme values occur when the rain rate in a pixel changes from zero in one month to a non-zero rain rate in the other month. Visual inspection shows the high spatial variability in the normalized index of Adler's algorithm which is contrasted with the low spatial variability of the algorithm's of Wu and Susskind.

Figure 16 shows the histograms of the normalized difference for all seven algorithms. Most of the histograms show bell-shape distributions. The histograms of Adler and Spencer's algorithm show secondary peaks at a normalized difference values of 2, whereas the GPCC histogram shows a secondary peak at a value of –2.

To quantify the difference, we define a paired-t statistics between these two months. Let $X(\mathbf{x})$ and $Y(\mathbf{x})$ denote the rain field in August 1987 and August 1988, respectively, where $\mathbf{x}$ is the position vector. The difference field $Z(\mathbf{x})$ is defined as

$$Z(\mathbf{x}) = \mathbf{X}(\mathbf{x}) - \mathbf{Y}(\mathbf{x}) \tag{3}$$

We want to test the null hypothesis $H_0 : E(Z) = 0$, where $E(Z)$ is the expected value of Z; i.e., there is no difference between the rain field in August 1987 and August 1988. Taking the expected value of the above equation, we get

$$E(Z) = E(X) - E(Y) \tag{4}$$

Let

$$t_0 = \frac{[Z]}{n^{-1/2} SD} \tag{5}$$

where [Z] and SD are the sample mean and standard deviation of Z (see Chang et al., 1995) Since t_0 has a t distribution with $n-1$ degree of freedom, H_0 is rejected if $abs(t) > t_{a,n-1}$. H_0 is accepted otherwise. For $a = 0.025$, $t_{a,n-1} = 1.96$ if $n > 30$.

Table 5 shows the paired–t statistics and PC between August 1987 and August 1988 for all the algorithms. Only the algorithms of Chang, Prabhakara, and Spencer show t-statistics greater than 1.96, hence H_0 can be rejected at the 95% confidence level, if all grid boxes can be assumed independent. Since rain fields are spatially correlated, the number of independent samples may effectively be less than n, even for the difference field. We will address this issue in a separate study. PCs between these two months were also computed. High paired t-statistics tend to be associated with low PC. Adler's algorithm is an exception. His algorithm shows the least paired-t statistics and the lowest PC.

6 SUMMARY AND DISCUSSIONS

Annual mean and monthly rain rates from nine algorithms were compared. Results from the annual (August 1987–July 1988) and two monthly (August, 1987 and May, 1988) comparison showed that there are substantial differences in the amount of rainfall estimated by different algorithms. The global mean rainfall estimated from the algorithms ranges from 2.7 to 3.5 mm/day. In comparison, the range of the GCM estimates (Figure 3 of Chahline, 1992) in the tropical region vary from 2 mm/day to 9 mm/day, and a more recent comparison shows a range from 2 to 3.7 mm/day (Lau *et al.*, 1996). These global estimates can be compared to past estimates. From water budget analysis, the global annual mean rainfall is estimated to be in the range of 2.6 to 3.2 mm/day (950 mm to 1130 mm) (Chahine, 1993; Eagleson, 1960).

The variability among algorithms tends to be high in regions of high rain rates, such as in the major rain bands (ITCZ, SPCZ, SACZ), monsoon regions, and in the Amazon. The ratio of the variability to the mean is in general less than 0.5, except in the oceanic dry regions. This high ratio is due to the difference in treatment of the low rain rates.

High PCs were found between algorithms that use the same satellite/sensor data as input. This points to sampling error as the dominant contributor to the errors in space/time

satellite rain algorithms. Future algorithms must address the sampling issue to improve the accuracy of satellite rain algorithms.The algorithms of Adler, Chang, Kummerow, and Prabhakara all used SSM/I data. Similarities between these algorithms are minimal since each algorithm is focused on different physics. Adler's algorithm is mainly based on the scattering signatures from ice particles. Chang's algorithm is based on the relationship between hydrometeors and microwave emission. The strength of Kummerow's algorithm is the capability to retrieve vertical profiles of precipitation and hydrometoers. Prabhakara's algorithm emphasizes the characterization of convective and stratiform rainfalls. These efforts are complementary. By combining their strength, an improved rainfall product can be provided to the community. For example, by combining Adlers scattering and Chang's emission algorithms, a global data set over land and oceans can be achieved. A beam–filling correction factor is required for Chang's algorithm which depends on the rain type and structure. Prabhakara's scheme for discriminating heavy convective and light stratiform rain can potentially contribute to Chang's algorithm. The convective and stratiform classification can also be valuable to Adler's scattering algorithm to account for the varying distribution of warm rain and stratiform rain, when the scattering signal is small. Kummerow's theoretical model should provides a better understanding of the instantaneous rainfall information in the footprint scale. This knowledge can be used by other investigators to further understanding the effect of non-raining cloud, thus improving the brightness temperature–rainfall rate (Tb–R) relationship.

Algorithms of Susskind and Wu are based on the parameters retrieved from TOVS sounding data. The major differences between these two algorithms are the variables used in their regression analyses. These products are derived primarily from TOVS observations and are complementary to those derived from SSM/I.

To address the sampling issue, techniques are being developed that combine microwave and IR data. These techniques take advantage of the superior time sampling of IR sensors onboard geostationary satellites and the physically based retrieval from microwave measurements. The unique feature of the combined algorithm is that the IR data can be calibrated against any microwave estimates, if such estimates are deemed superior.

Rainfall retrieval algorithms using SSM/I data are typically based on the differences in multi–spectral responses. General meteorological conditions associated with the satellite overpasses are usually treated as additional degrees of freedom in the retrieval. While satellite information has been used for data assimilation in GCMs, it might be advantageous to incorporate GCM parameters and rain gage measurements to the satellite rainfall retrievals, as described by Huffman *et al.* (1997).

Rainfall information from ground observations is needed for algorithm validation and comparison. At present, comparison data are available from only a few sources. GPCC and the Surface Reference Data Center (SRDC) of the GPCP are preparing global and regional (test–sites) rain gage data sets. Over the oceans, a 20 year monthly rainfall data set covering the western Pacific region have been compiled by Morrisey (1991). During the recent

TOGA-COARE Intensive Observing Period, shipboard radar and gage data have been collected. This radar rain rate data set has been used to validate satellite based rain algorithms for AIP–3. Over land, the network of weather radar can potentially provide continuous spatial coverage. Looking ahead, the TRMM project is acquiring data from various ground radar sites and field campaigns are planned as part of the validation program for TRMM algorithms. These rainfall data sets will prove to be of great value to the satellite rainfall community. However, a major effort is required to manage and distribute these data sets. It is hoped that the Earth Observing System Data and Information System (EOSDIS) will be able to fill this role.

Acknowledgments

We thank R. F. Adler, P. Arkin, G. Huffman, J. Janowiak, C. Kummerow, A. Negri, C. Prabhakara, R. Spencer, J. Susskind, and M. L. Wu for supplying us with their data and comments for this study, and K. M. Lau for his continued interest. J. Meng of SAIC/General Sciences Corporation provided programming and graphics support. This work is supported by NASA through an EOS Interdisciplinary Project Climate and Hydrospheric Processes.

References

Adler, R.F., A.J. Negri, P.R. Keehn and I.M. Hakkarinen, 1993: Estimation of monthly rainfall over Japan and surrounding waters from a combination of low-orbit microwave and geosynchronous IR data. *J. Appl. Meteor.*, **32**, 335-356.

Adler, R.F., H.–Y.M. Yeh, N. Passad, W.–K. Tao, and J. Simpson, 1991: Microwave simulations of a tropical rainfall system with a three–dimensional cloud model.*J. Appl. Meteor.*, **30**, 924-953.

Arkin, P.A., and B.N. Meisner, 1987: The relationship between large-scale convective rainfall and cold cloud over the western hemisphere during 1982–84. *Mon. Wea. Rev.*, **115**, 51-74.

Barrett, E., C., R. F. Adler, K. Arpe, P. Bauer, W. Berg, A. Chang, R. Ferraro, J. Ferriday, S. Goodman, Y. Hong, J. Janowiak, C. Kidd, D. Krivoton, M. Morrisey, W. Olsen, G. Petty, B. Rudolf, A. Shibata, E. Smith, and R. Spencer, 1994: The First WetNet Precipitation Project (PIP–1): Interpretation of the results, *Remote Sensing Reviews*, **11**, 303-373.

Chahine, M.T., 1992: The hydrological cycle and its influence on climate. *Nature*, **359**, 373-380.

Chang, A. T. C., L. S. Chiu, and G. Yang, 1995: Diurnal cycles of oceanic precipitation from SSM/I data, *Mon. Weath. Rev.*, **123**, 3371-3380.

Chiu, L., D. Short, G. North, and A. McConnell, 1990: Rain estimation from satellites: Effect of finite field of view.*J. Geophys. Res.*, **95**, 2177-2185.

Chiu, L. S., A. T. C. Chang, and J. Janowiak, 1993: Comparison of monthly rain rate derived from GPI and SSM/I using probability distribution functions. *J. Appl. Meteor.*, **32**, 323-334.

Ebert, E.: 1996: Results of the 3rd Algorithm Intercomparison Project of the Global Precipitation Climatology Project (GPCP). *BMRC Research Report* **No. 55**, Bureau of Meteorology Research Center, Victoria, Australia, 182 pp.

Huffman, G., R. Adler, P. Arkin, A. Chang, R. Ferraro, A. Gruber, J. Janowiak, A. McNab, B. Rudolf, and U. Schneider, 1997: The Global Precipitation Climatology Project (GPCP) combined precipitation dataset, *Bull. Amer. Soc.*, (in press).

Huffman, G., R. Adler, P. Keehn, A. Negri, 1993: Examples of global rain estimates from combined low orbit microwave and geosynchronous IR data. *AMS Fourth Symposium on Climate Change Studies*, 17-22, Jan. 1993, Anaheim, CA., 318-323.

Kummerow, C., R.A. Mack and I.M. Hakkarinen, 1989: A self-consistency approach to improve microwave rainfall estimates from space. *J. Appl. Meteor.*, **28**, 869-884.

Kummerow, C. and L. Giglio, 1994: A Passive microwave technique for estimating rainfall and vertical structure information from space, Part I: Algorithm description.*J. Appl. Meteor.*

Lee, T. H., J. C. Janowiak, and P. Arkin, 1991: Atlas of Products for the Algorithm Intercomparison Project 1: Japan and surrounding oceanic regions, Jun-Aug 1989. Univ. Corp. of Atmo. Research.

Lau, K-M, J. H. Kim, and Y. Sud, 1996: Intercomparison of hydrological process in AMIP GCMs. *Bull. Amer. Metero. Soc.*, **77**, 2209-2227.

Morrisey, M., 1991: Using sparse rain gages to test satellite-based rainfall algorithms. *J. Geophys. Res.*, **96**, D10, 18 561-18 571.

Prabhakara, C., G. Dalu, R. Suhasini, J.J. Nucciarone and G.L. Liberti, 1992: Rainfall over oceans: remote sensing from satellite microwave radiometers.*Meteor. & Atmos. Phys.*,**47**, 177-199.

Prabhakara, C., J.J. Nucciarone and G. Dalu, 1993: Convective and stratiform rain: multi-channel microwave sensing over oceans. *NASA TM-104586*, May 1993.

Rudolf, B., H. Hauschild, W. Ruth, and U. Schneider, 1994: Global precipitation climatology data base. in Climatic Parameters in Radiowave Propagation Prediction, CLIMPARA94, USRI Comm. F, Moscow, Russia.

Smith, E., Jungyun Chang, and James Lamm, 1995: PIP-2 Intercomparison Results report, [Preliminary], Department of Meteorology, Florida State University, Tallahassee, Florida 32312-3034.

Spencer, R.W., 1993: Global oceanic precipitation from the MSU during 1979-91 and comparisons to other climatologies. *J. Climate*, **6**, 1301-1326.

Susskind, J., D. Rosenfield, D. Reuter and M.T. Chahine, 1984: Remote sensing of weather and climate parameters from HIRS2/MSU on TIROS-N. *J. Geophys. Res.*, **89D**, 4677-4697.

Susskind, J. and J. Pfaendtner, 1989: Impact of interactive physical retrievals on NWP. *Joint ECMWF/EUMETSAT Workshop on the Use of Satellite Data in Operational Weather Prediction:* 1989-1993., V 1, 245-270.

Wilheit, T. T., 1988: Error analysis for the Tropical Rainfall Measuring Mission (TRMM) in Tropical Rainfall Measurements. A. Deepak Publishing, 377-385.

Wilheit, T.T., A.T.C. Chang and L.S. Chiu, 1991: Retrieval of monthly rainfall indices from microwave radiometric measurements using probability distribution functions. *J. Atmos. Oceanic Tech.*, **8**, 118-136.

Wu, M.-L., 1991: Global precipitation estimates from satellites: using difference fields of outgoing long-wave radiation. Atmoshpere-Ocean, 29 (1), 150-174.

Table 1: Characteristic of Satellite Rainfall Algorithms Included in this Study

Algorithm	Objective	Technique	Input	Spatial Resolution	Temporal Resolution	Domain
Adler	Instantaneous /Climatology	MW scattering	SSM/I 19, 22, 37 and 85 GHZ	0.5°×0.5°	monthly	global
Huffman	Climotology	MW calibrated IR threshold	MW and IR	2.5°×2.5°	monthly	+/- 40°
Arkin (GPI)	Climate scale rainfall	IR thresholding	Geostationary and AVHRR	2.5°×2.5°	Pantad	+/- 40°
Chang	Climatology	New emission, Lognormal pdf constraint	SSM/I 19 and 22 GHz	2.5°×2.5° and 5°× 5°	monthly	+/- 65° ocean
Kummerow	Instantaneous rainfall, Profile	Optimal, piecewise linear reg.	SSM/I 19, 22, 37 and 85 GHz	pixel	instant.	global
Prabhakara	Instantaneous /Climatology	Precipitation area	SSM/I 19, 37 and 85 GHz	3°×5°	instant. monthly	+/-50° ocean
Spencer	Climate scale	Regression on using MW threshold	MSU channel 3	2.5°×2.5°	monthly	+/- 50° global
Susskind	Instantaneous rainfall	Regression on using retrieved quantities	TOVS sounding products	60 km	twice daily	global
Wu	Mesoscale/ Climatology	Cloud radiative forcing	TOVS sounding products	4°× 5°	10 day, monthly	global

Table 2: Available Data from the Nine Algorithms for this Study

Algorithm	8	9	10	11	12	1	2	3	4	5	6	7	8	9	10	11	12
Adler	x	x	x	x		x	x	x	x	x	x	x	x	x	x	x	x
Huffman	x	x	x	x			x	x	x	x	x						
Chang	x	x	x	x		x	x	x	x	x	x	x	x	x	x	x	x
Prabhakara	x	x	x	x		x	x	x	x	x	x	x	x	x	x	x	x
Kummerow	x	x	x	x		x	x	x	x	x	x						
Spencer	x	x	x	x	x	x	x	x	x	x	x	x	x	x	x	x	x
Arkin	x	x	x	x	x	x	x	x	x	x	x	x	x	x	x	x	x
Suskind	x	x	x	x	x	x	x	x	x	x	x	x	x	x	x	x	x
Wu	x	x	x	x	x	x	x	x	x	x	x	x	x	x	x	x	x

Table 3: Pattern Correlation Coefficients for August 1987 Between Different Algorithms

	Huffman	Prabhakara	Chang	Kummerow	Spencer	Arkin	Susskind	Wu
Adler	0.9	0.66	0.88	0.92	0.74	0.82	0.83	0.79
Huffman		0.65	0.83	0.83	0.71	0.88	0.82	0.79
Prabhakara			0.70	0.68	0.76	0.60	0.68	0.70
Chang				0.90	0.75	0.78	0.79	0.78
Kummerow					0.76	0.79	0.79	0.77
Spencer						0.72	0.81	0.79
Arkin							0.91	0.87
Susskind								0.94

Table 4: Same as Table 2 except for May 1988

	Huffman	Prabhakara	Chang	Kummerow	Spencer	Arkin	Susskind	Wu
Adler	0.45	0.54	0.82	0.90	0.63	0.77	0.77	0.70
Huffman		0.23	0.38	0.42	0.33	0.47	0.44	0.42
Prabhakara			0.65	0.53	0.63	0.58	0.56	0.61
Chang				0.85	0.69	0.75	0.73	0.69
Kummerow					0.74	0.81	0.78	0.71
Spencer						0.76	0.79	0.75
Arkin							0.93	0.89
Susskind								0.93

Table 5: Paired-t Statistics and Pattern Correlation Coefficients Between August 1987 and 1988

Algorithm	Adler	Chang	Prabhakara	Spencer	Arkin	Susskind	Wu
Aug 87 mean	2.76	3.56	3.18	3.10	3.48	2.68	3.34
Aug 87 S.D.	3.40	3.59	3.09	2.69	4.38	2.46	2.68
Aug 88 mean	2.71	3.29	2.94	2.93	3.35	2.60	3.41
Aug 88 S.D.	3.25	3.41	2.84	2.82	4.26	2.49	2.90
paired-t	0.63	2.77	2.73	2.29	1.07	1.59	-1.13
Corr. coeff.	0.55	0.60	0.58	0.59	0.70	0.73	0.75

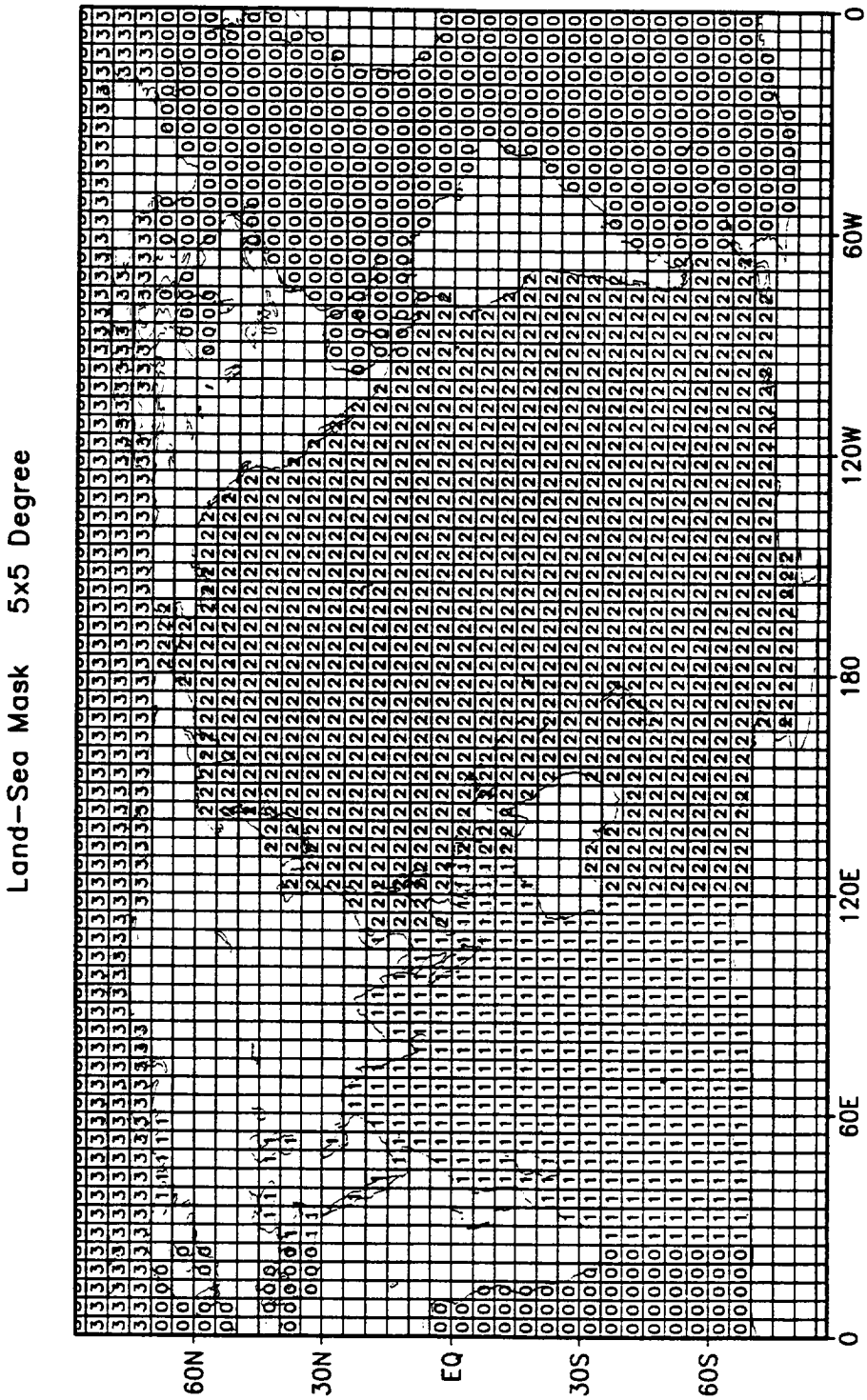

Figure 1: Land and sea mask used in this study. The oceans are further divided into the Atlantic, Pacific, and Indian ocean sectors, and the land into north and south America, Eurasia, Africa, and Australia sectors.

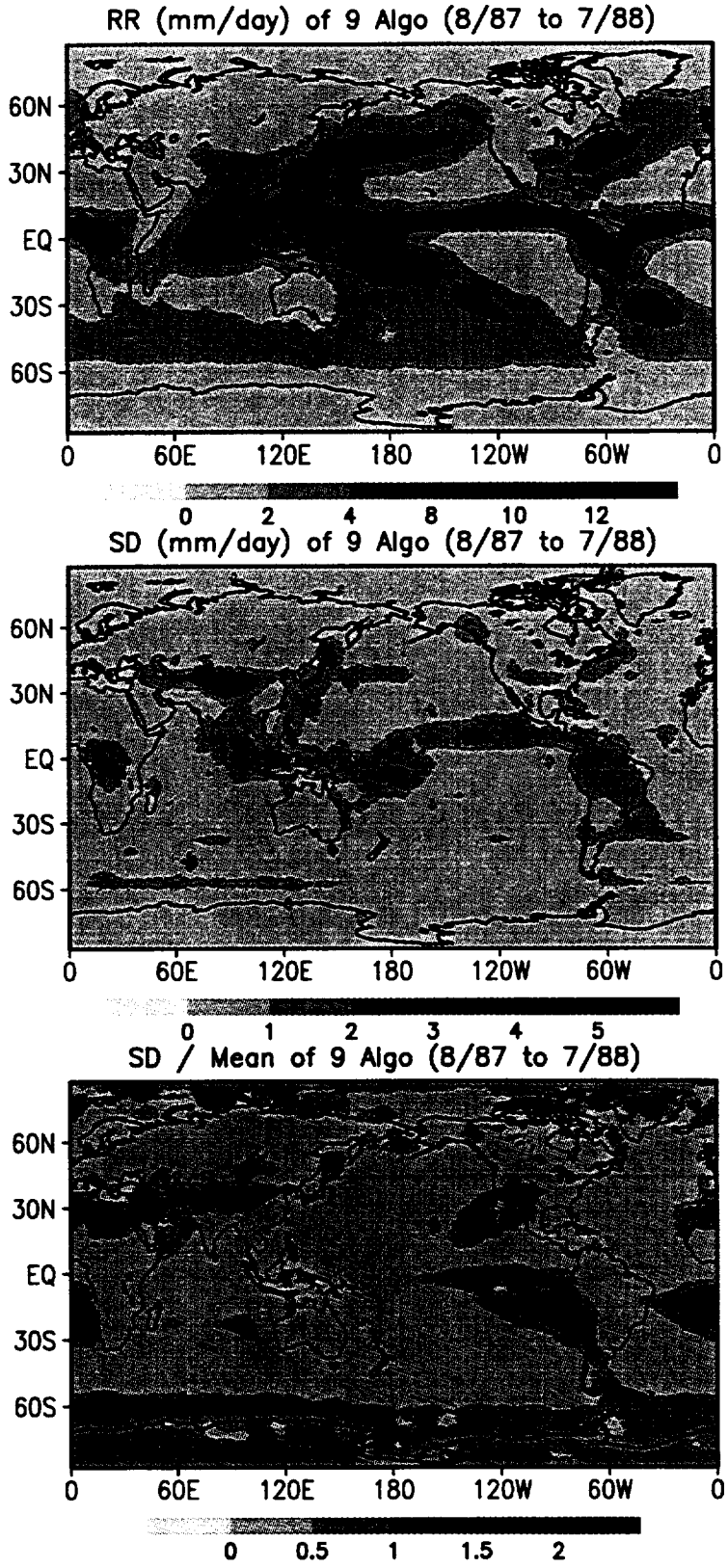

Figure 2: Mean (upper panel), standard deviation(SD, middle panel), and the ratio of the SD to the mean (lower panel) for the annual mean (August 1987 - July 1988). The ensemble average is taken over all nine algorithms.

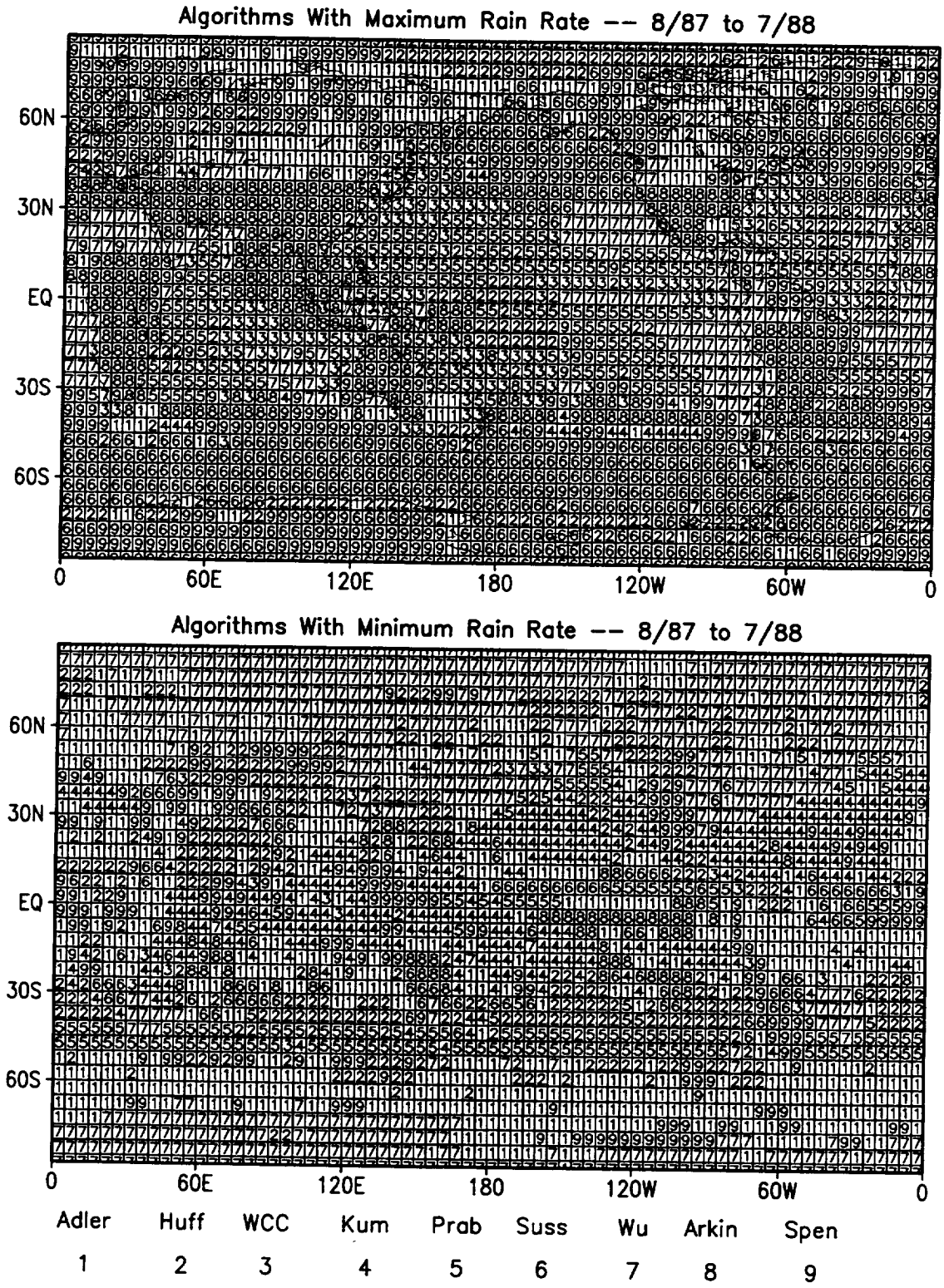

Figure 3: Algorithm with maximum (upper panel) and minimum (lower panel) rain rates for the annual mean.

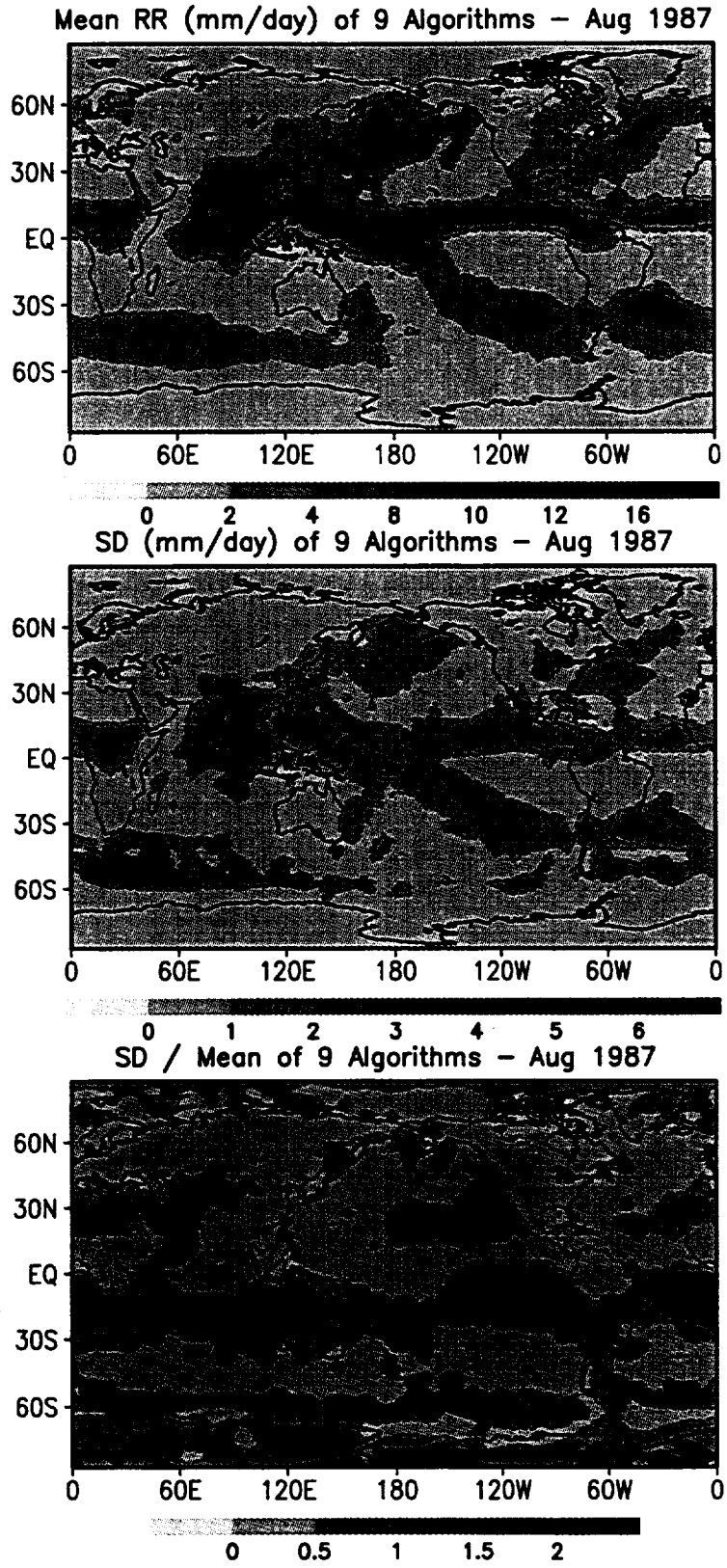

Figure 4.1: Same as Figure 2, except for August 1987.

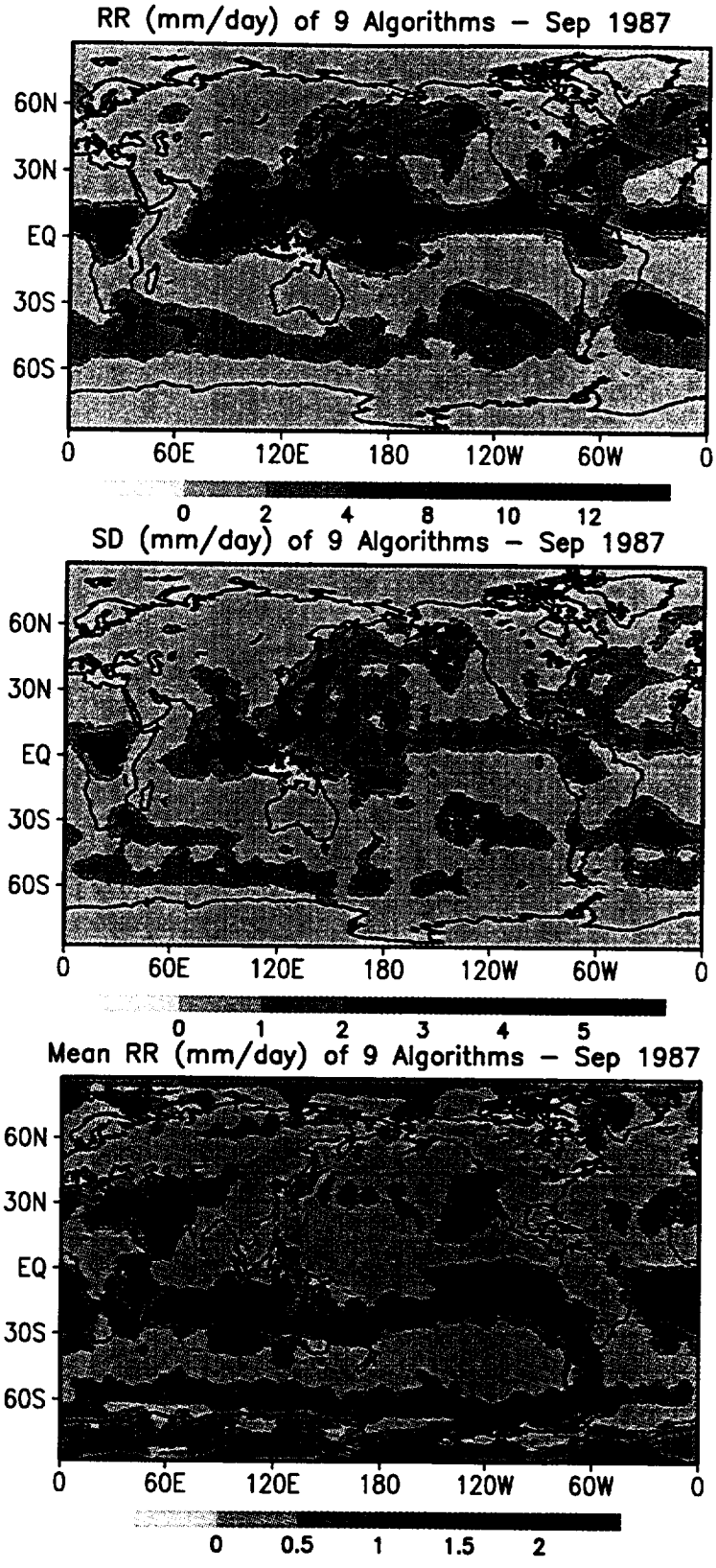

Figure 4.2: Same as Figure 2, except for September 1987.

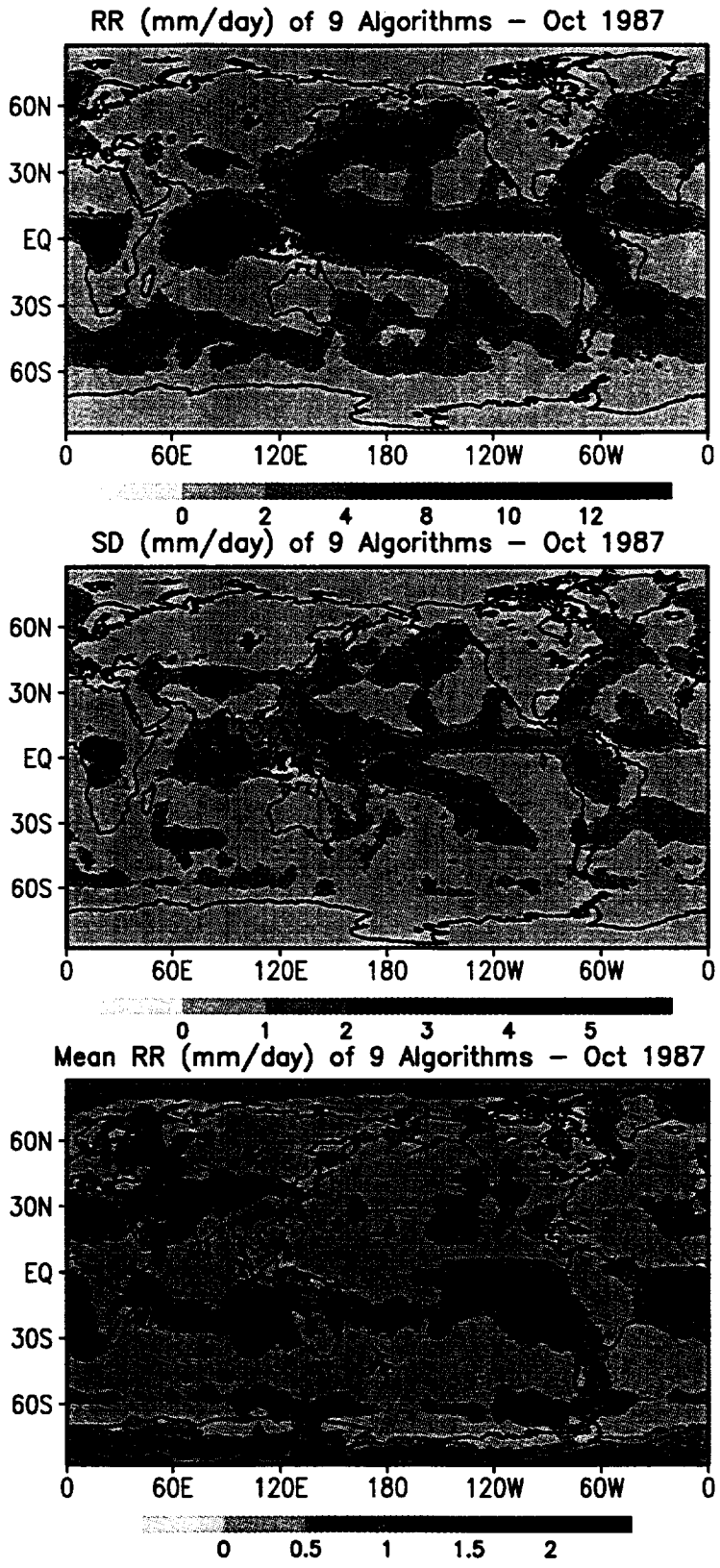

Figure 4.3: Same as Figure 2, except for October 1987.

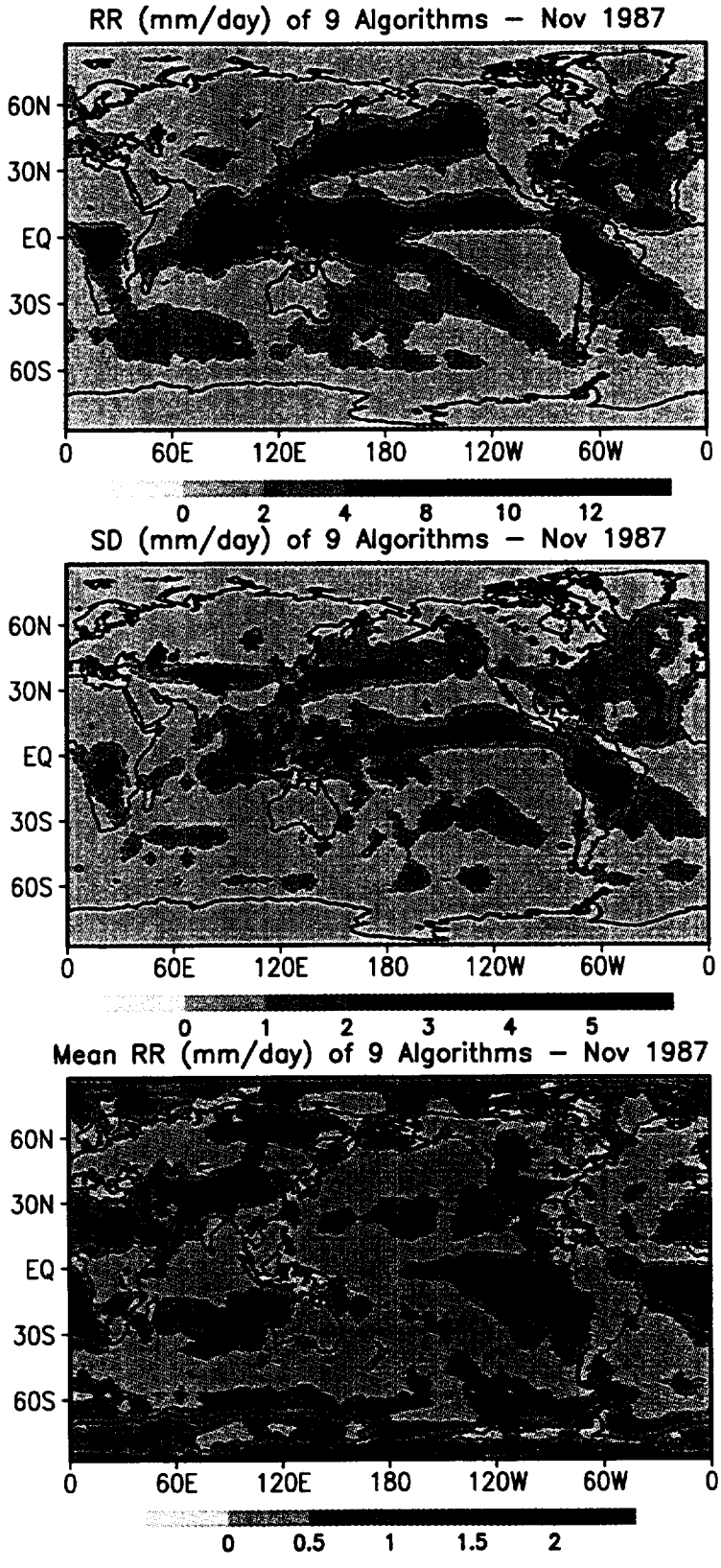

Figure 4.4: Same as Figure 2, except for November 1987.

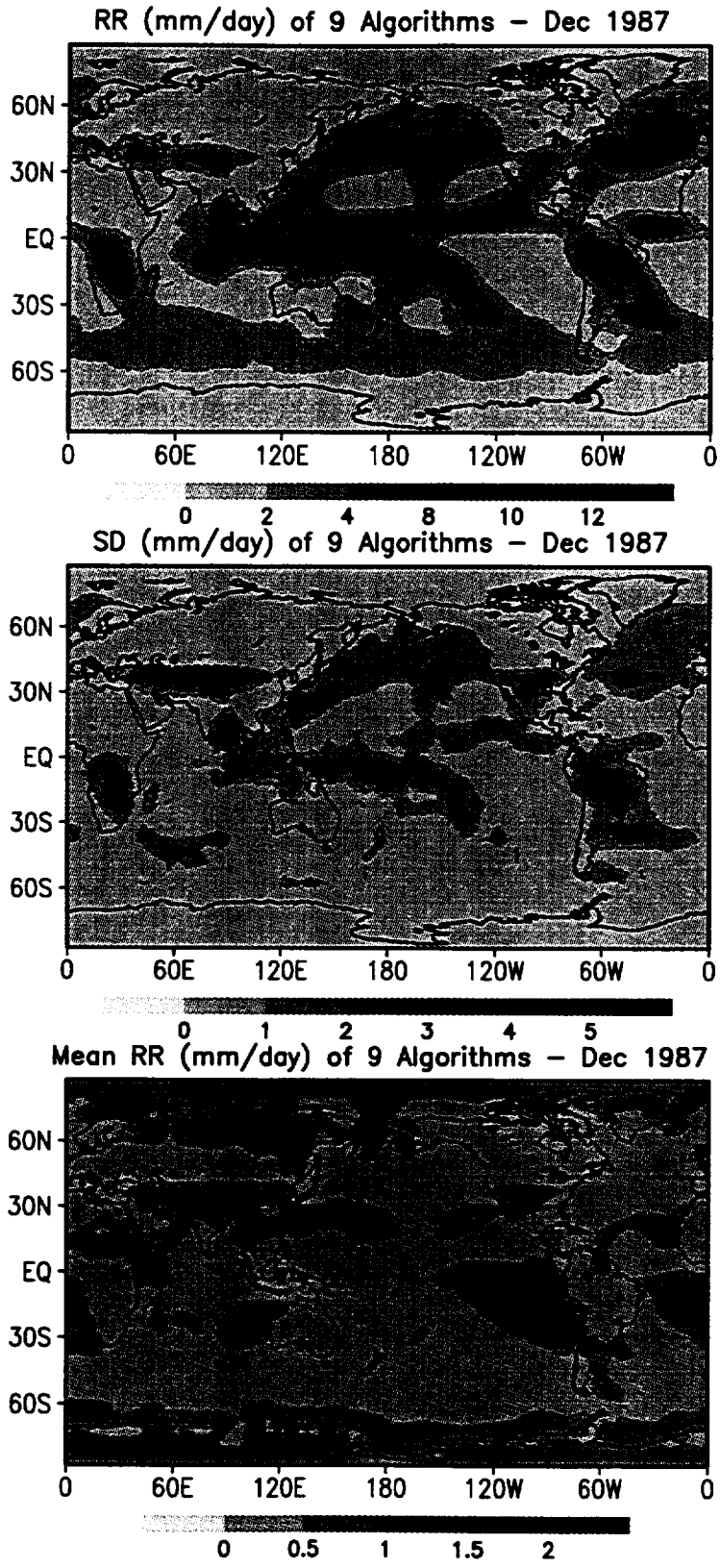

Figure 4.5: Same as Figure 2, except for December 1987.

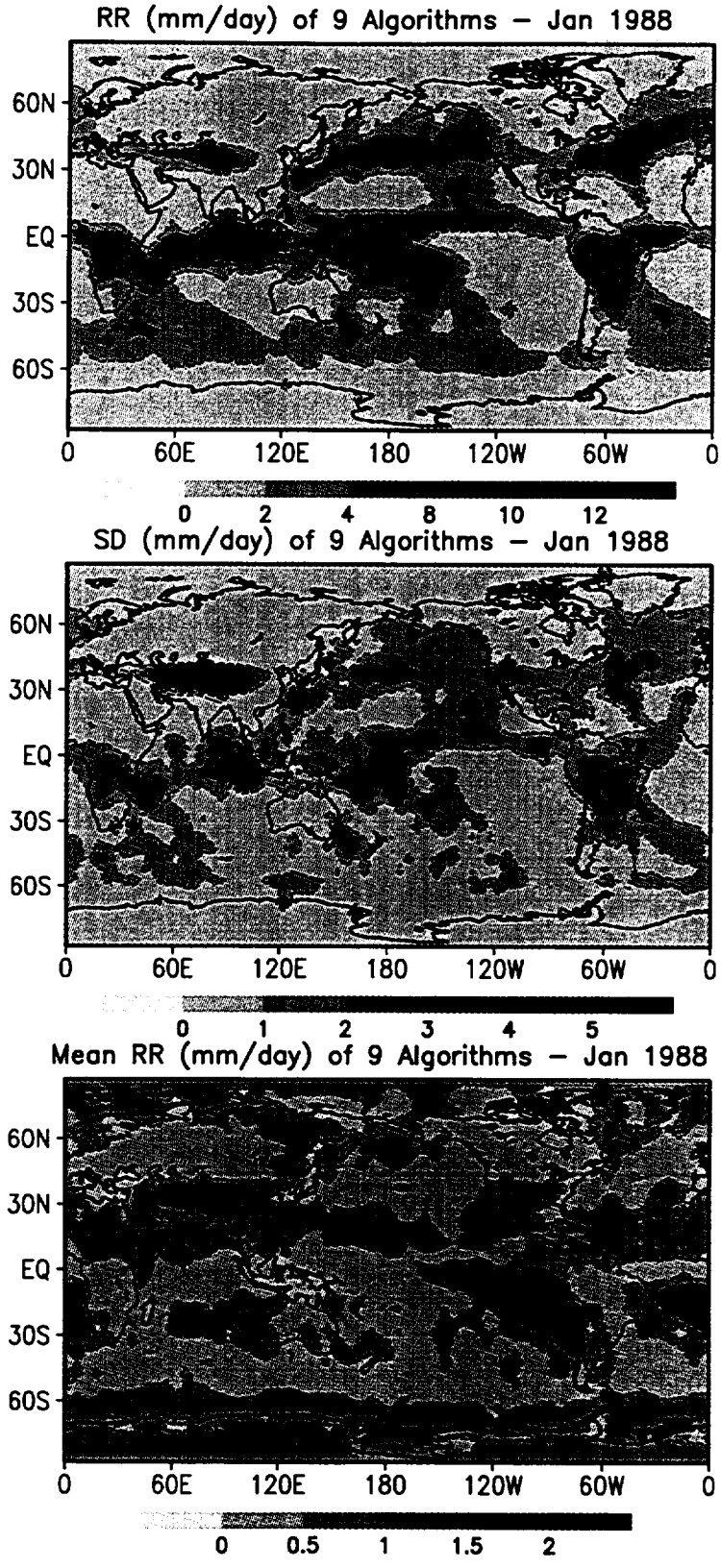

Figure 4.6: Same as Figure 2, except for January 1988.

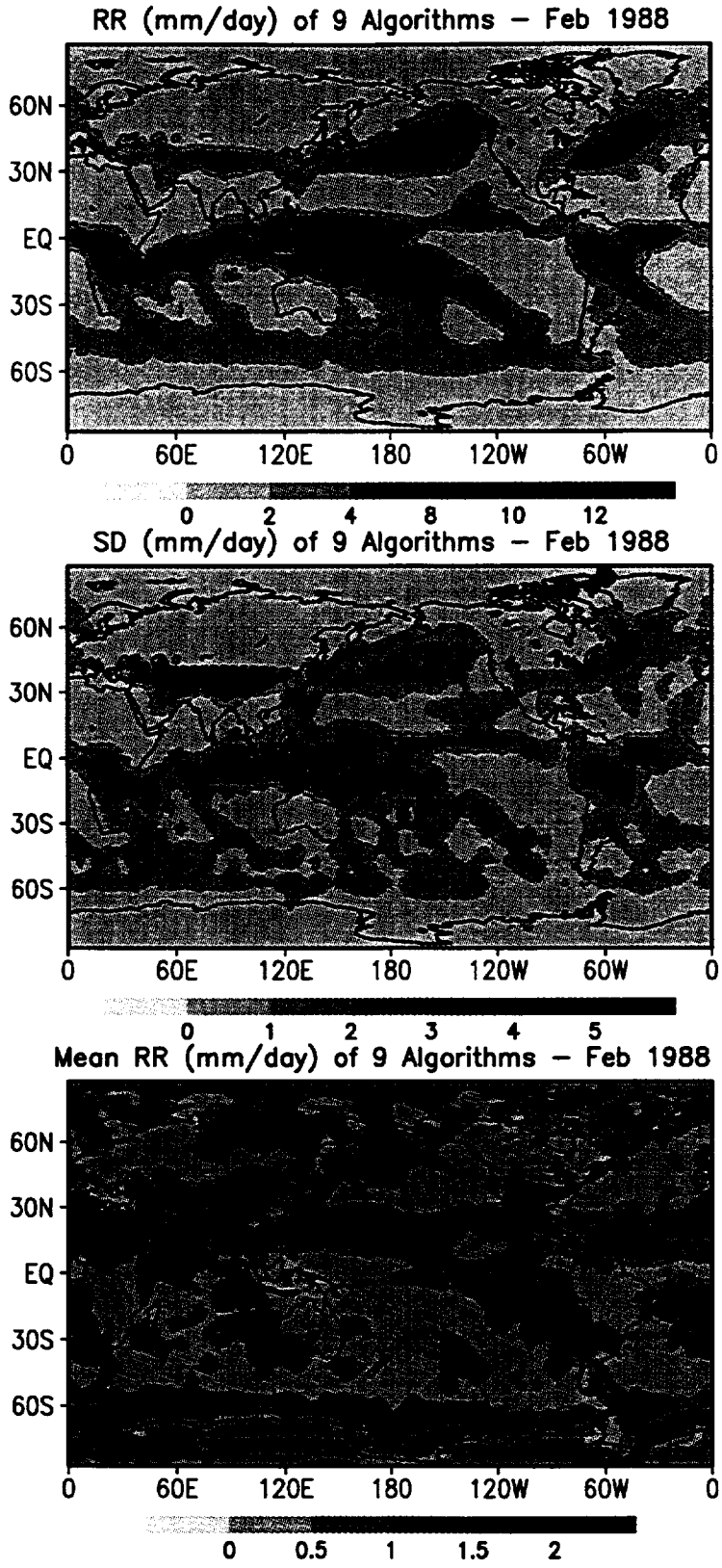

Figure 4.7: Same as Figure 2, except for February 1988.

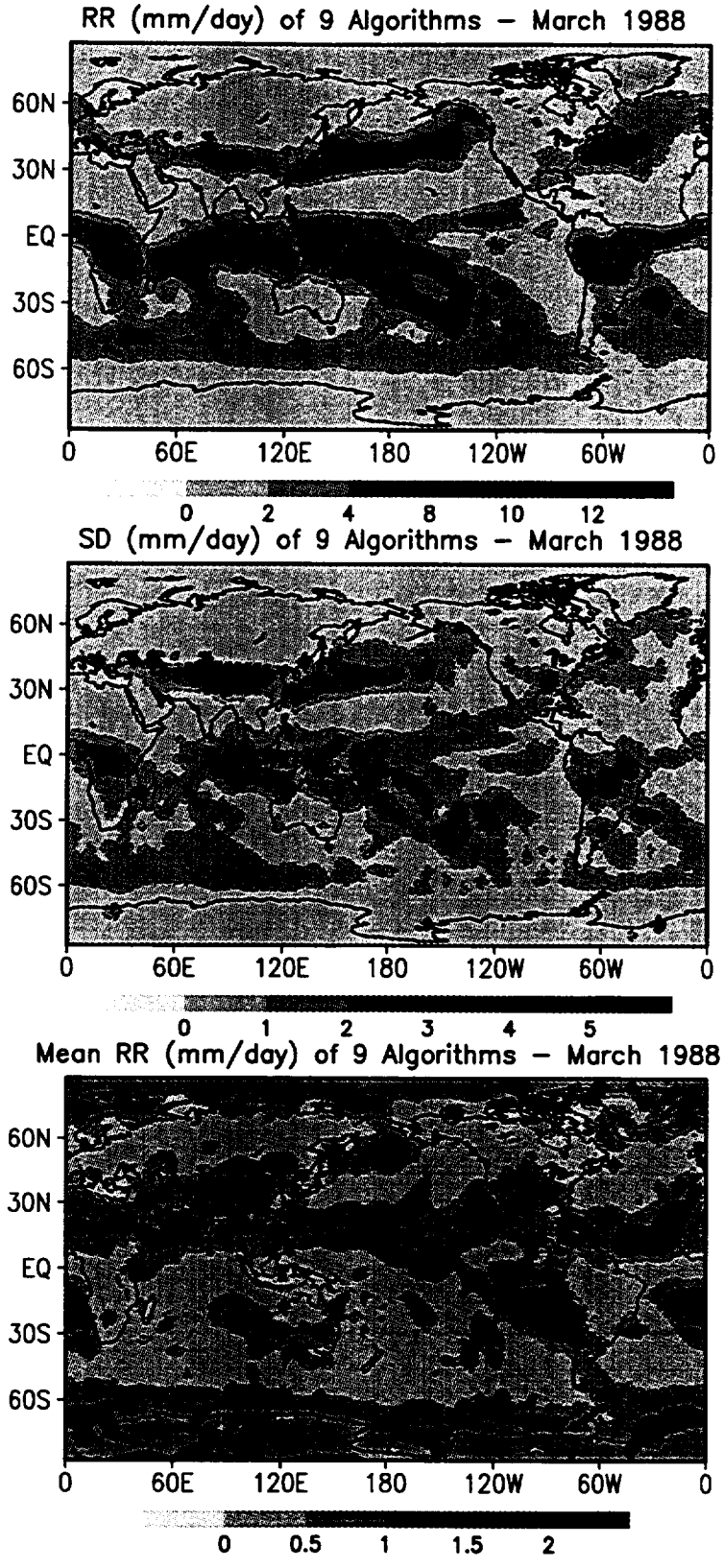

Figure 4.8: Same as Figure 2, except for March 1988.

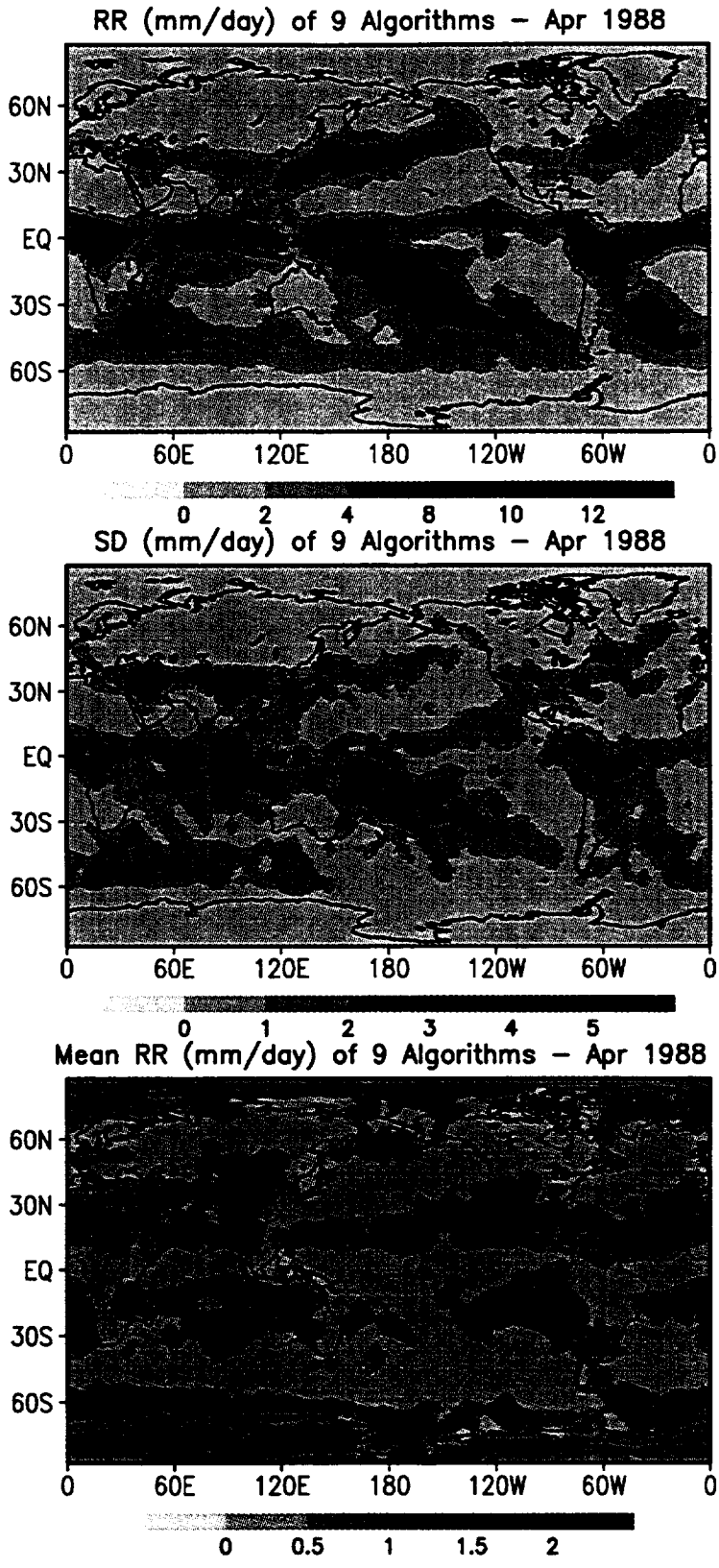

Figure 4.9: Same as Figure 2, except for April 1988.

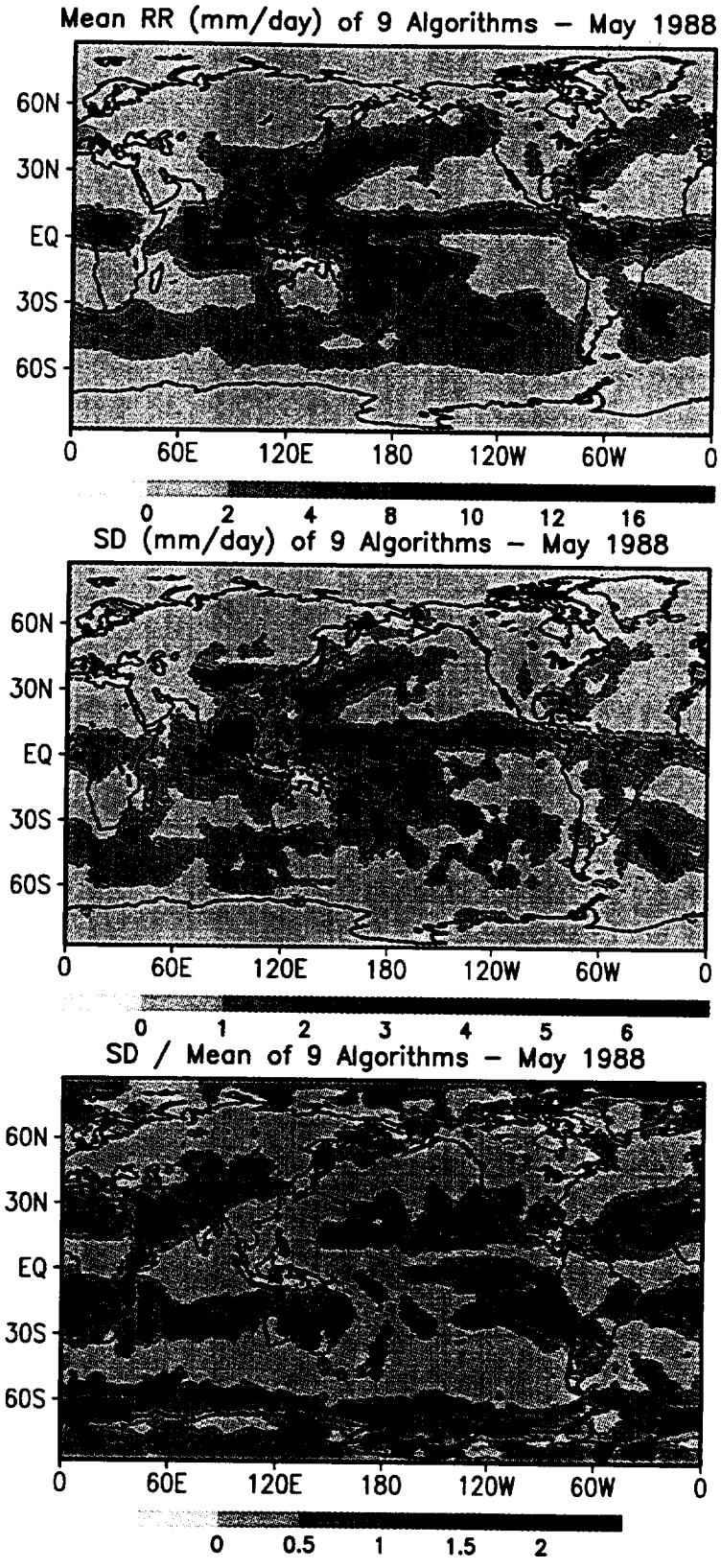

Figure 4.10: Same as Figure 2, except for May 1988.

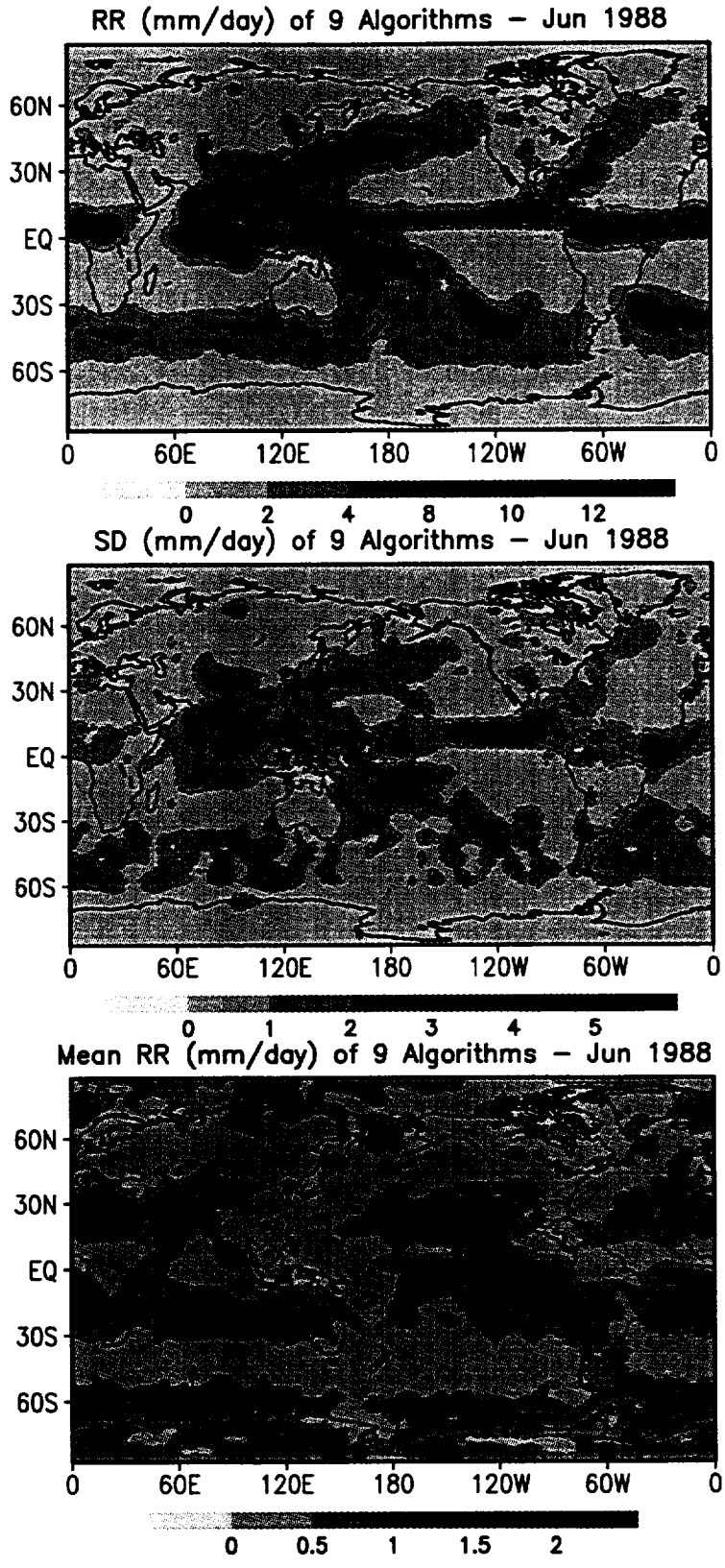

Figure 4.11: Same as Figure 2, except for June 1988.

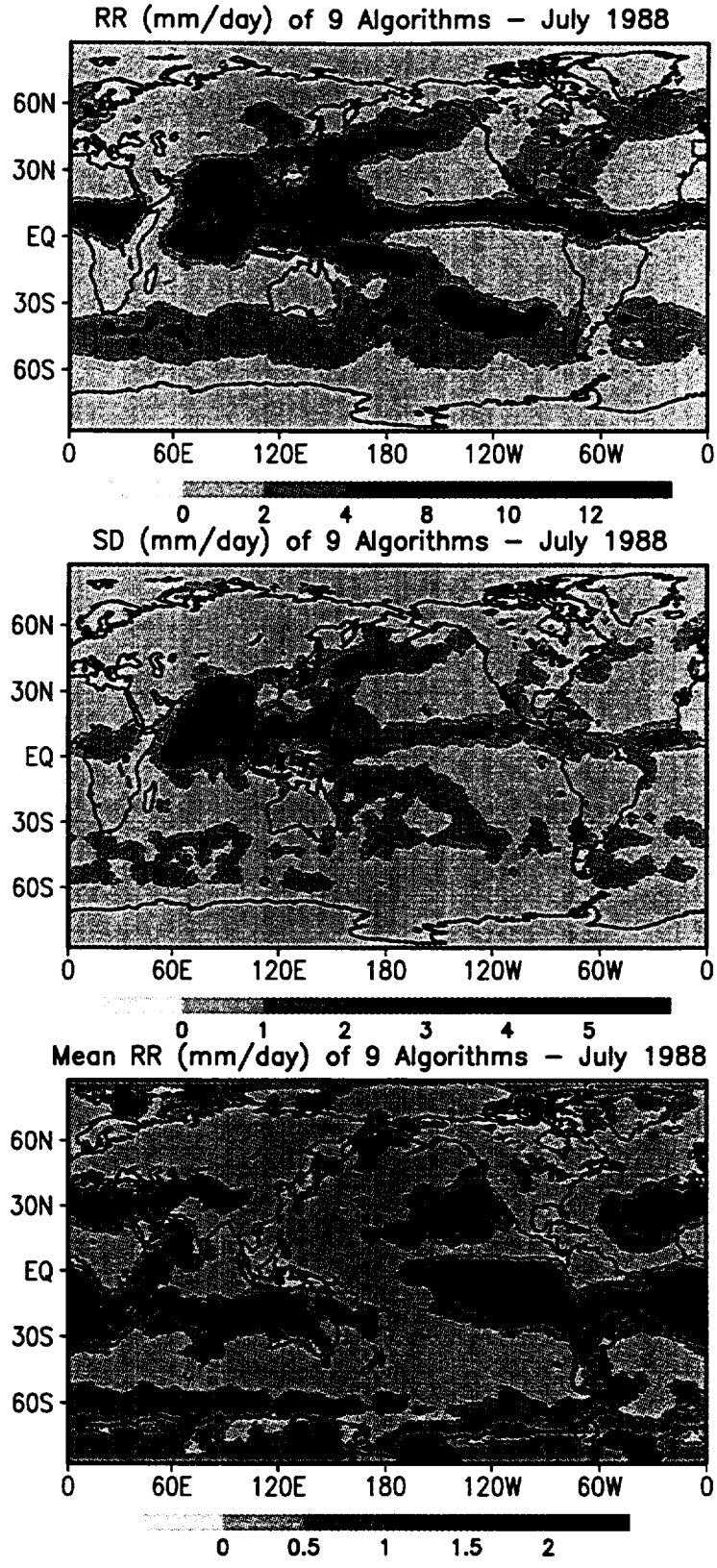

Figure 4.12: Same as Figure 2, except for July 1988.

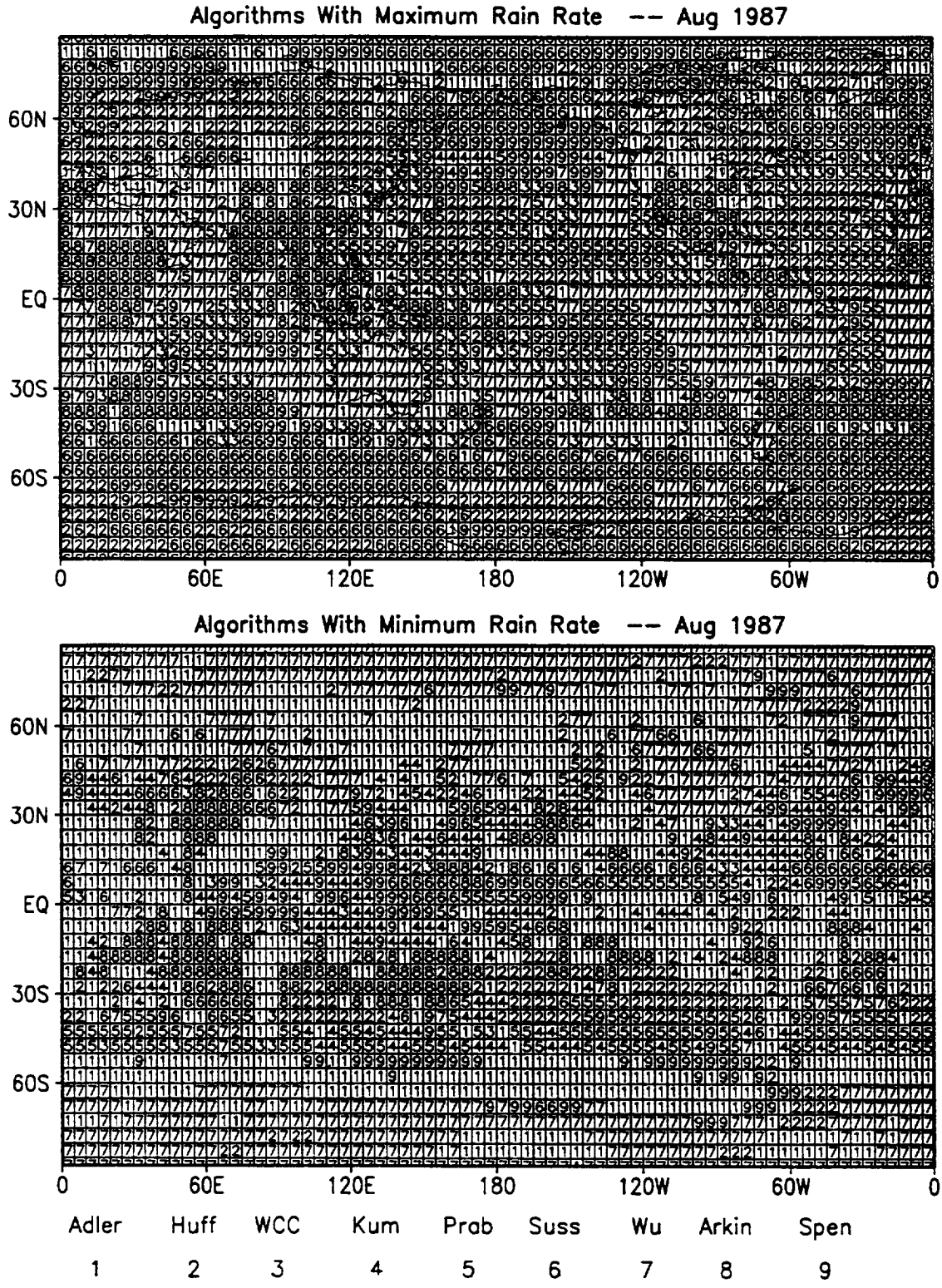

Figure 5.1: Same as Figure 3, except for August 1987.

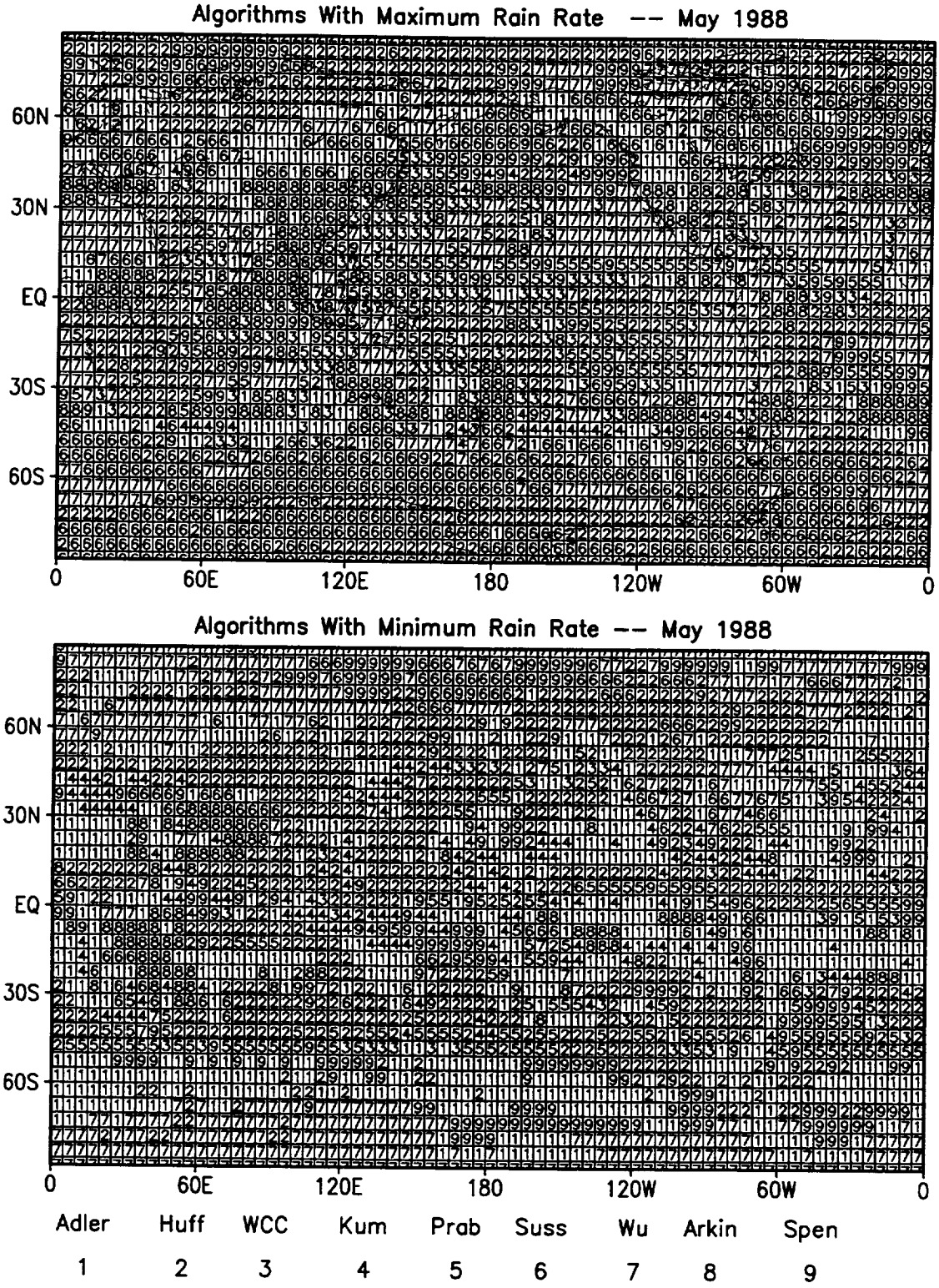

Figure 5.2: Same as Figure 3, except for May 1988.

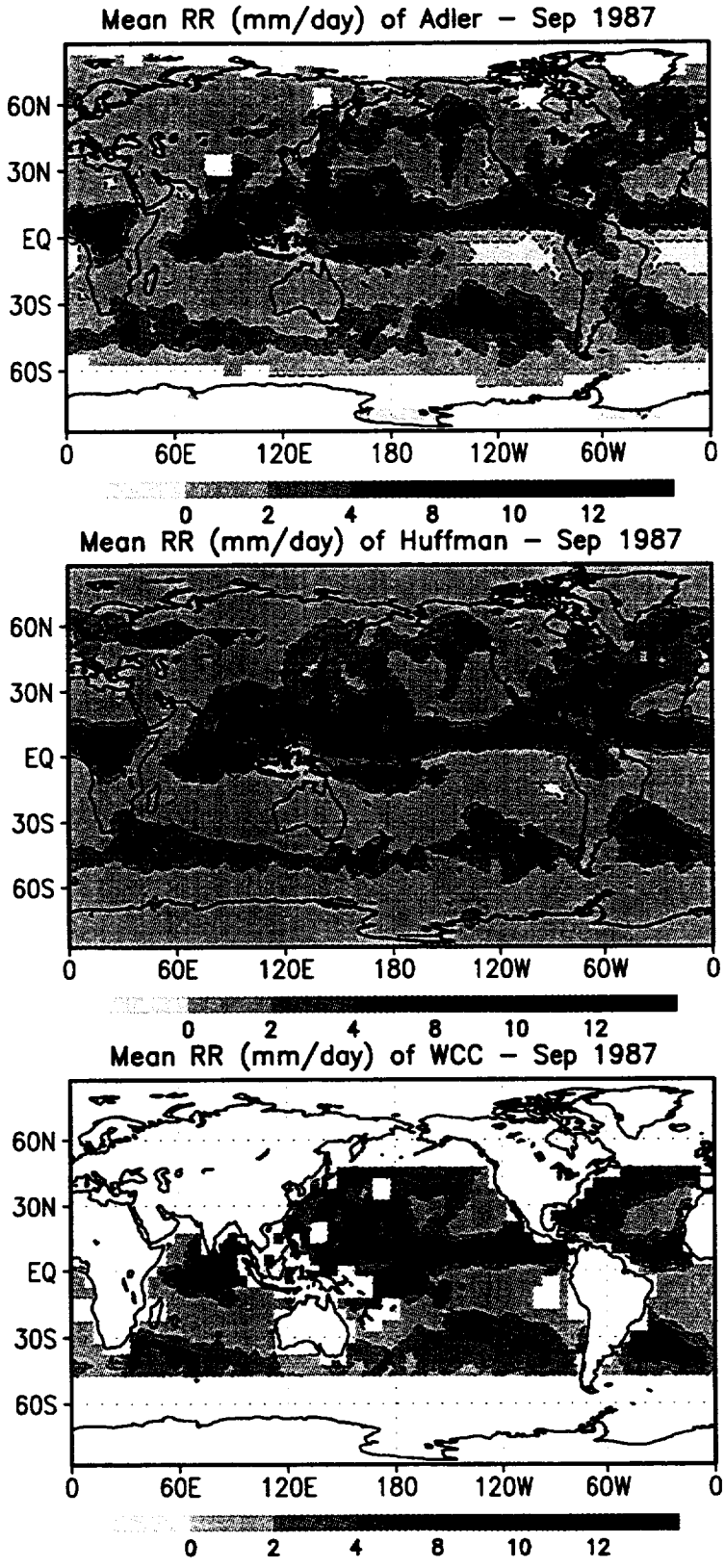

Figure 6: Monthly rainfall for September 1987 for all algorithms.

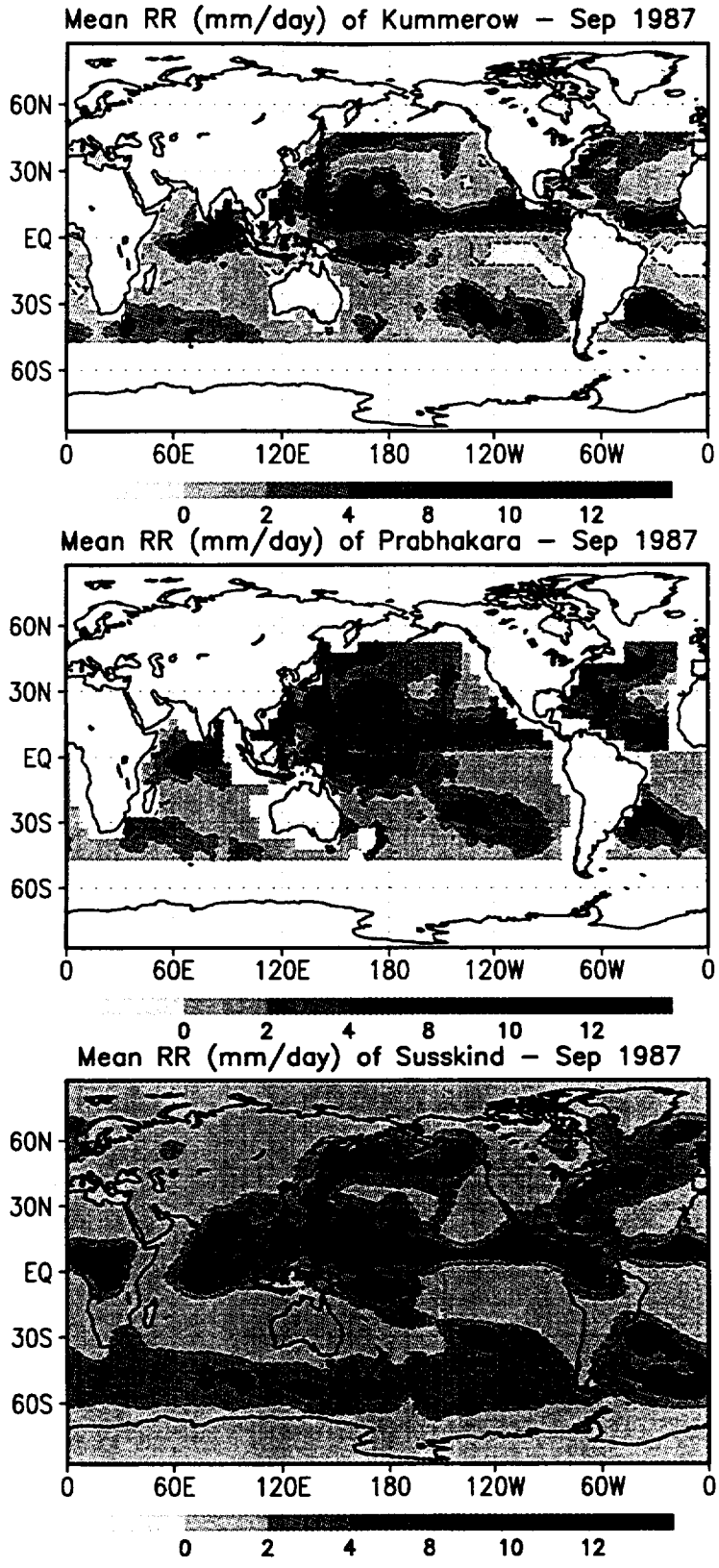

Figure 6-continued 1: Monthly rainfall for September 1988 for all algorithms.

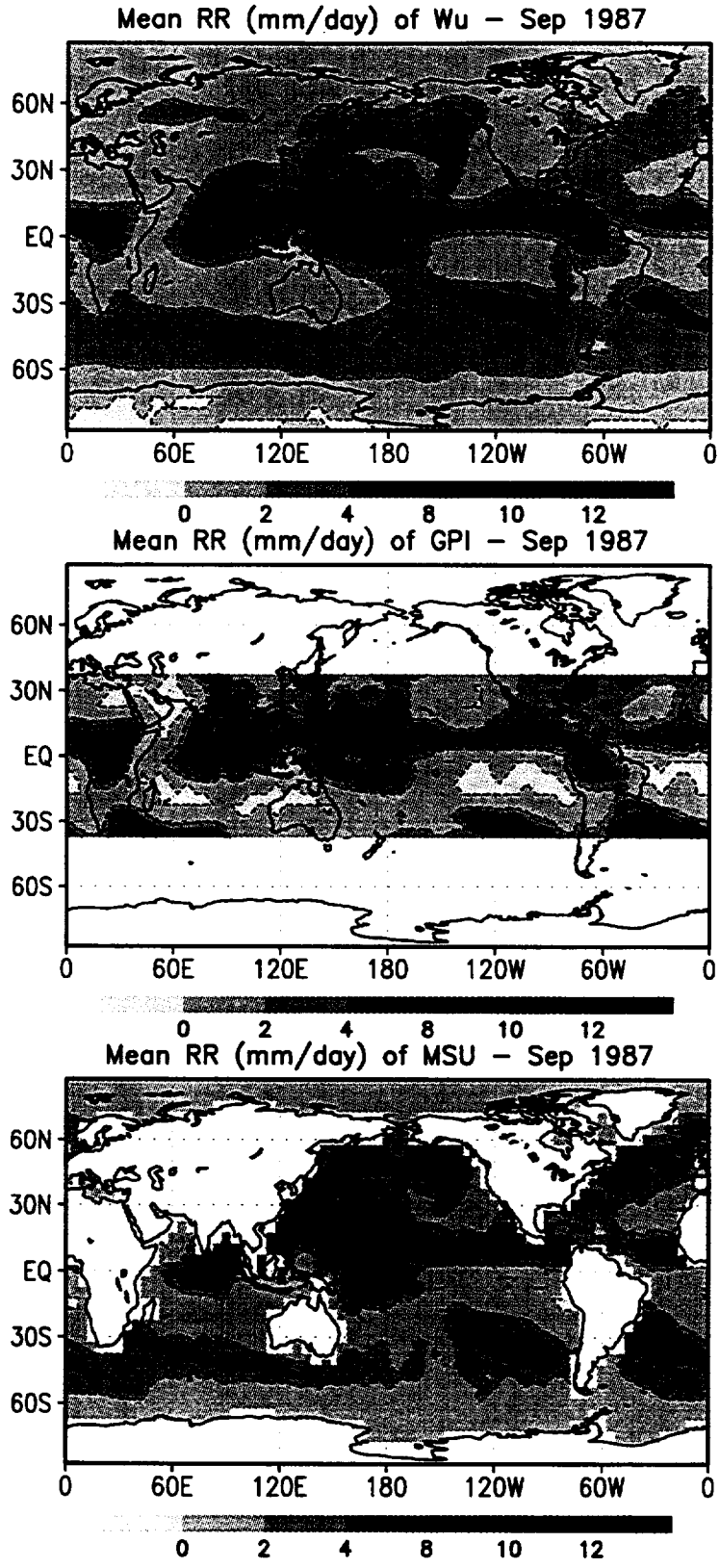

Figure 6-continued 2: Monthly rainfall for September 1987 for all algorithms.

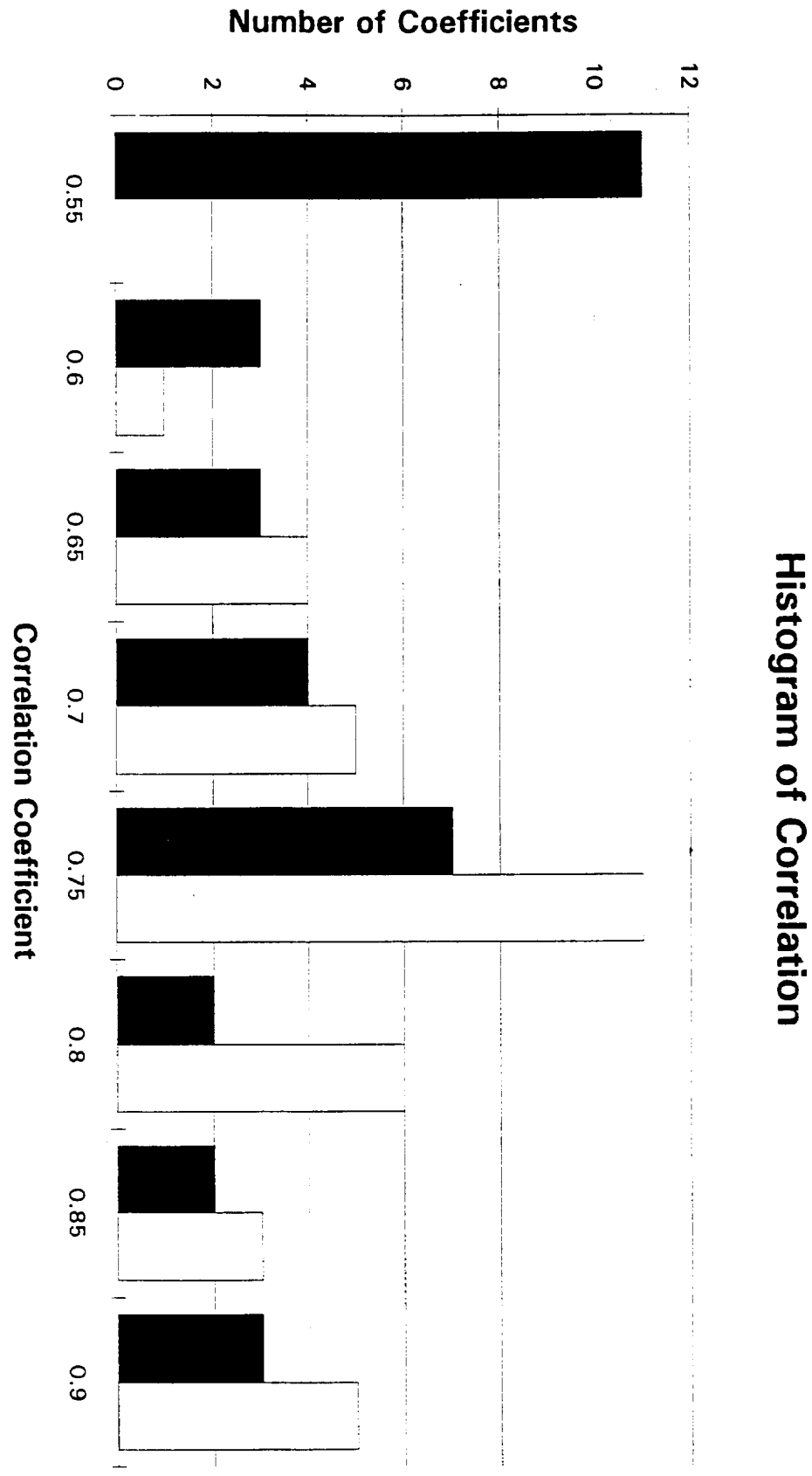

Figure 7: Histogram of pattern correlation coefficients among algorithms for August 1987 and May 1988. The bin 0.9 includes PC coefficients in the interval (0.90, 0.95).

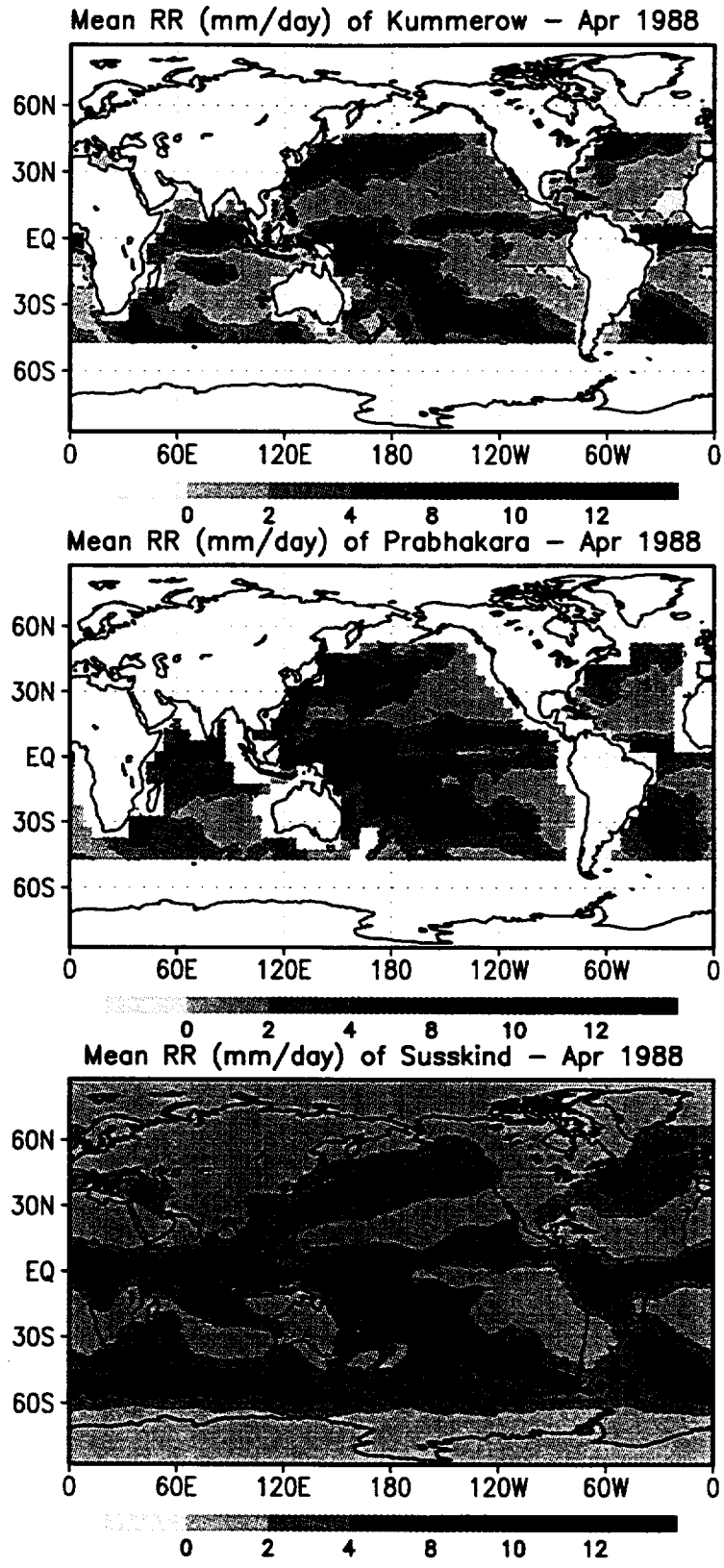

Figure 8: Monthly rainfall for April 1988 for all algorithms.

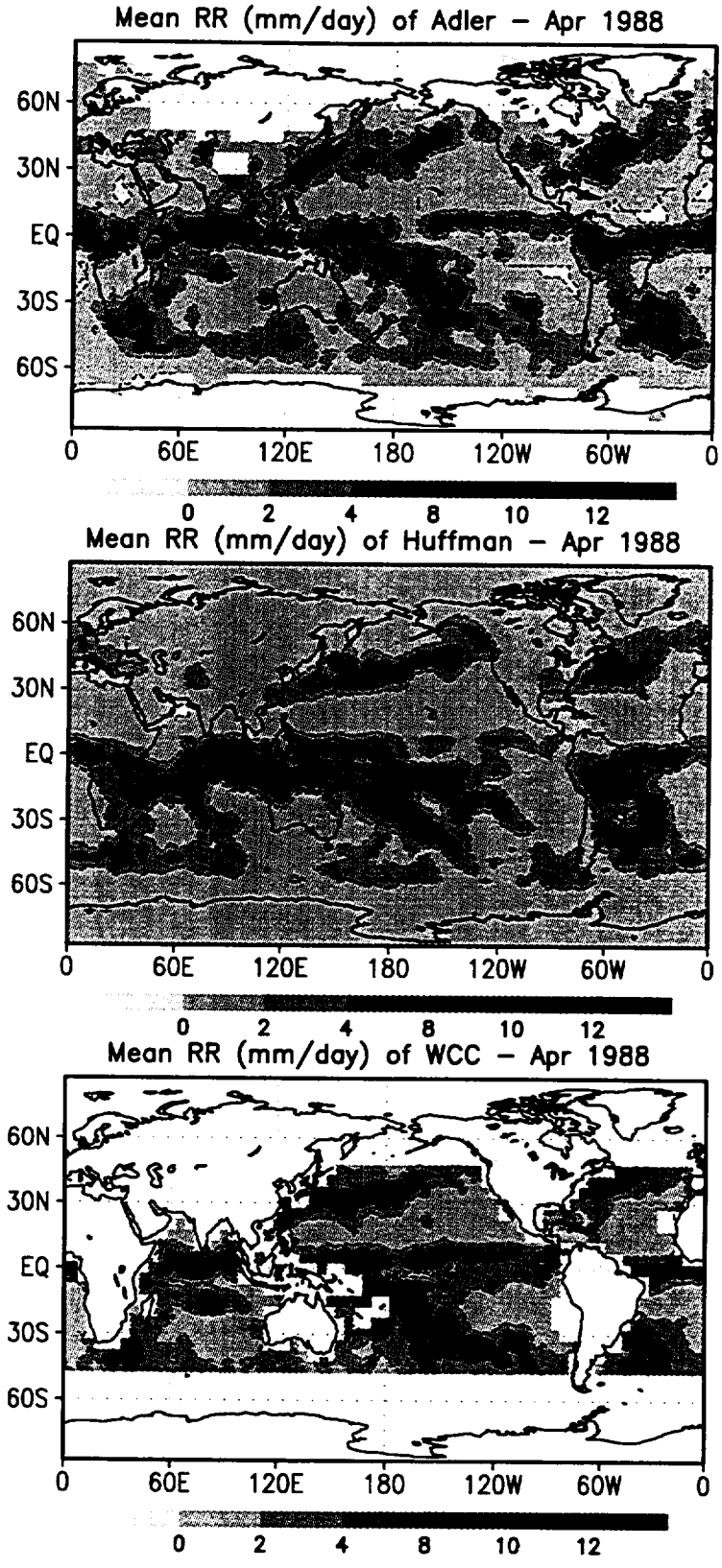

Figure 8 continued 1: Monthly rainfall for April 1988 for all algorithms.

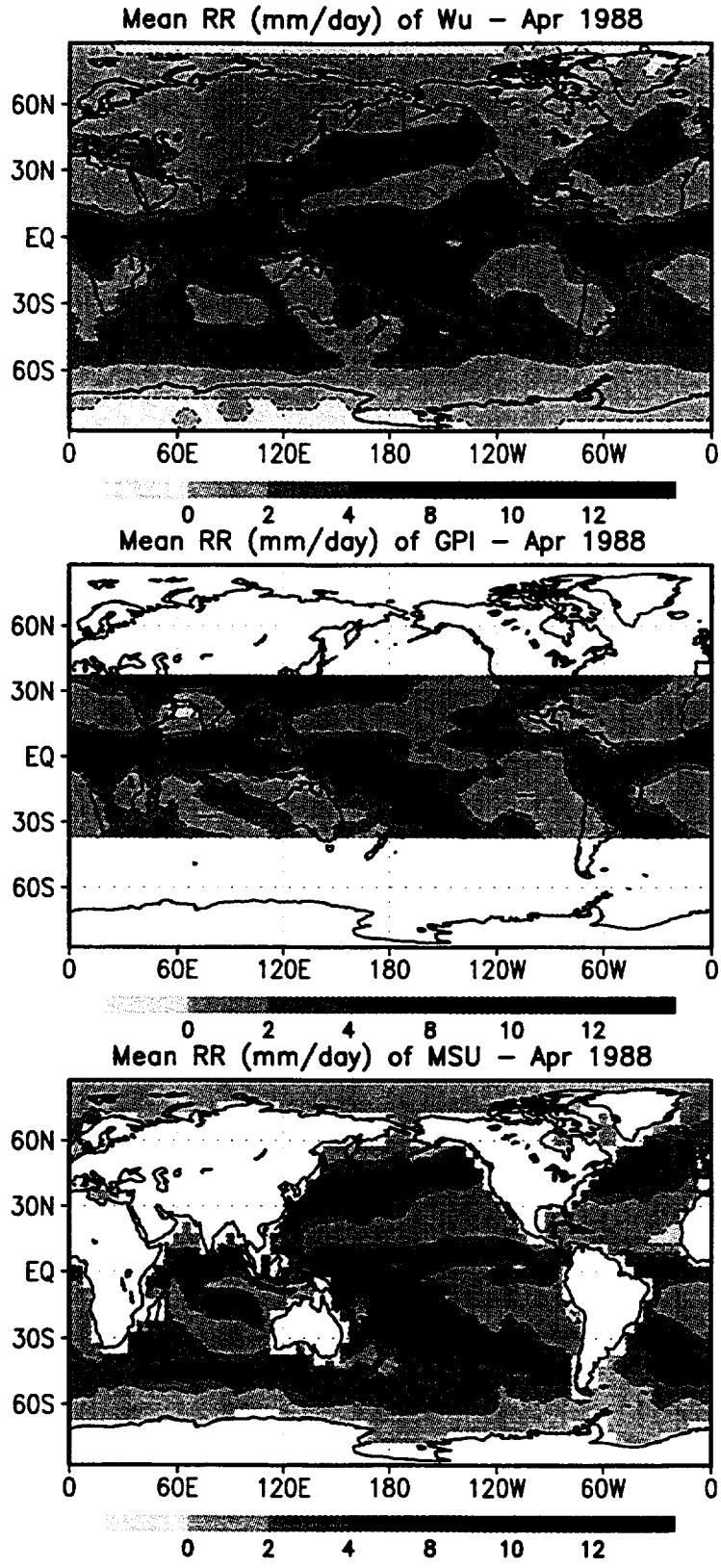

Figure 8 continued 2: Monthly rainfall for April 1988 for all algorithms.

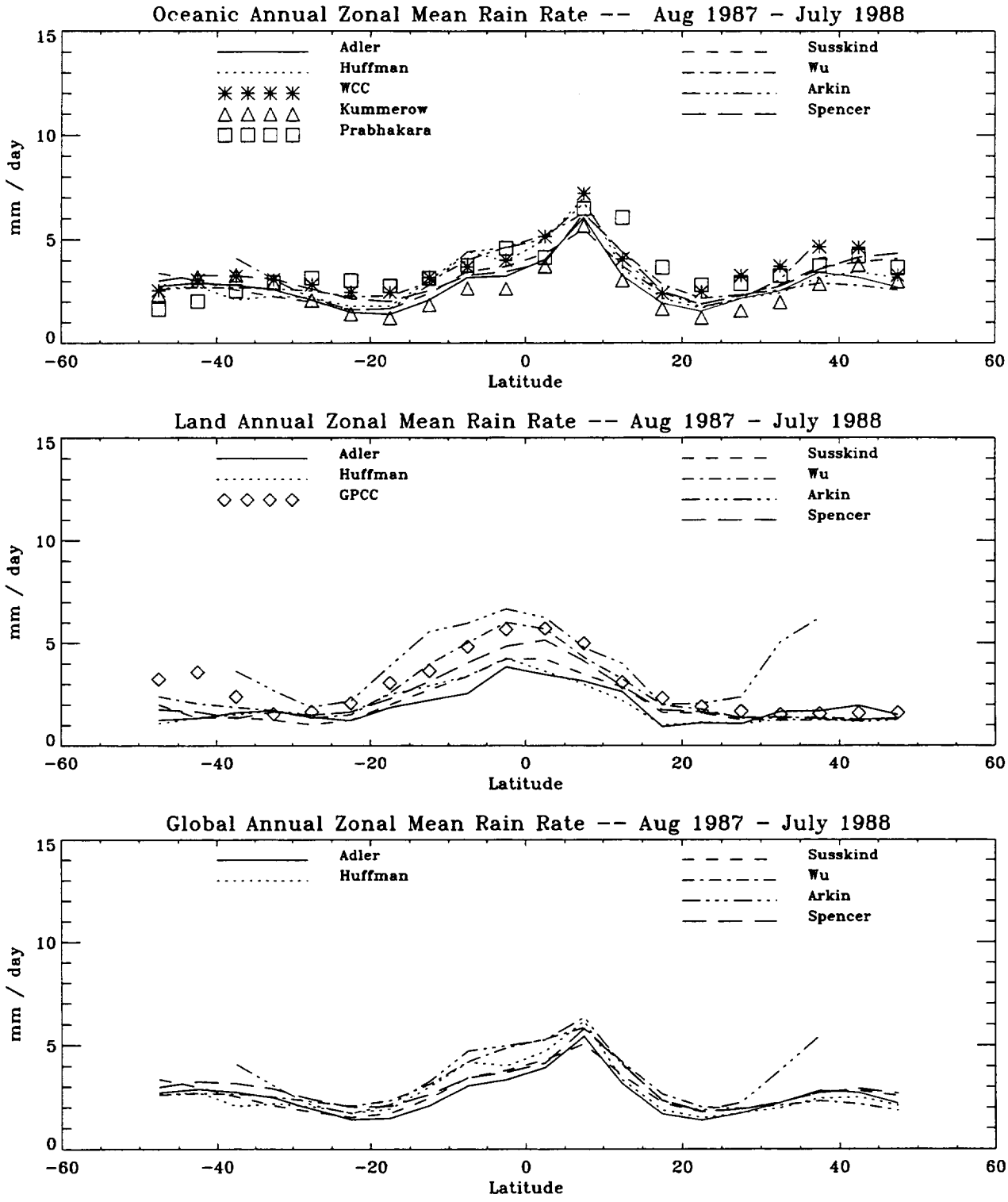

Figure 9: Zonal mean rain rates over the oceans (upper panel), land (middle panel) and over both land and ocean (lower panel) for the annual mean (August 1987-July 1988).

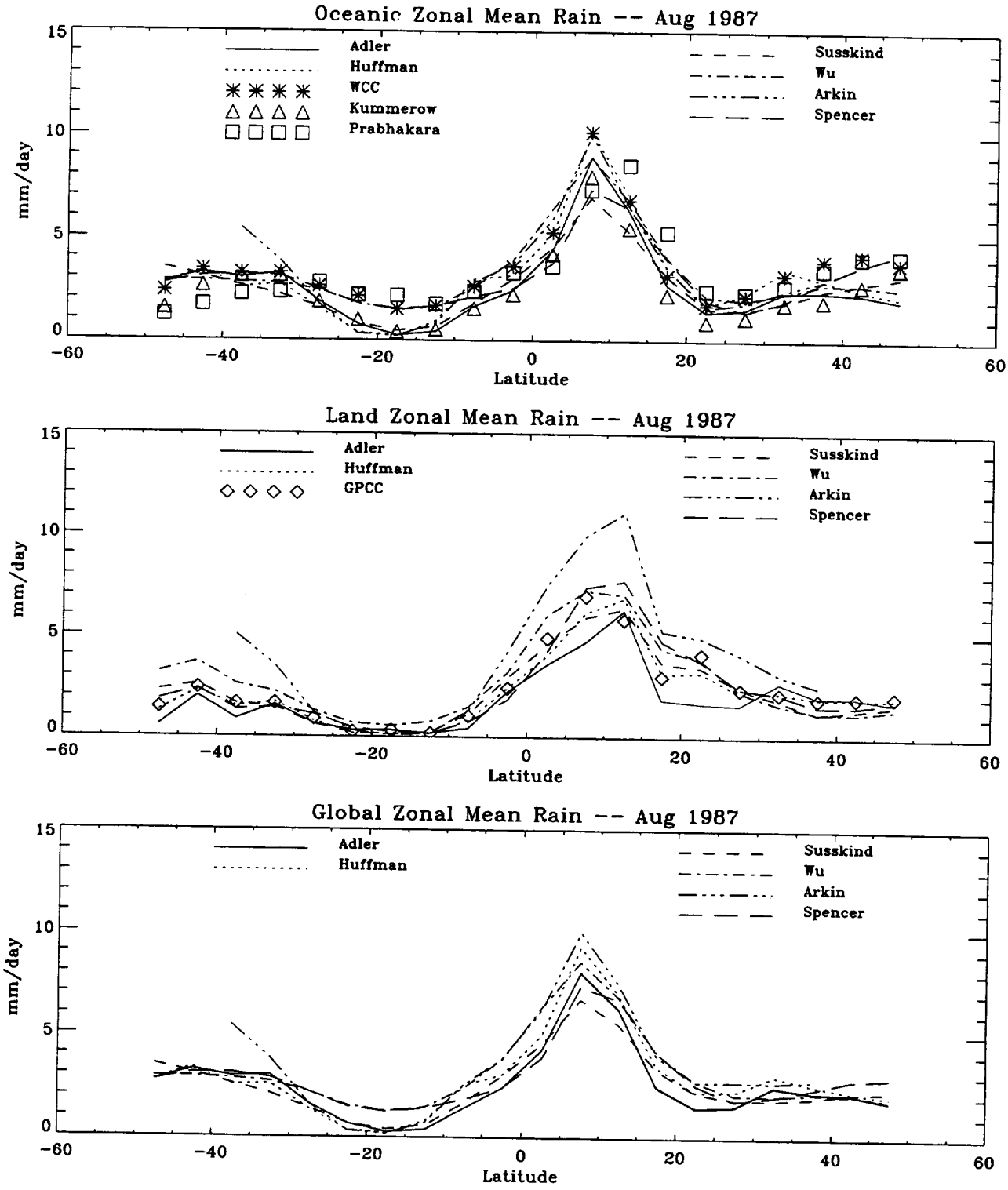

Figure 10: Same as Figure 9, except for August 1987.

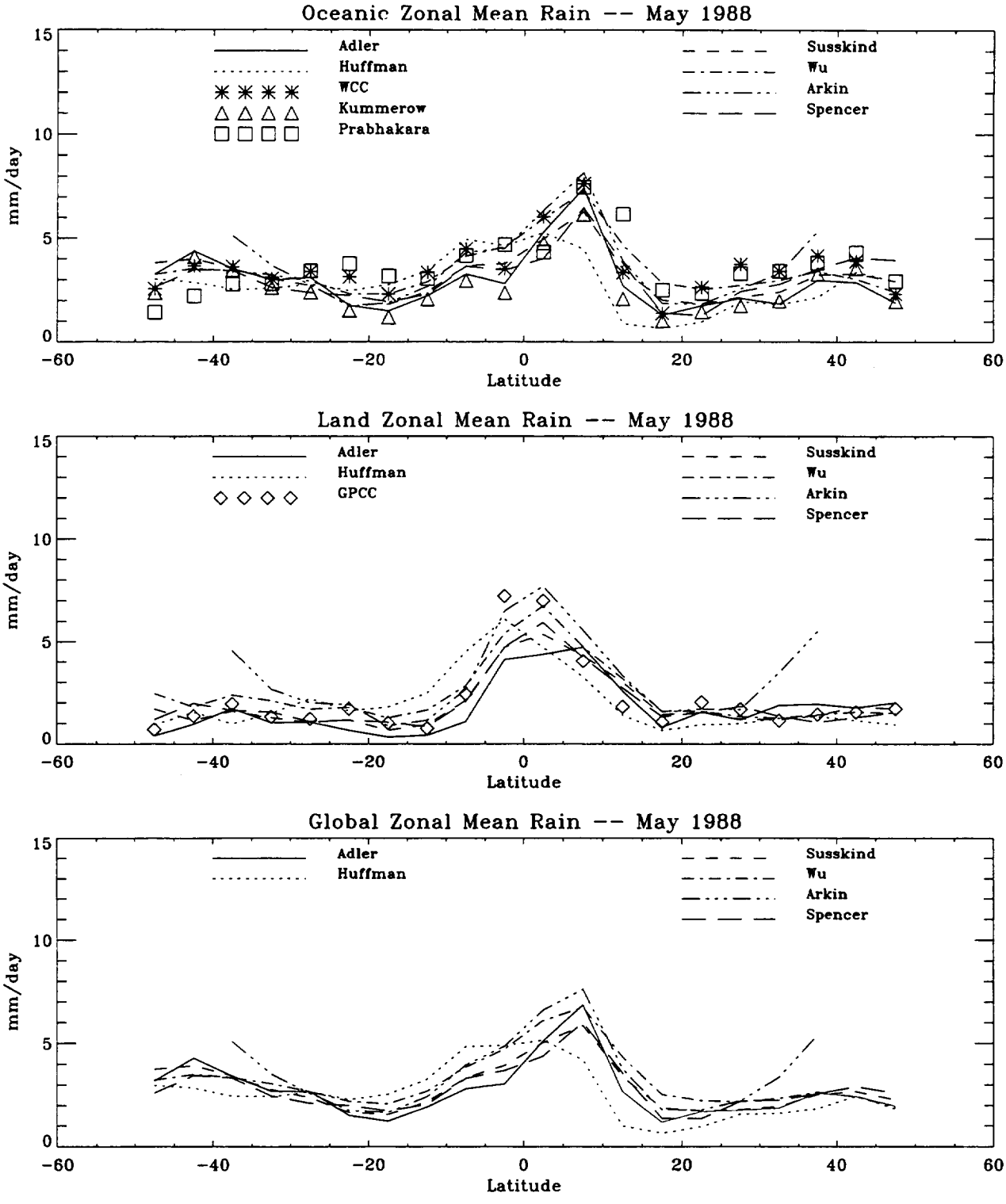

Figure 11: Same as Figure 9, except for May 1988.

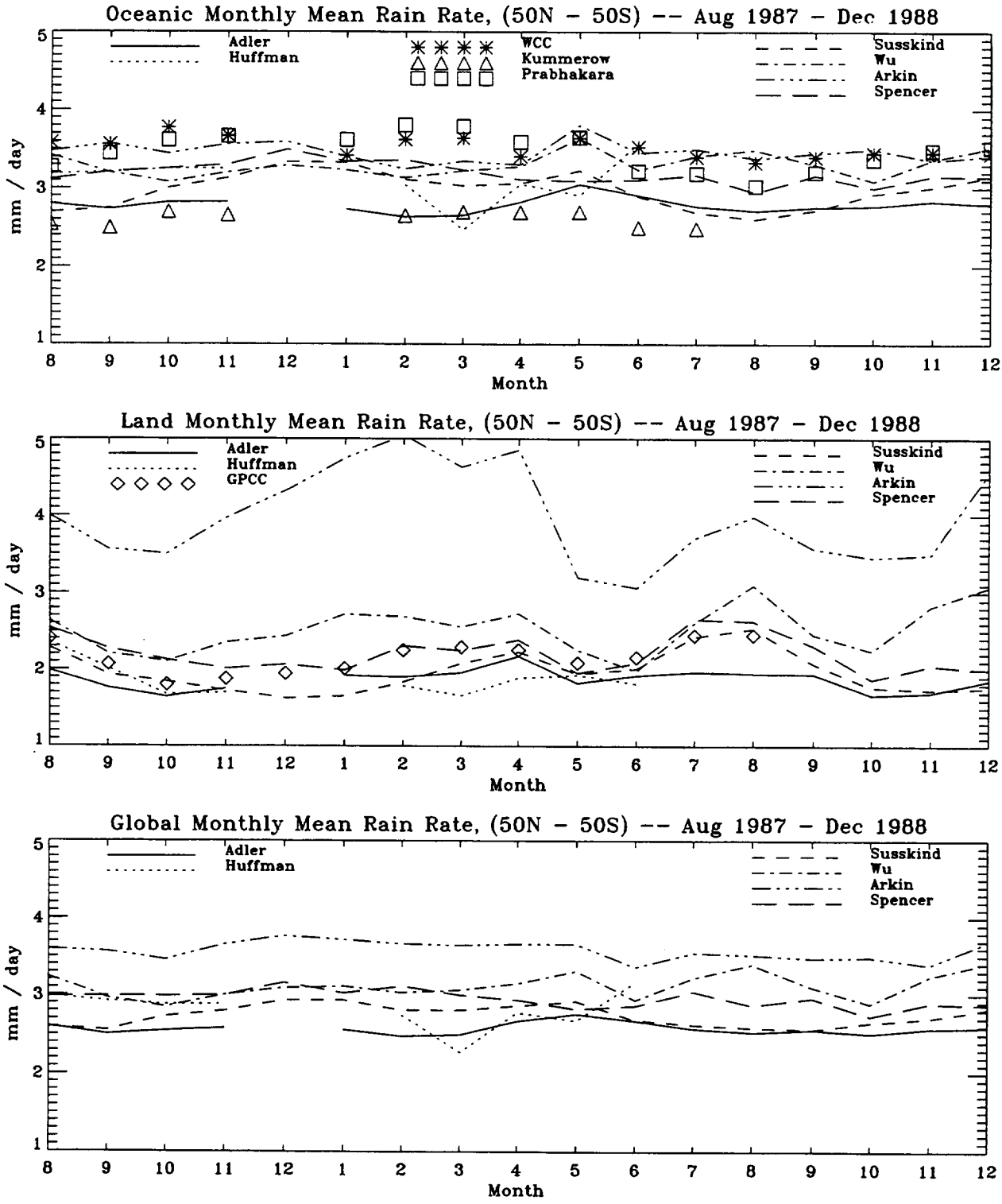

Figure 12: Time series of the global (50°N - 50°S) average for all algorithms over the oceans (upper panel), land (middle panel), and over both ocean and land (lower panel) from August 1987 to December 1988.

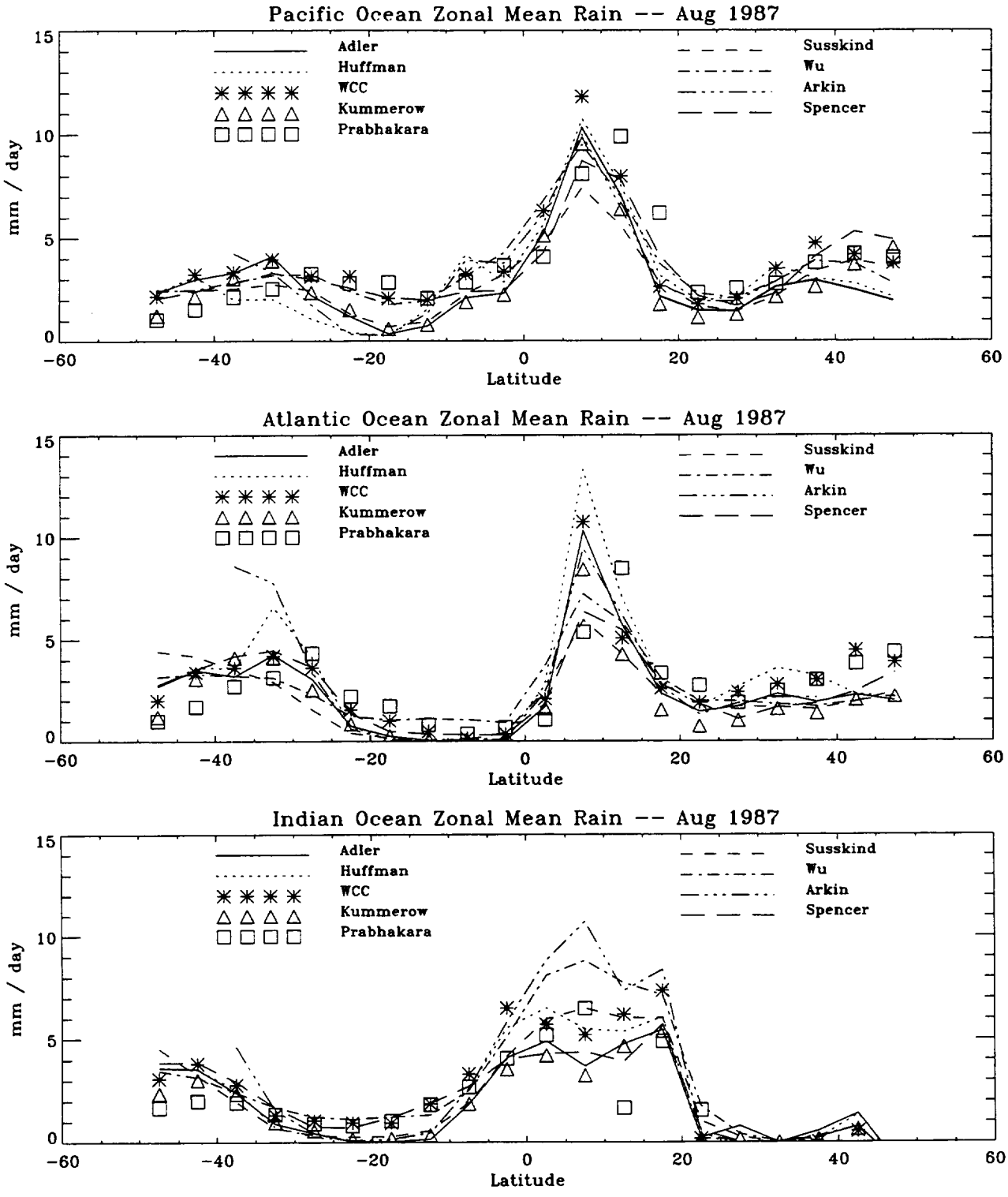

Figure 13.1: Zonal mean rain rates for the Pacific (upper panel), Atlantic (middle panel), and Indian ocean sector (lower panel) for August 1987.

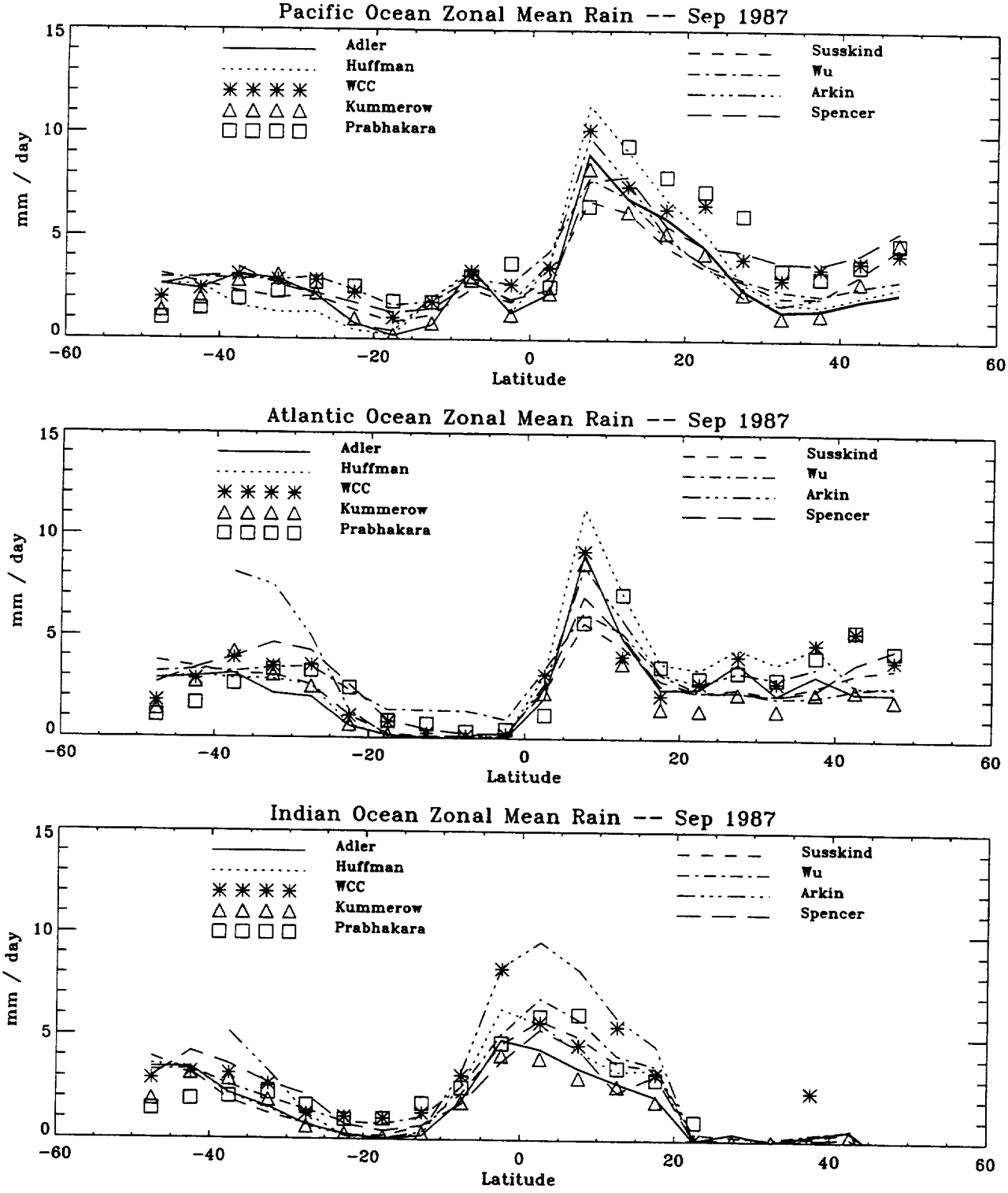

Figure 13.2: Zonal mean rain rates for the Pacific (upper panel), Atlantic (middle panel), and Indian ocean sector (lower panel) for September 1987.

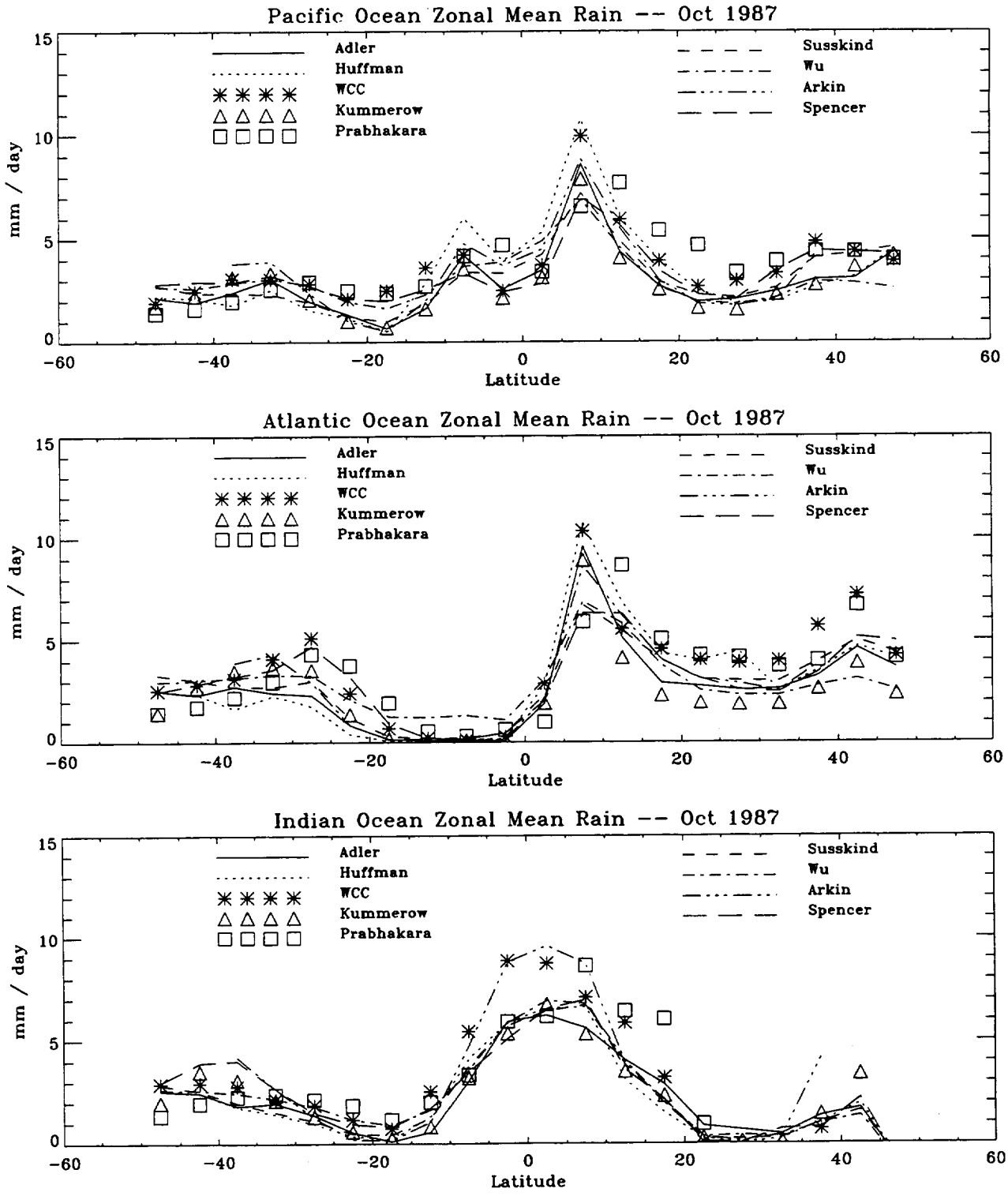

Figure 13.3: Zonal mean rain rates for the Pacific (upper panel), Atlantic (middle panel), and Indian ocean sector (lower panel) for October 1987.

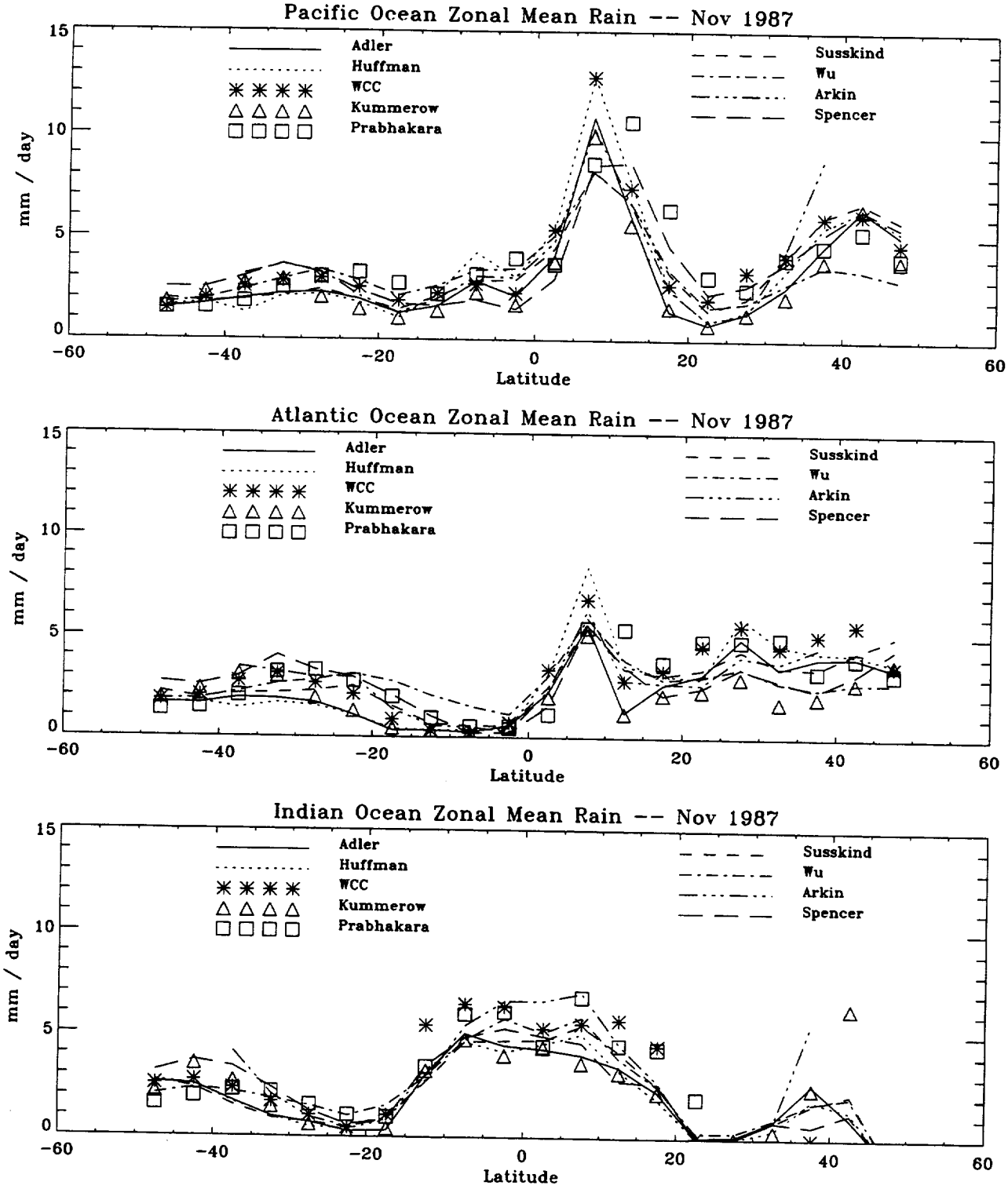

Figure 13.4: Zonal mean rain rates for the Pacific (upper panel), Atlantic (middle panel), and Indian ocean sector (lower panel) for November 1987.

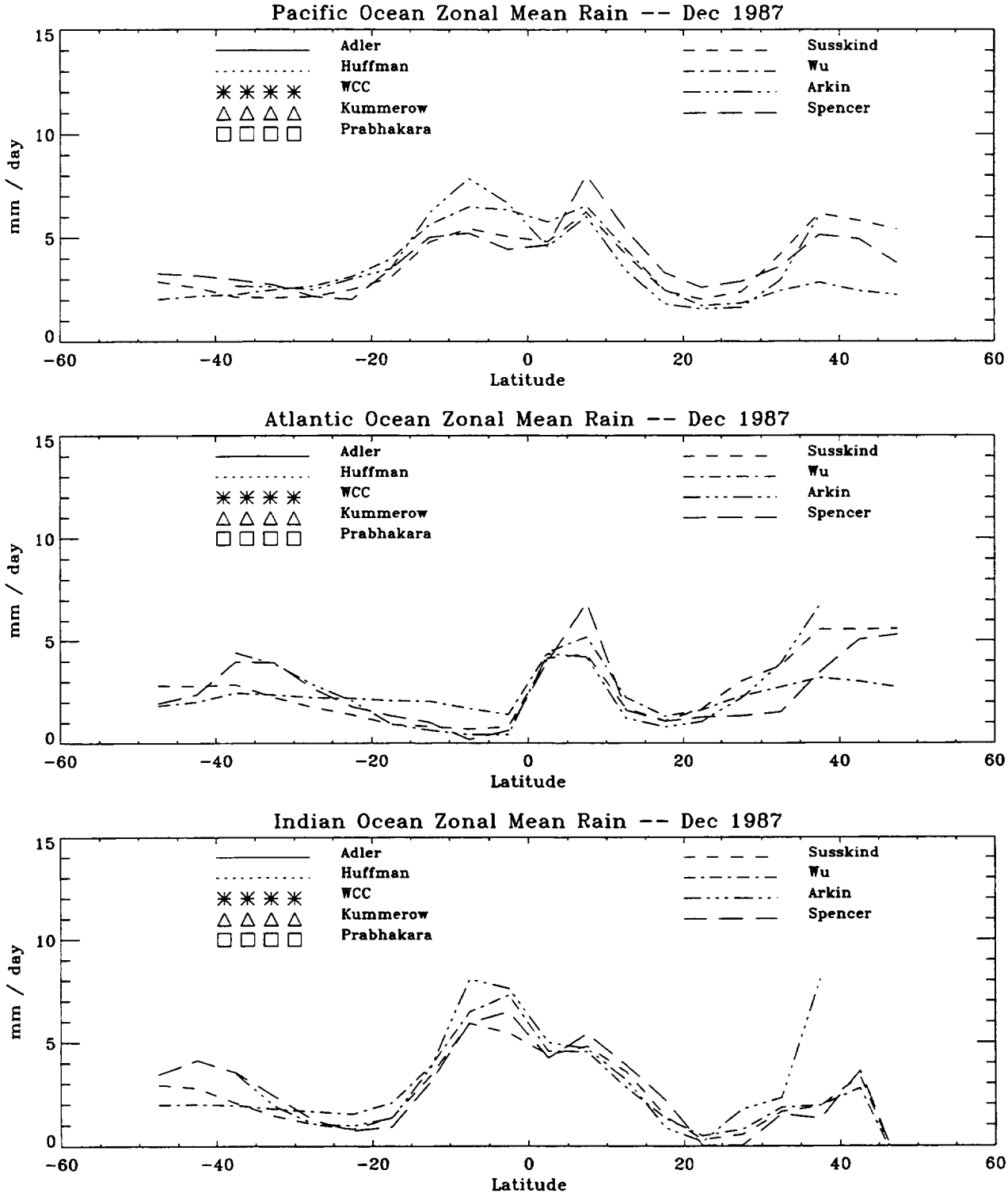

Figure 13.5: Zonal mean rain rates for the Pacific (upper panel), Atlantic (middle panel), and Indian ocean sector (lower panel) for December 1987.

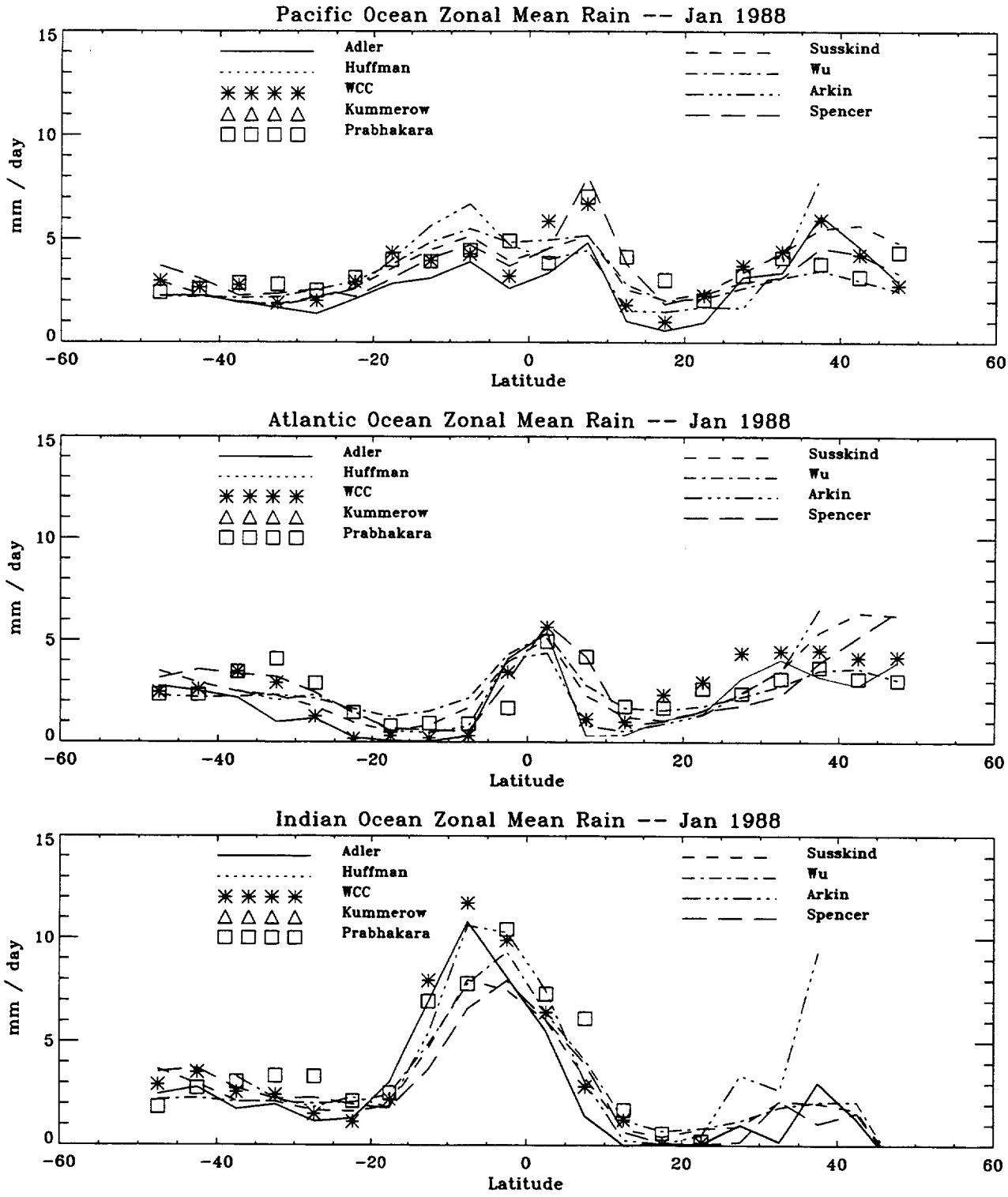

Figure 13.6: Zonal mean rain rates for the Pacific (upper panel), Atlantic (middle panel), and Indian ocean sector (lower panel) for January 1988.

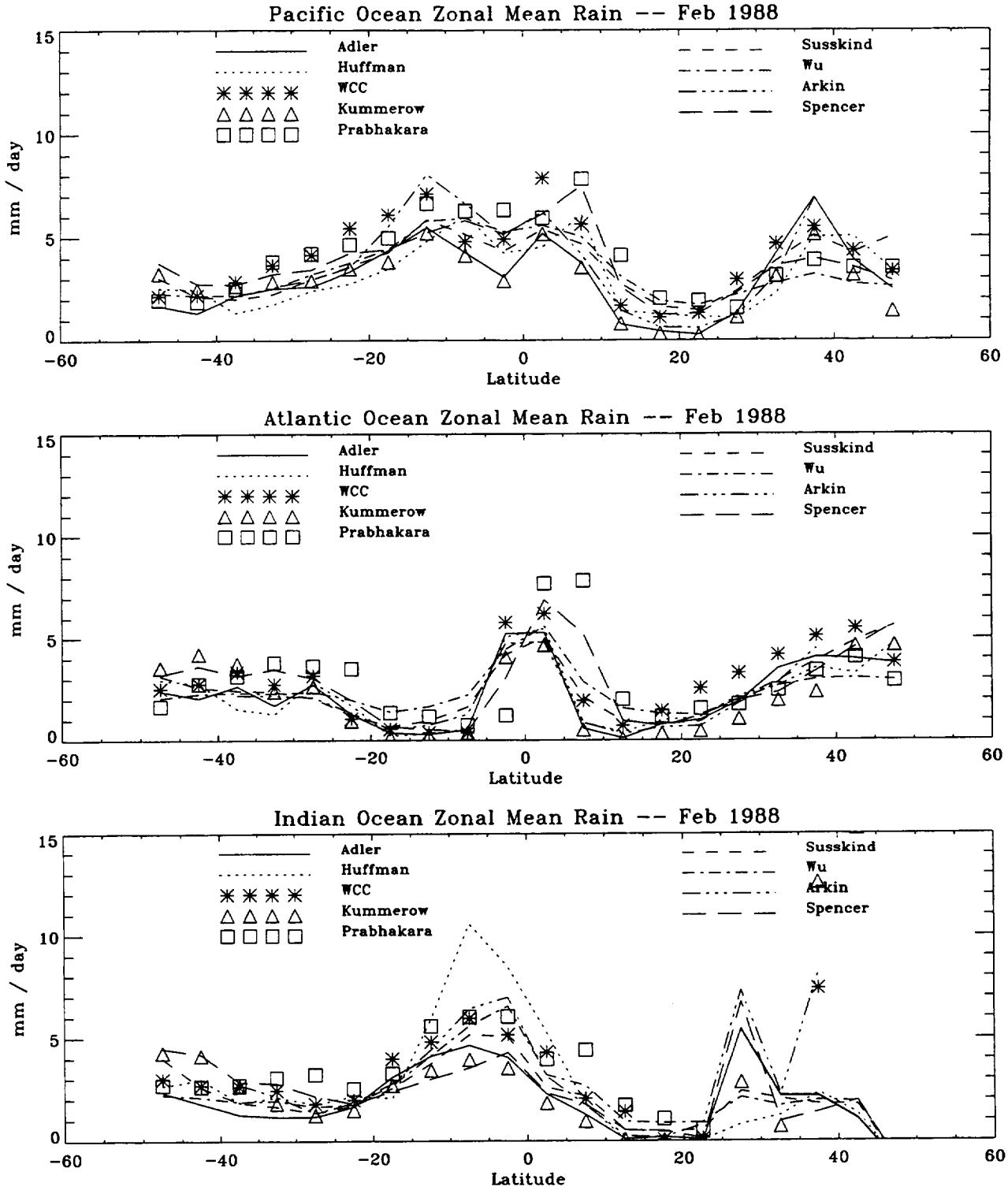

Figure 13.7: Zonal mean rain rates for the Pacific (upper panel), Atlantic (middle panel), and Indian ocean sector (lower panel) for February 1988.

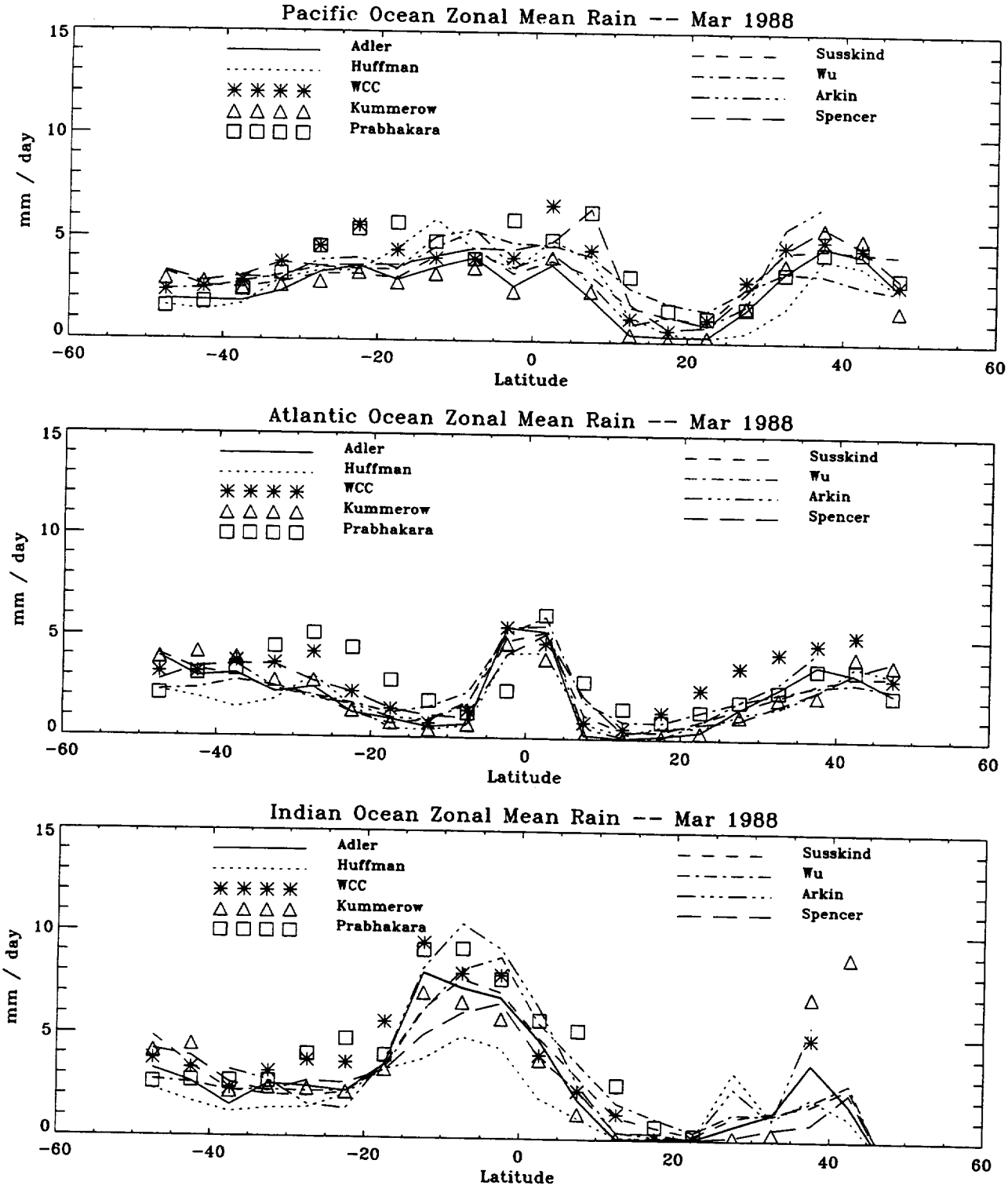

Figure 13.8: Zonal mean rain rates for the Pacific (upper panel), Atlantic (middle panel), and Indian ocean sector (lower panel) for March 1988.

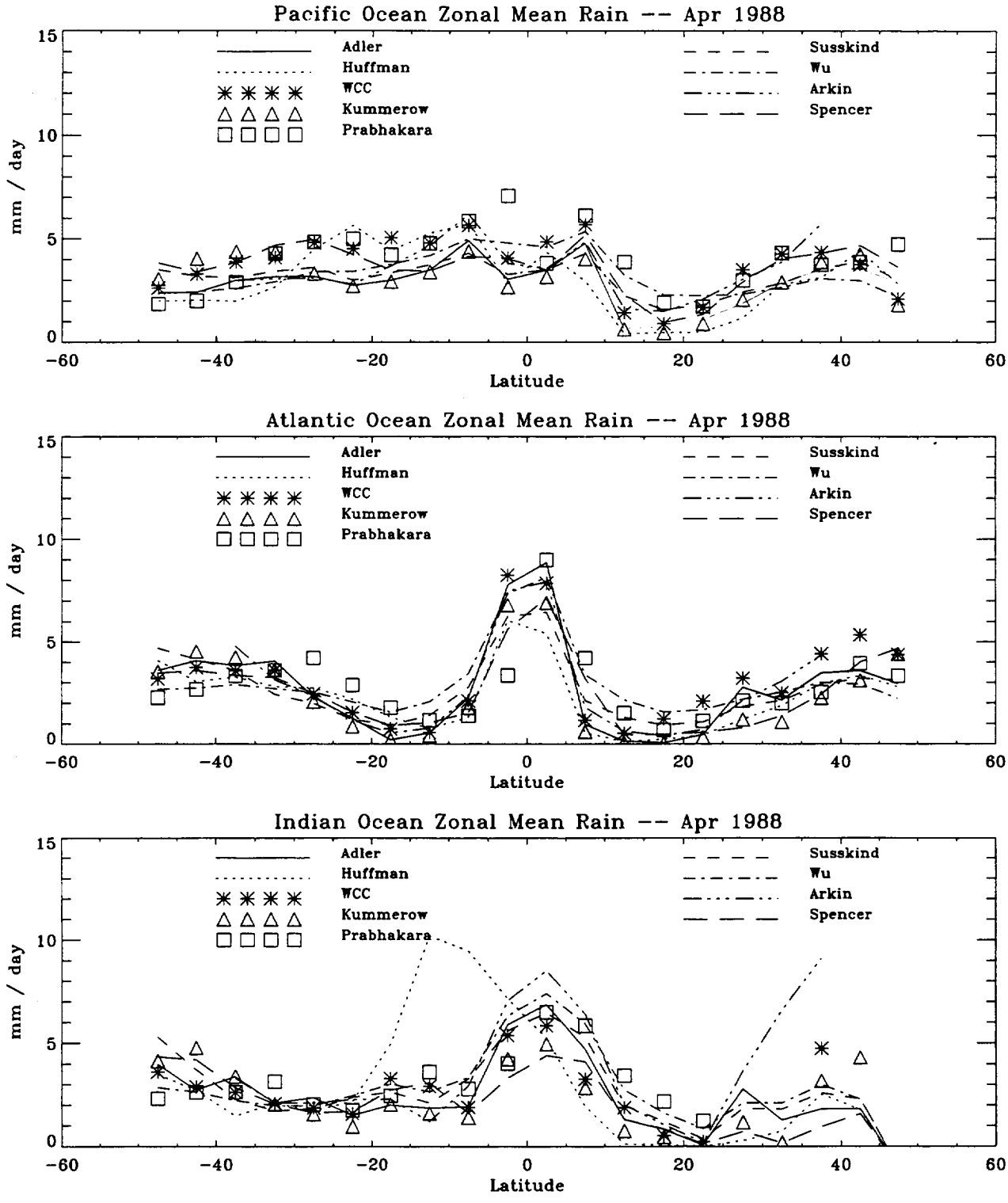

Figure 13.9: Zonal mean rain rates for the Pacific (upper panel), Atlantic (middle panel), and Indian ocean sector (lower panel) for April 1988.

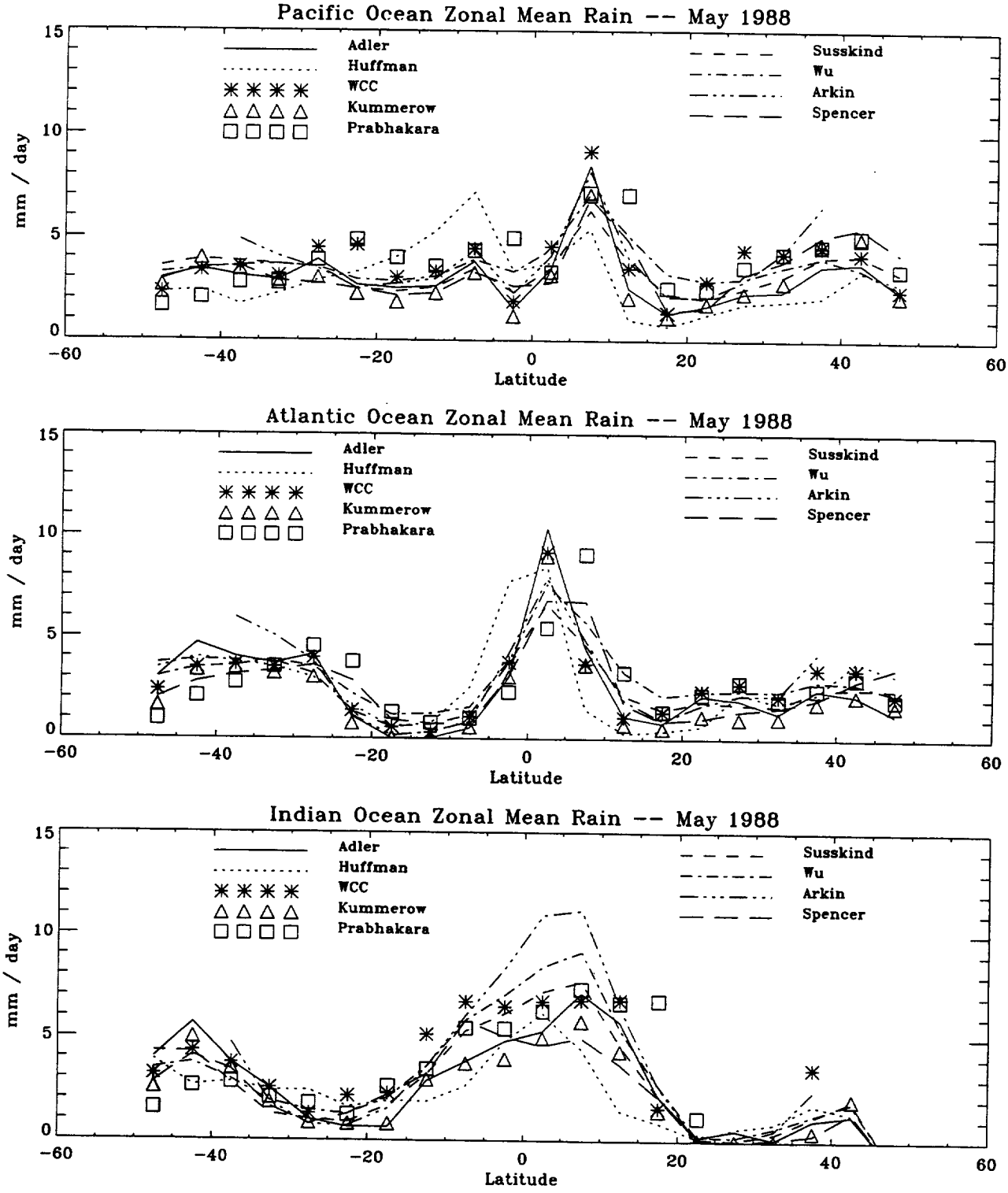

Figure 13.10: Zonal mean rain rates for the Pacific (upper panel), Atlantic (middle panel), and Indian ocean sector (lower panel) for May 1988.

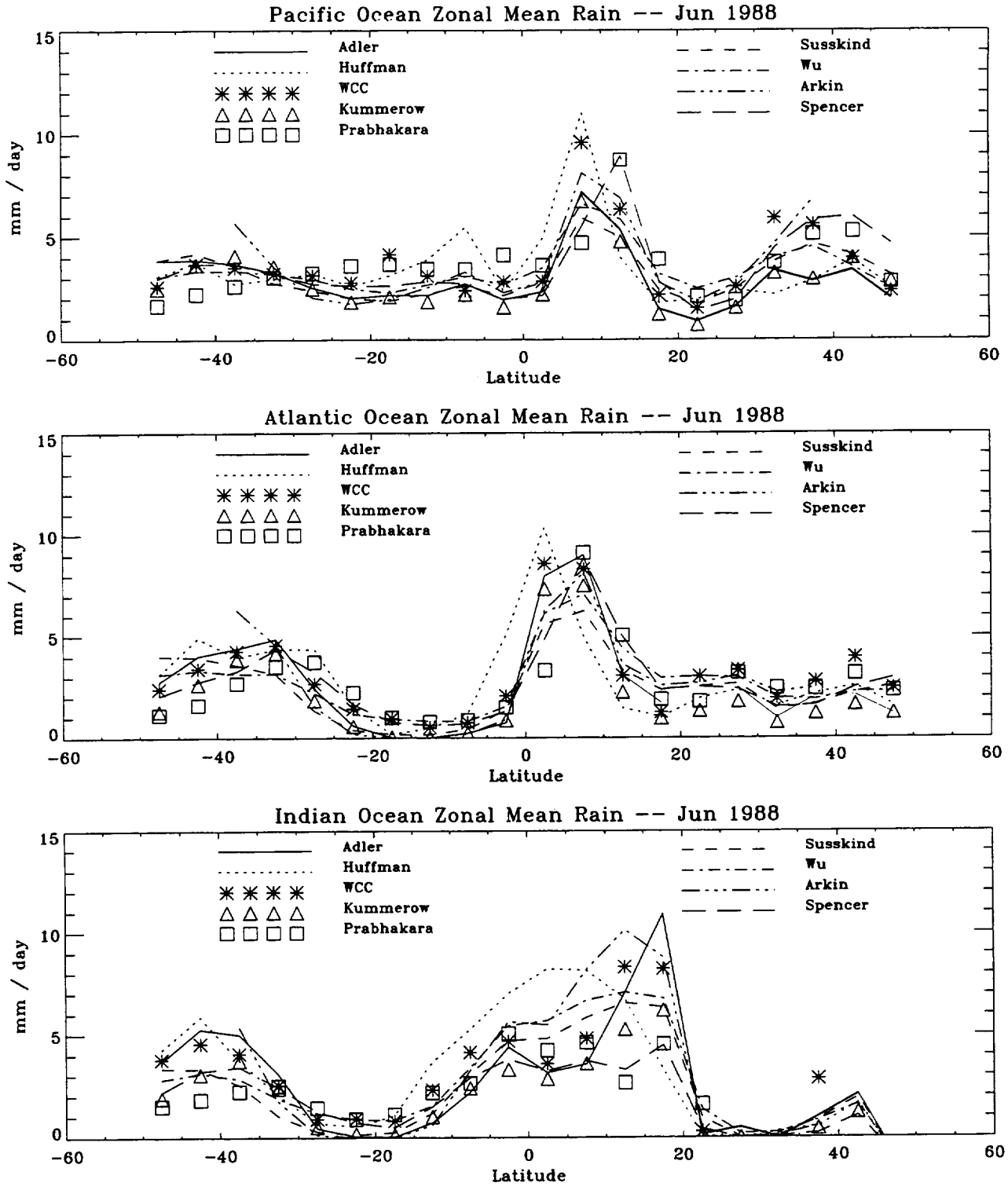

Figure 13.11: Zonal mean rain rates for the Pacific (upper panel), Atlantic (middle panel), and Indian ocean sector (lower panel) for June 1988.

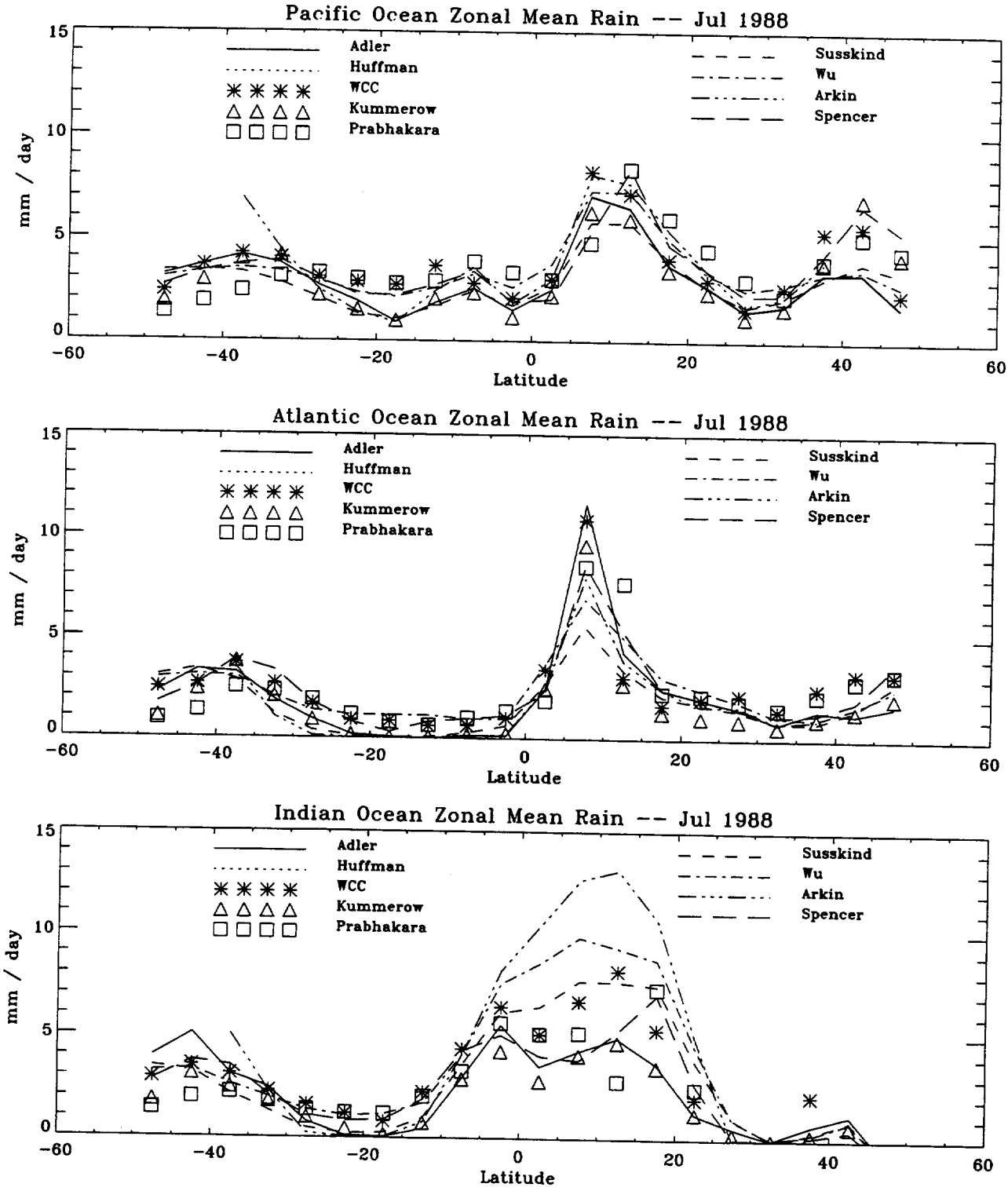

Figure 13.12: Zonal mean rain rates for the Pacific (upper panel), Atlantic (middle panel), and Indian ocean sector (lower panel) for July 1988.

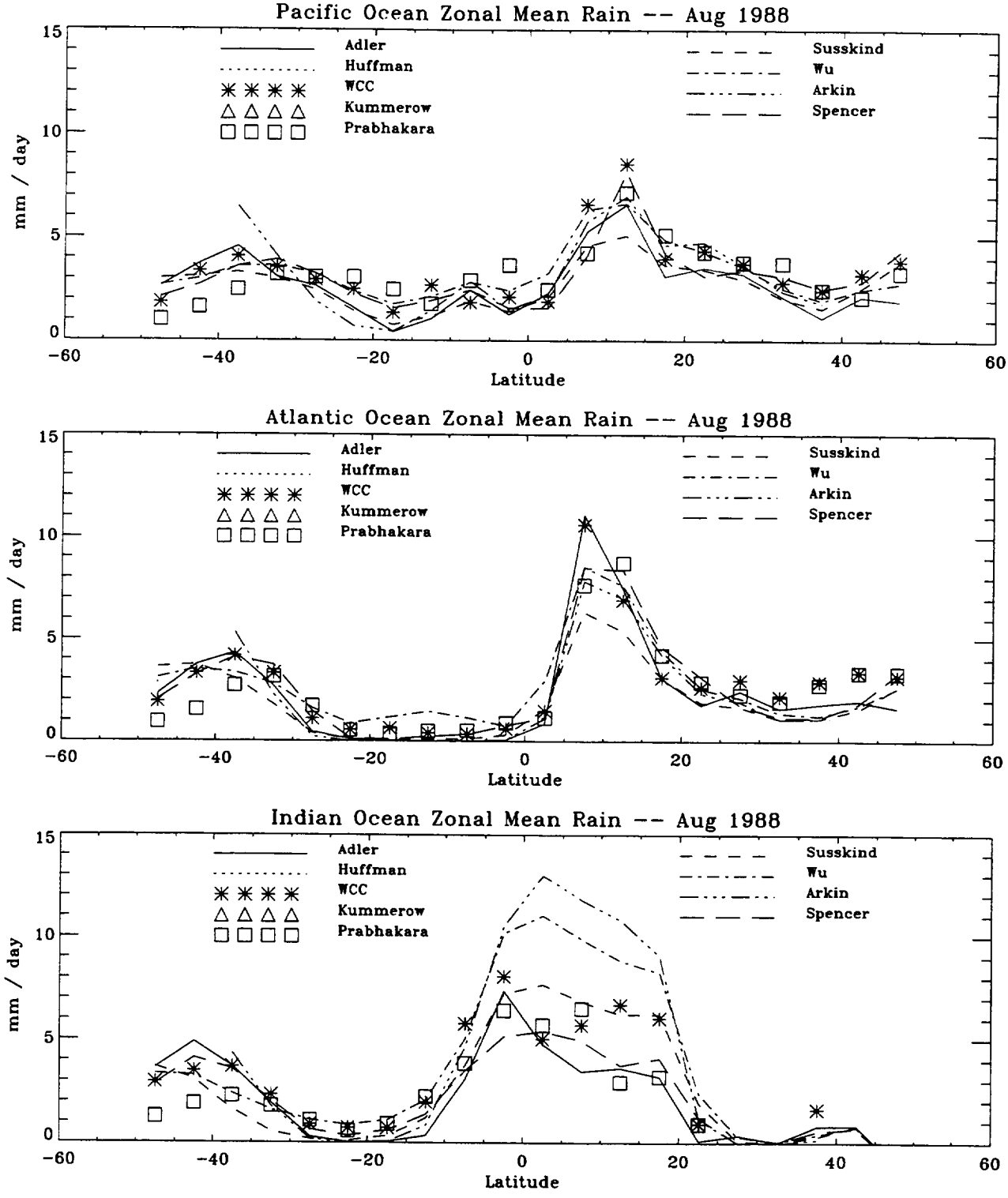

Figure 13.13: Zonal mean rain rates for the Pacific (upper panel), Atlantic (middle panel), and Indian ocean sector (lower panel) for August 1988.

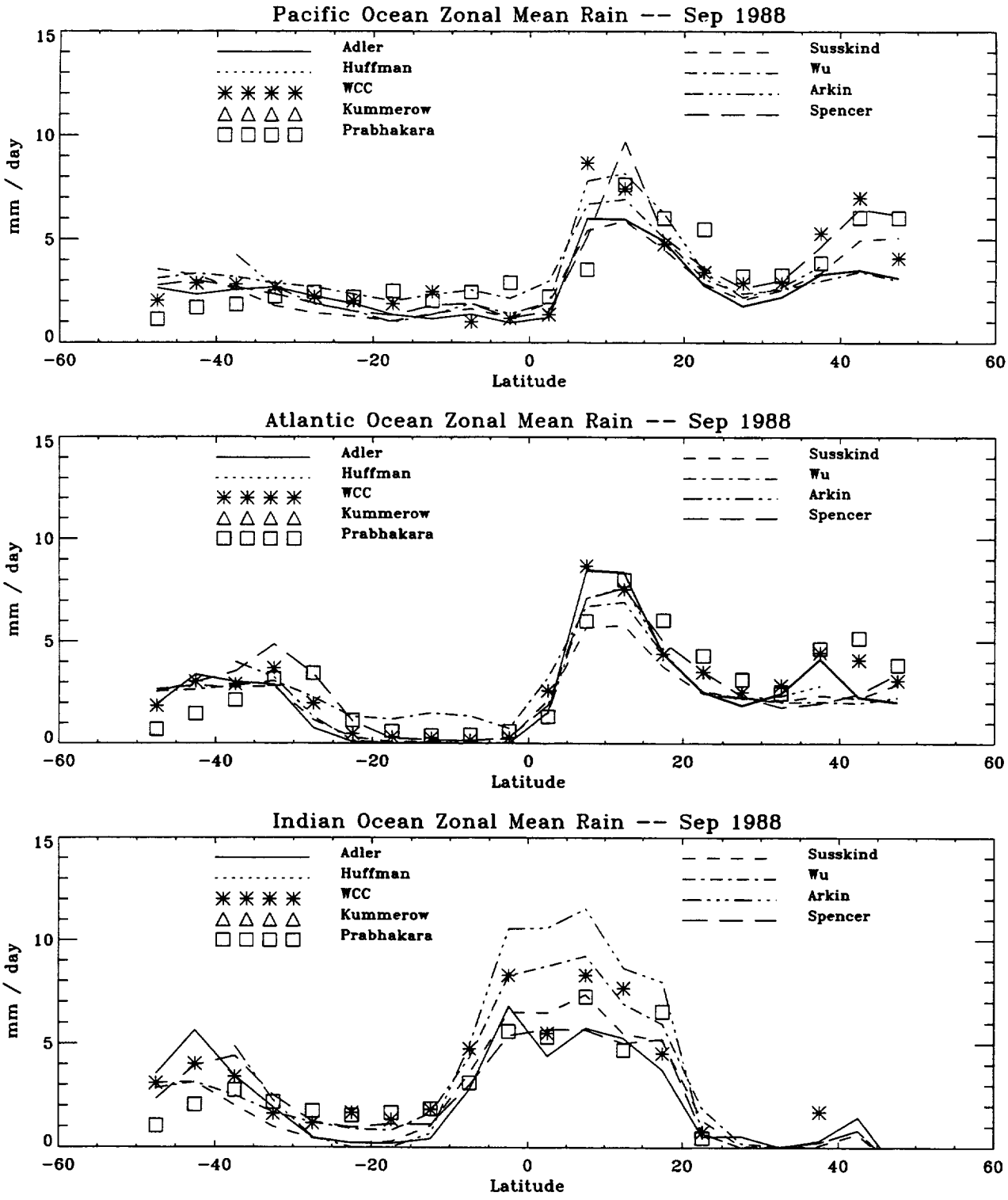

Figure 13.14: Zonal mean rain rates for the Pacific (upper panel), Atlantic (middle panel), and Indian ocean sector (lower panel) for September 1988.

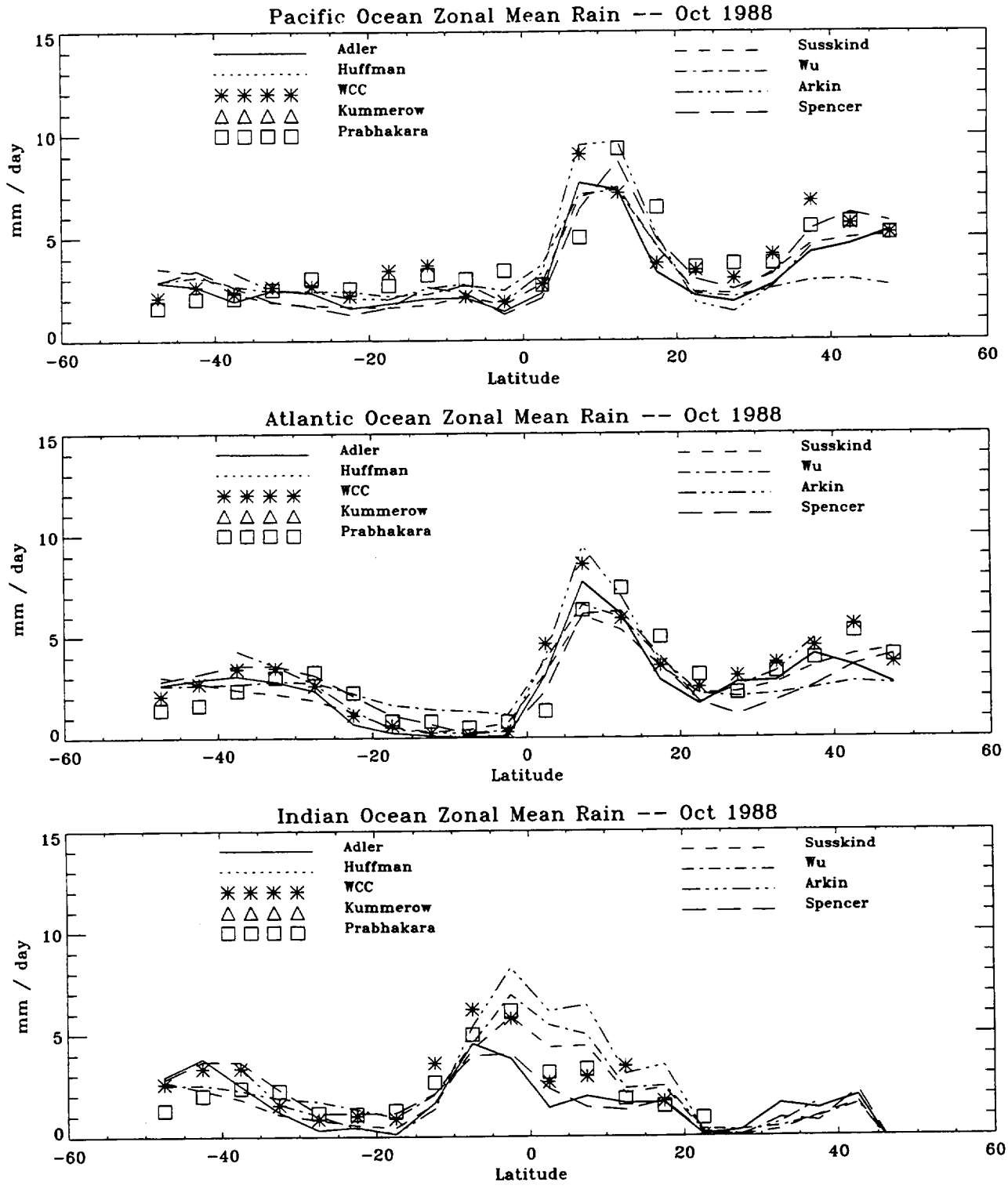

Figure 13.15: Zonal mean rain rates for the Pacific (upper panel), Atlantic (middle panel), and Indian ocean sector (lower panel) for October 1988.

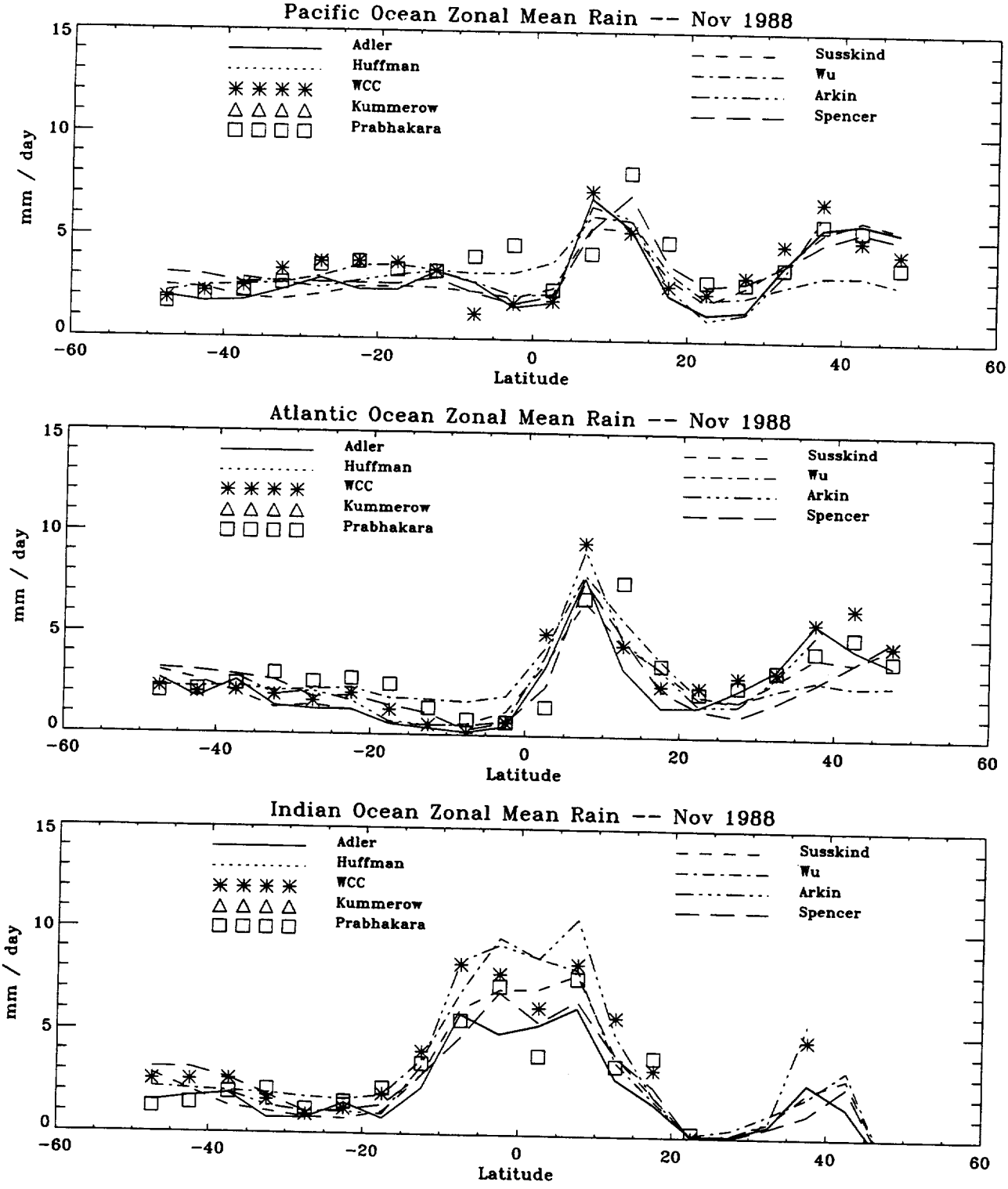

Figure 13.16: Zonal mean rain rates for the Pacific (upper panel), Atlantic (middle panel), and Indian ocean sector (lower panel) for November 1988.

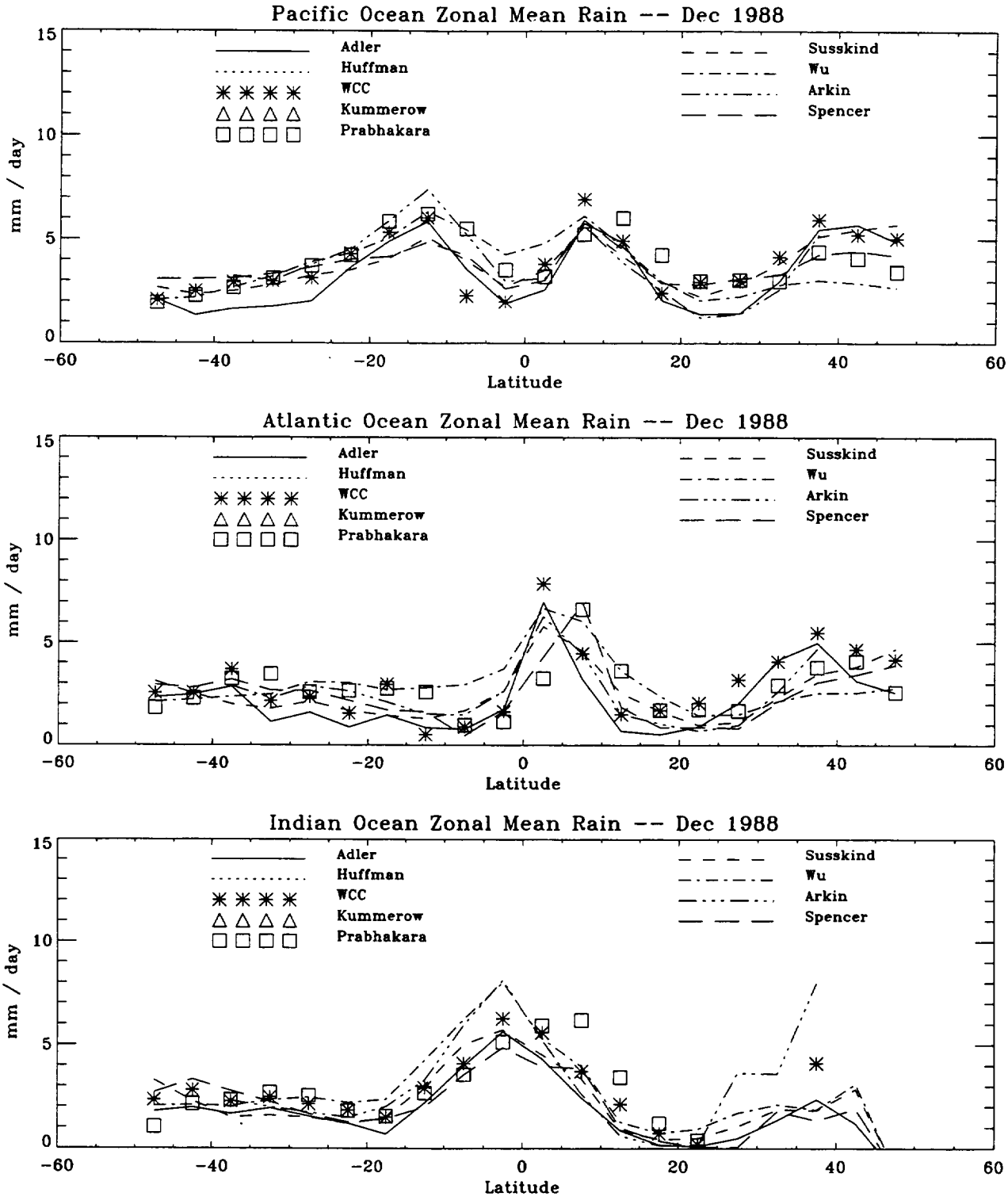

Figure 13.17: Zonal mean rain rates for the Pacific (upper panel), Atlantic (middle panel), and Indian ocean sector (lower panel) for December 1988.

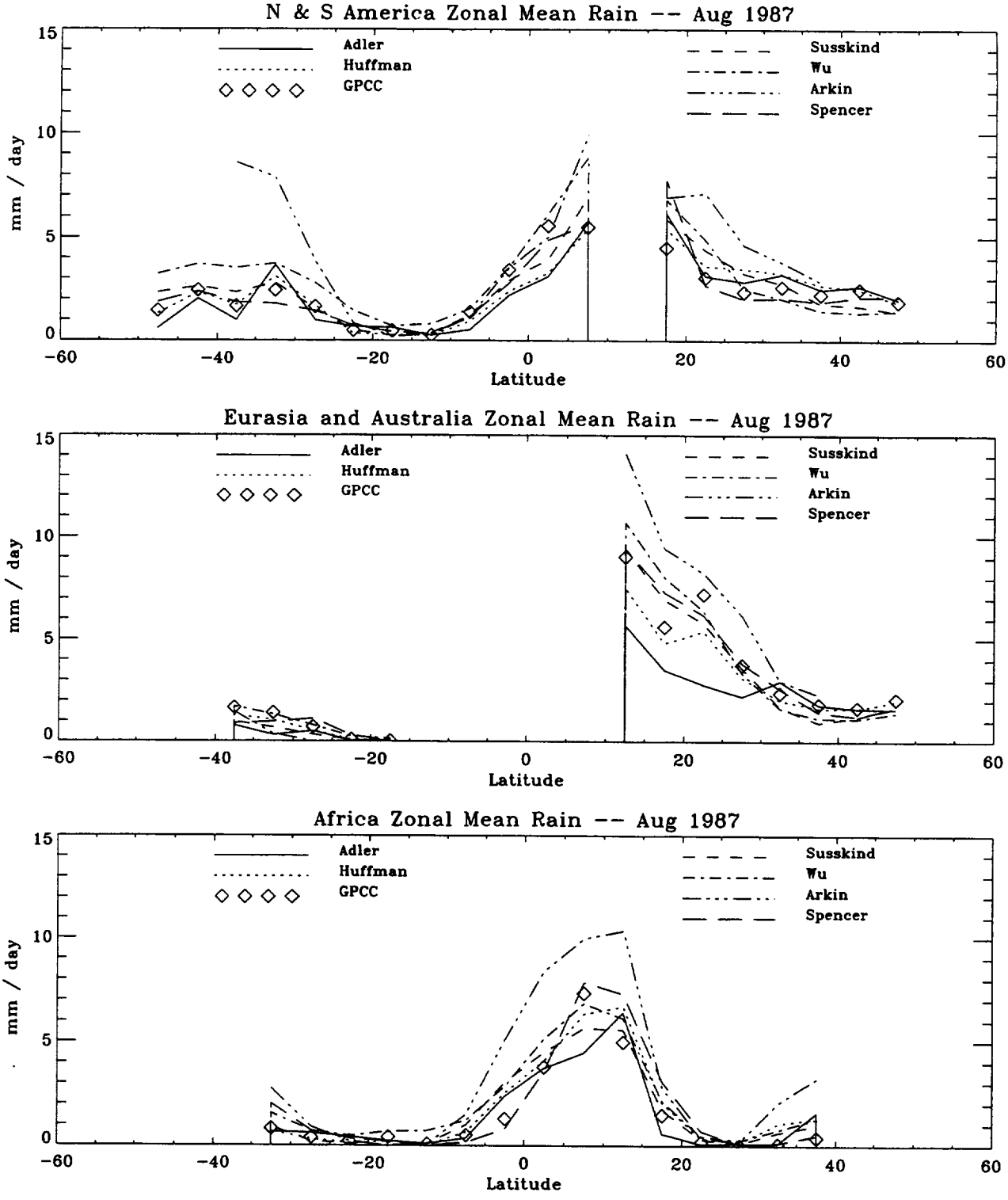

Figure 14.1: Zonal mean rain rate for the north and south American (upper panel), Australia and Eurasia (middle panel), and Africa land sector (lower panel) for August 1987.

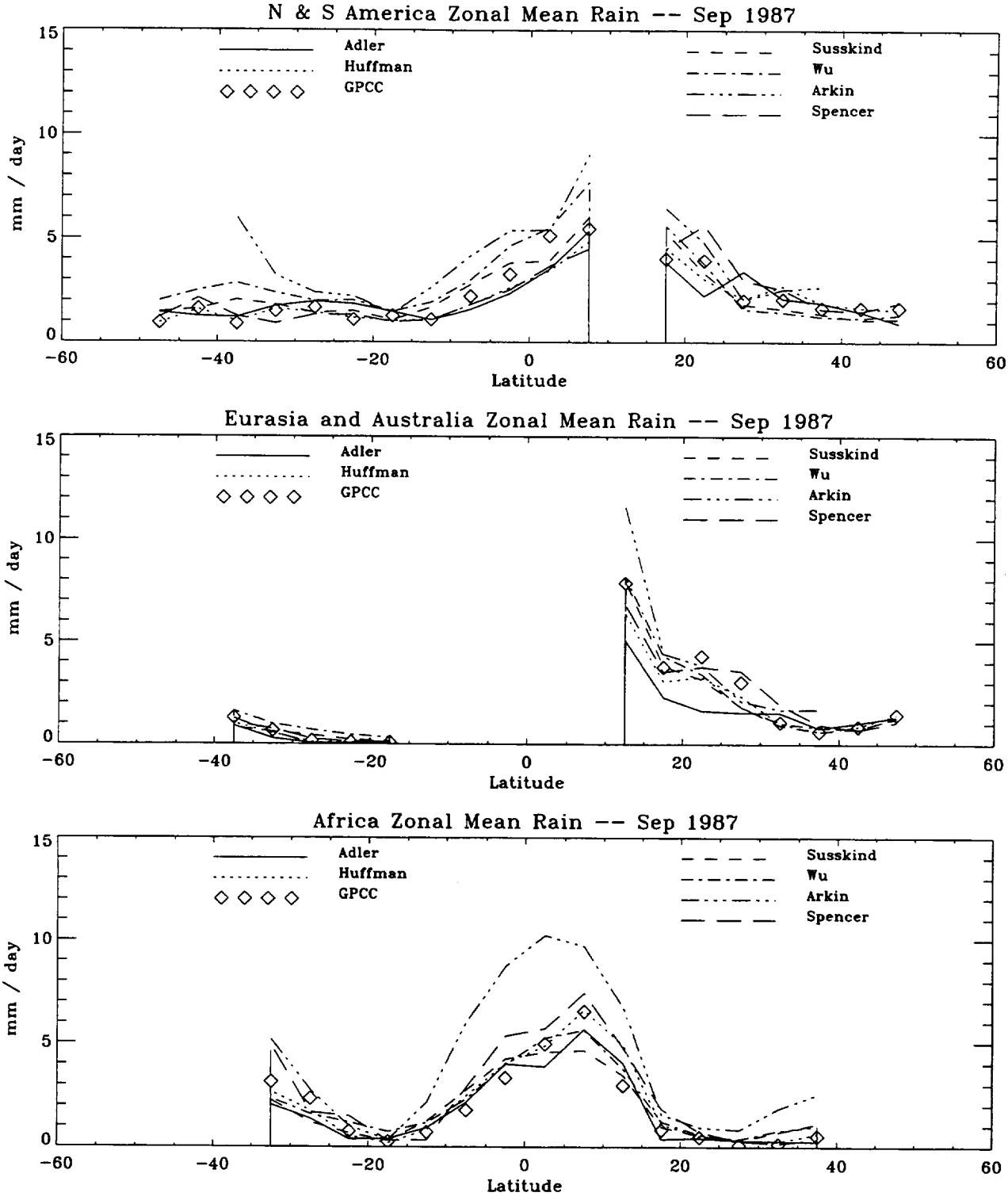

Figure 14.2: Zonal mean rain rate for the north and south American (upper panel), Australia and Eurasia (middle panel), and Africa land sector (lower panel) for September 1987.

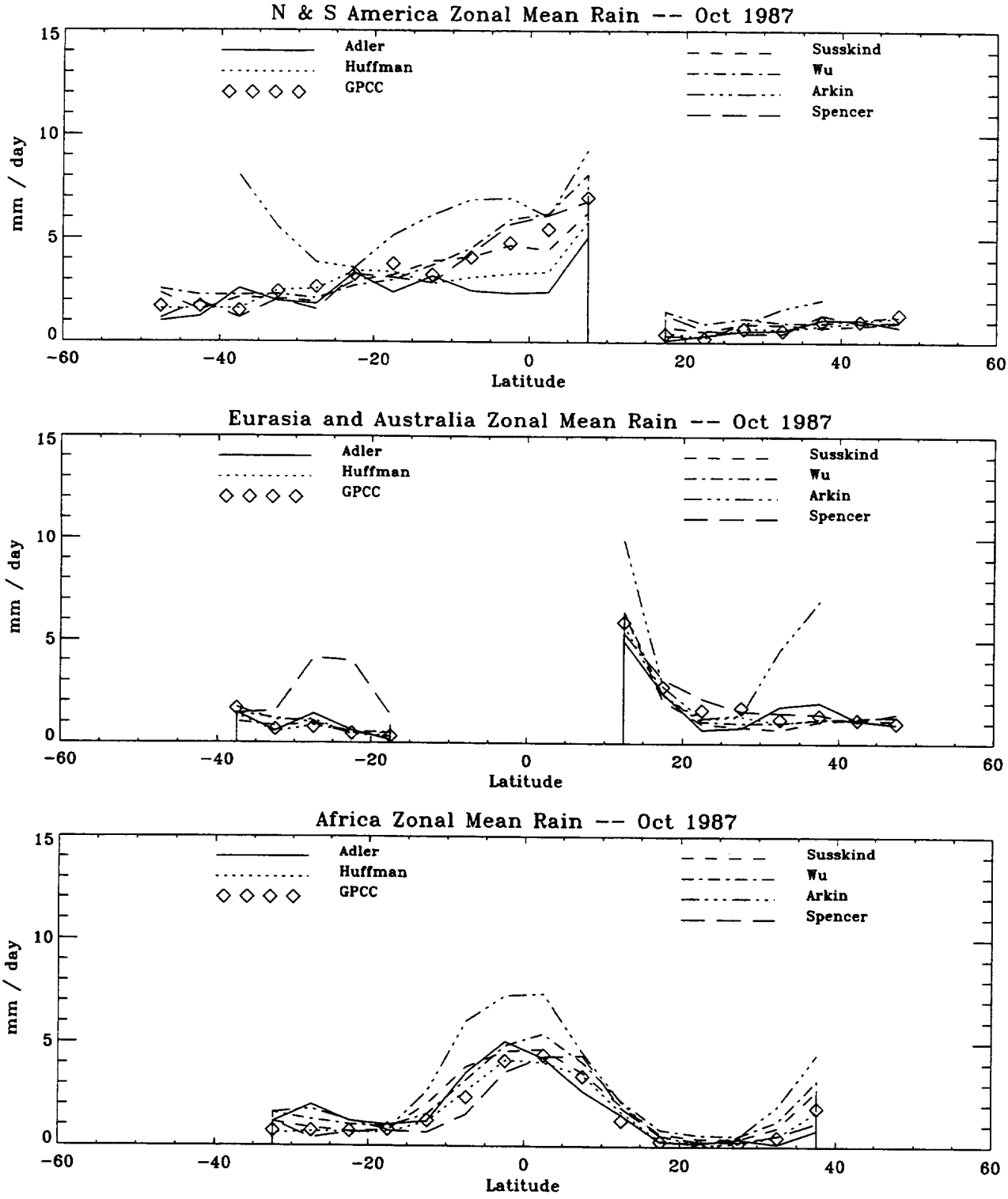

Figure 14.3: Zonal mean rain rate for the north and south American (upper panel), Australia and Eurasia (middle panel), and Africa land sector (lower panel) for October 1987.

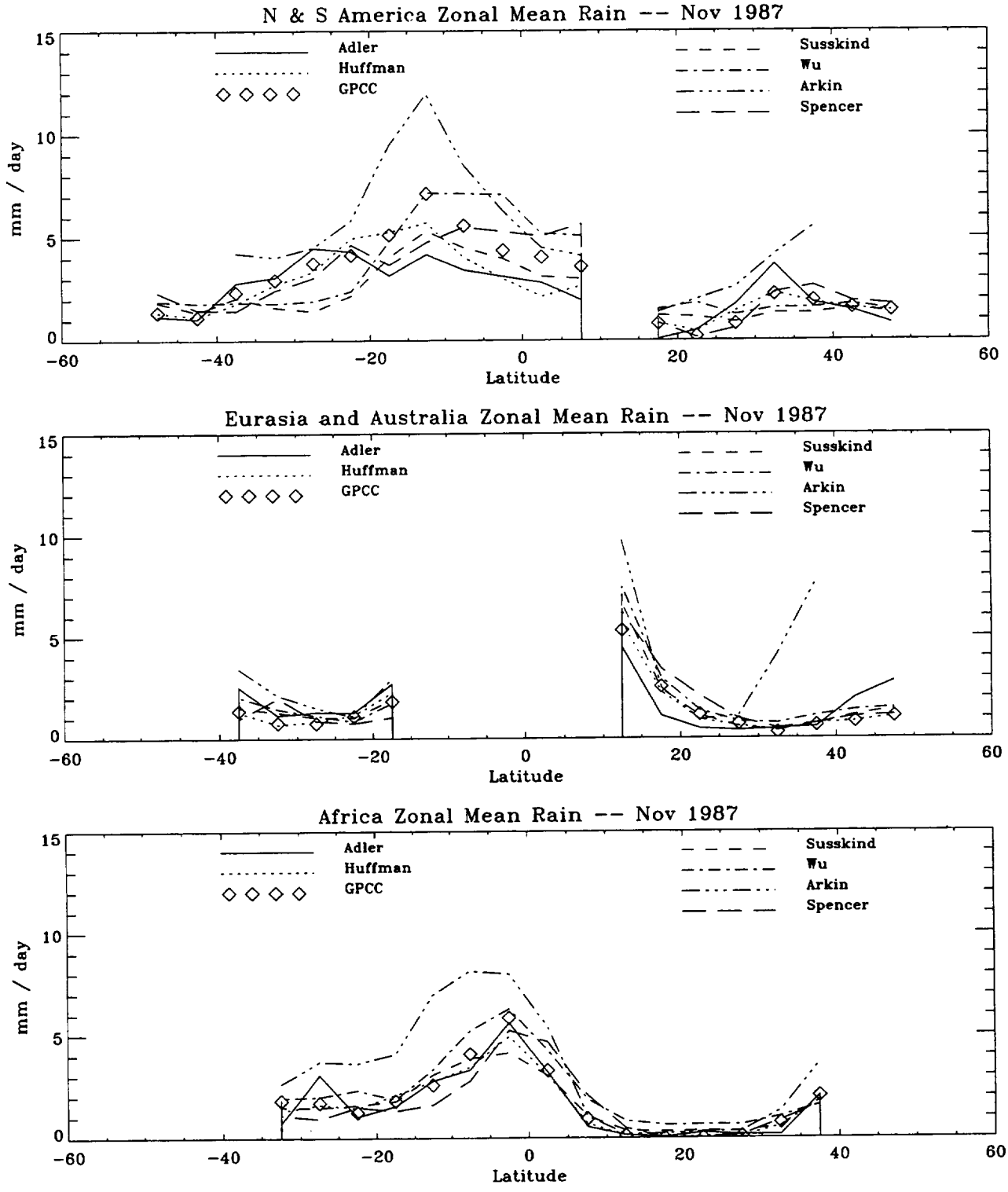

Figure 14.4: Zonal mean rain rate for the north and south American (upper panel), Australia and Eurasia (middle panel), and Africa land sector (lower panel) for November 1987.

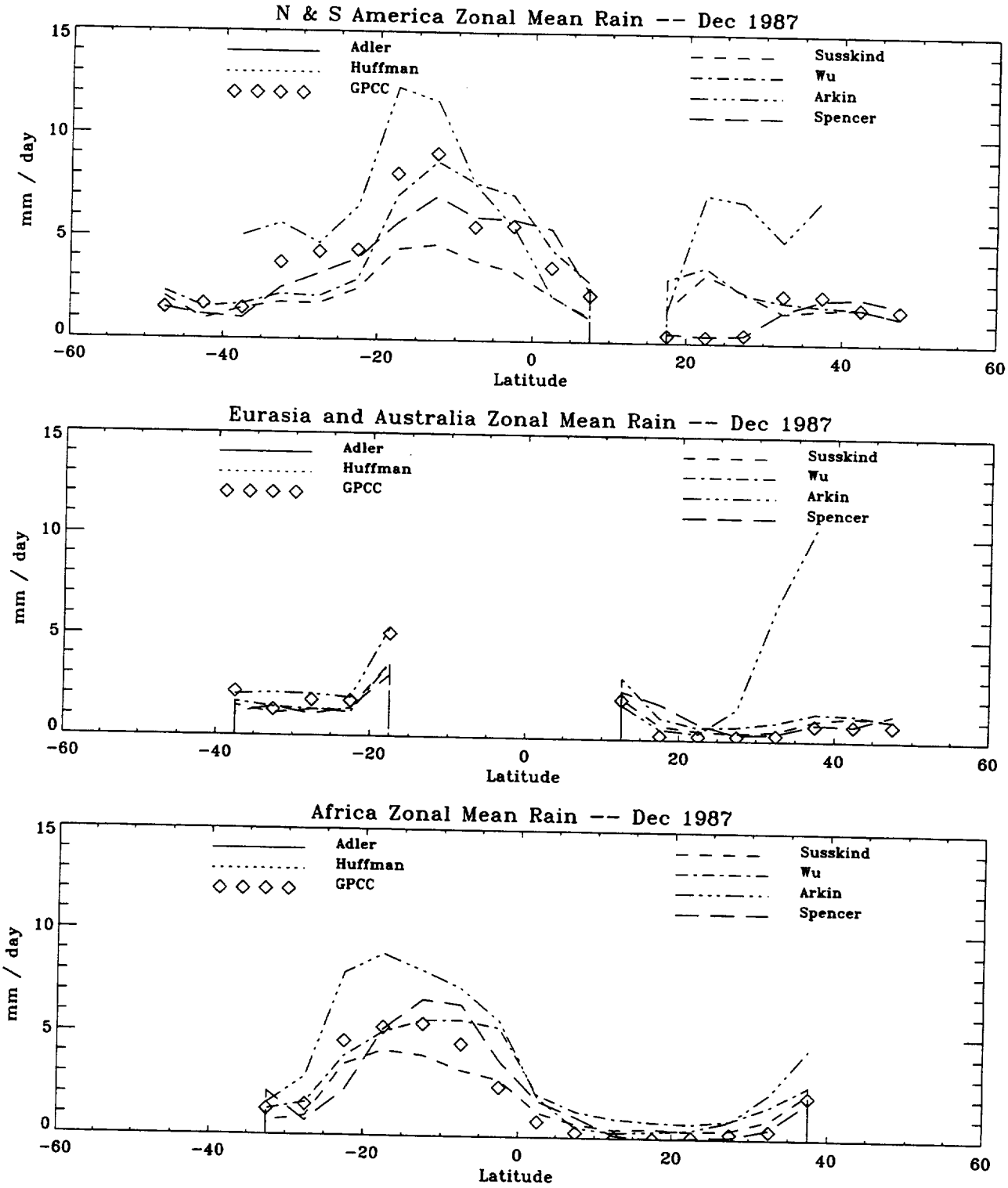

Figure 14.5: Zonal mean rain rate for the north and south American (upper panel), Australia and Eurasia (middle panel), and Africa land sector (lower panel) for December 1987.

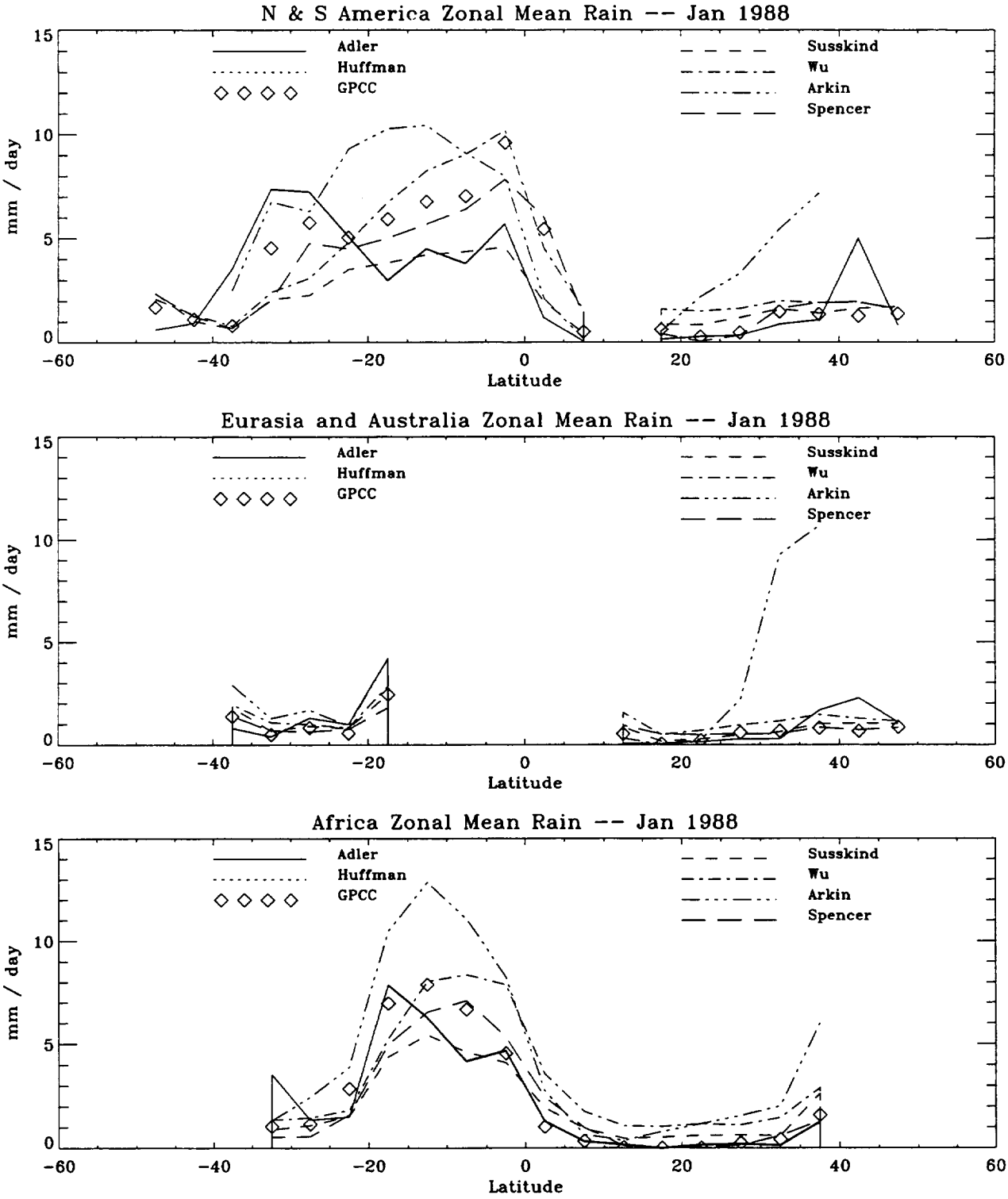

Figure 14.6: Zonal mean rain rate for the north and south American (upper panel), Australia and Eurasia (middle panel), and Africa land sector (lower panel) for January 1988.

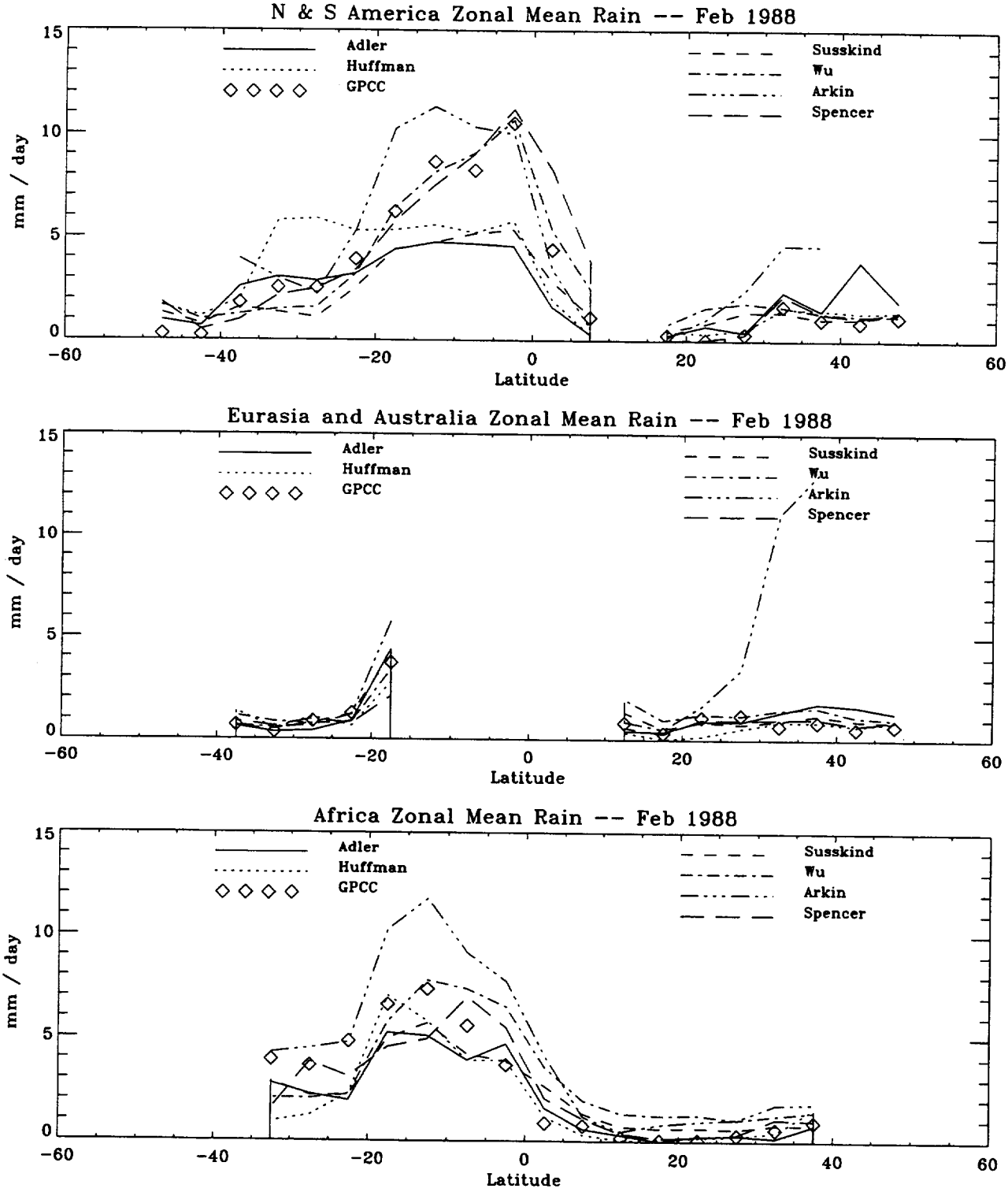

Figure 14.7: Zonal mean rain rate for the north and south American (upper panel), Australia and Eurasia (middle panel), and Africa land sector (lower panel) for February 1988.

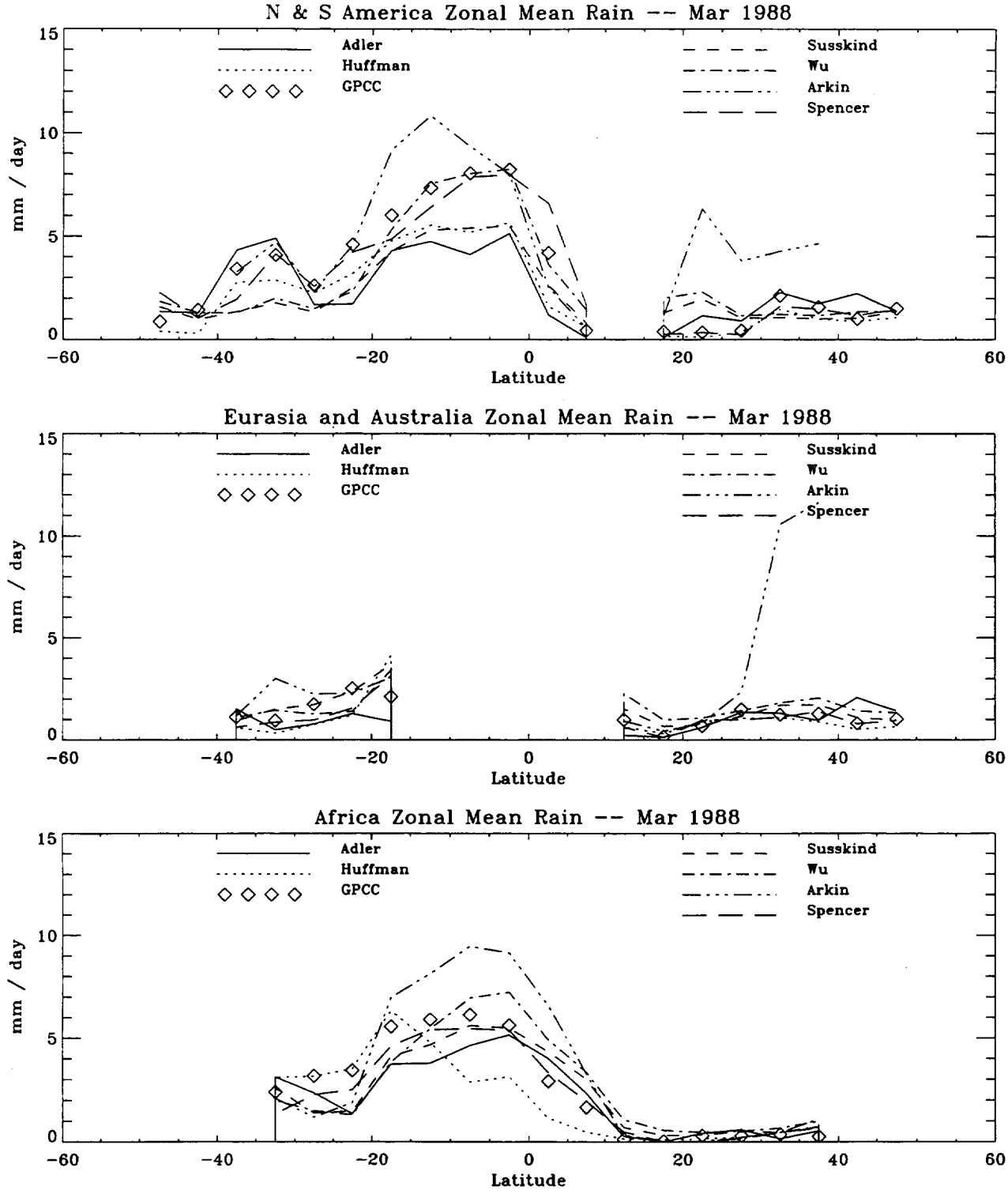

Figure 14.8: Zonal mean rain rate for the north and south American (upper panel), Australia and Eurasia (middle panel), and Africa land sector (lower panel) for March 1988.

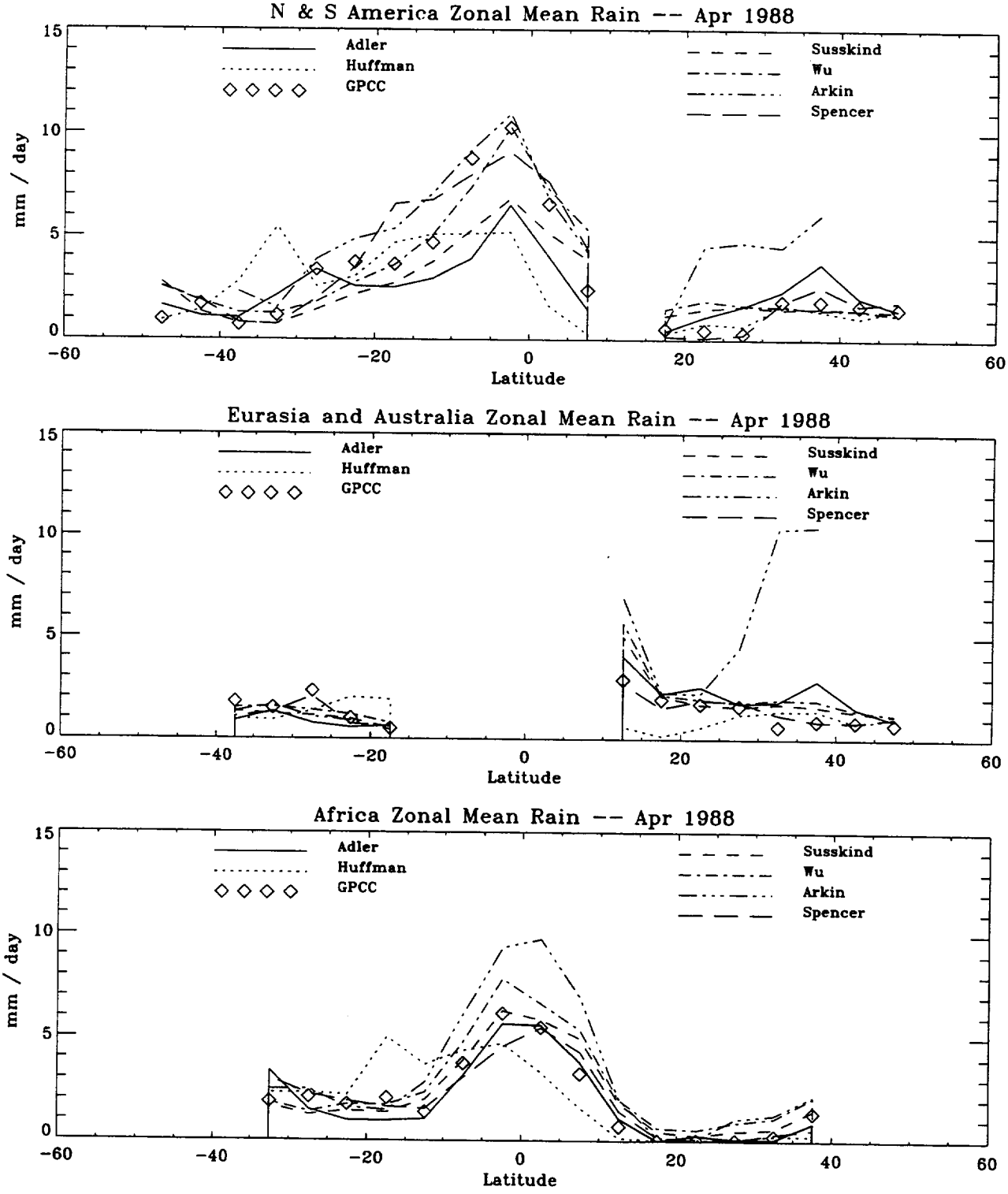

Figure 14.9: Zonal mean rain rate for the north and south American (upper panel), Australia and Eurasia (middle panel), and Africa land sector (lower panel) for April 1988.

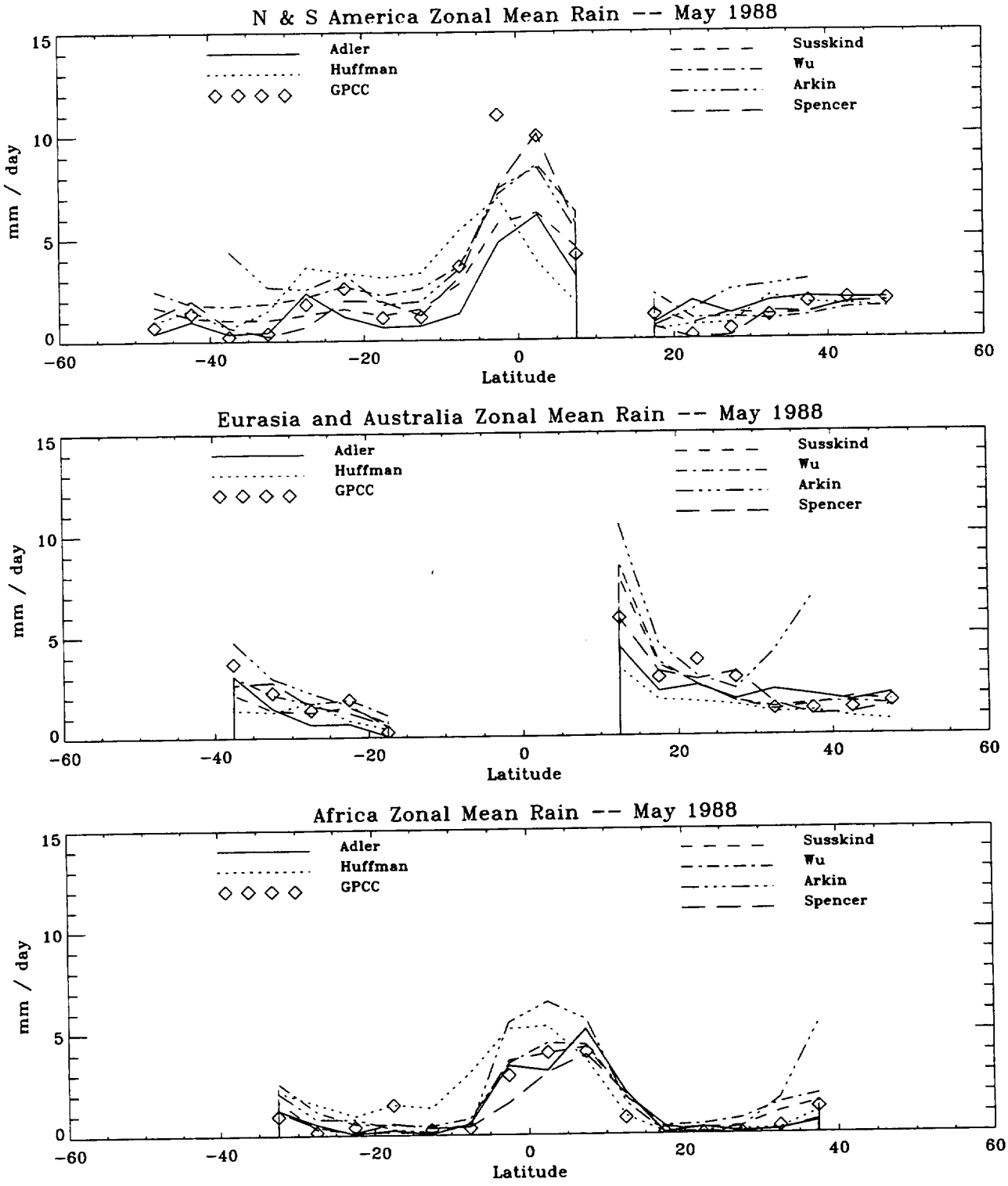

Figure 14.10: Zonal mean rain rate for the north and south American (upper panel), Australia and Eurasia (middle panel), and Africa land sector (lower panel) for May 1988.

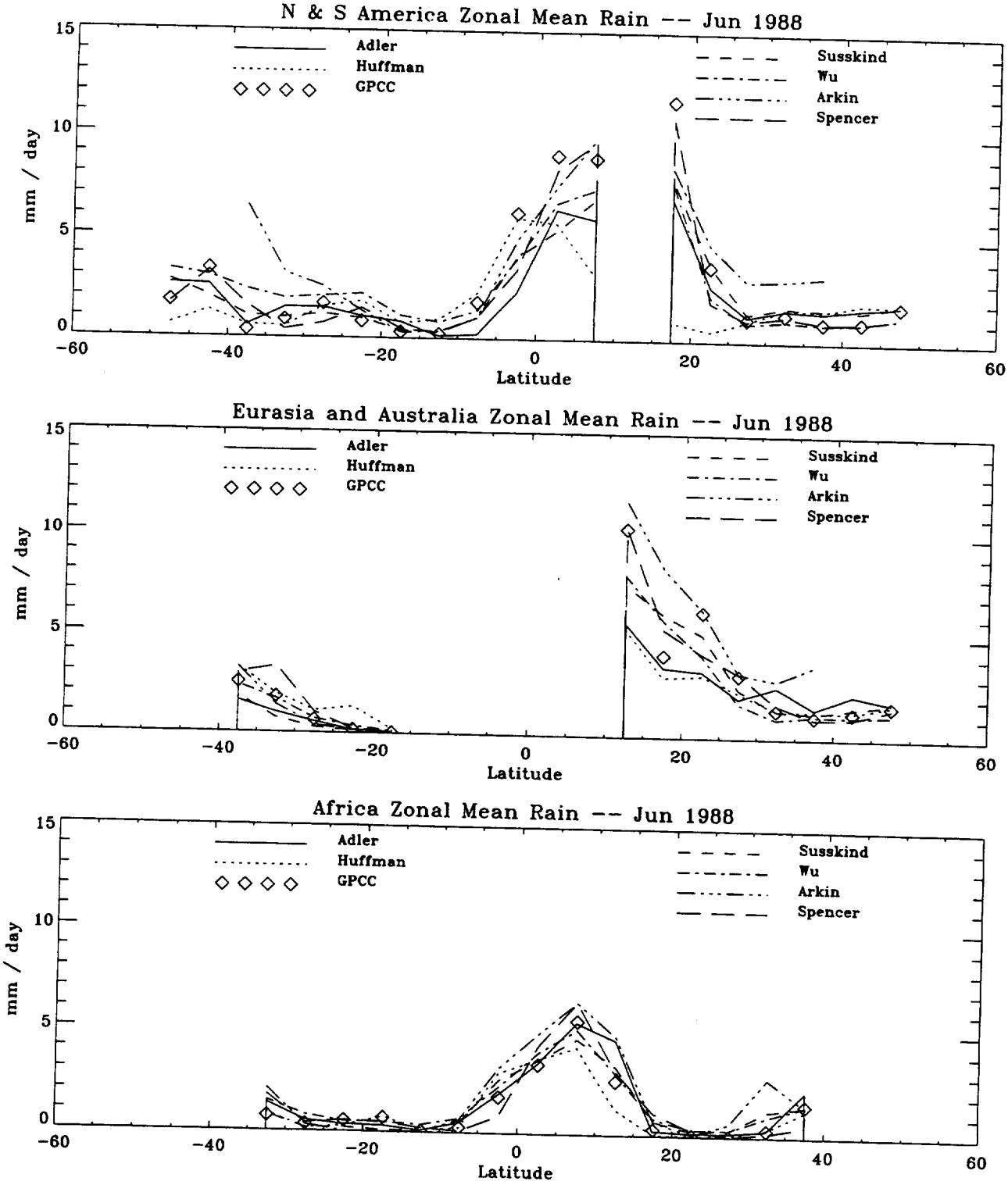

Figure 14.11: Zonal mean rain rate for the north and south American (upper panel), Australia and Eurasia (middle panel), and Africa land sector (lower panel) for June 1988.

ERRATA

Following is Figure 14.12, page 79 which was not printed.

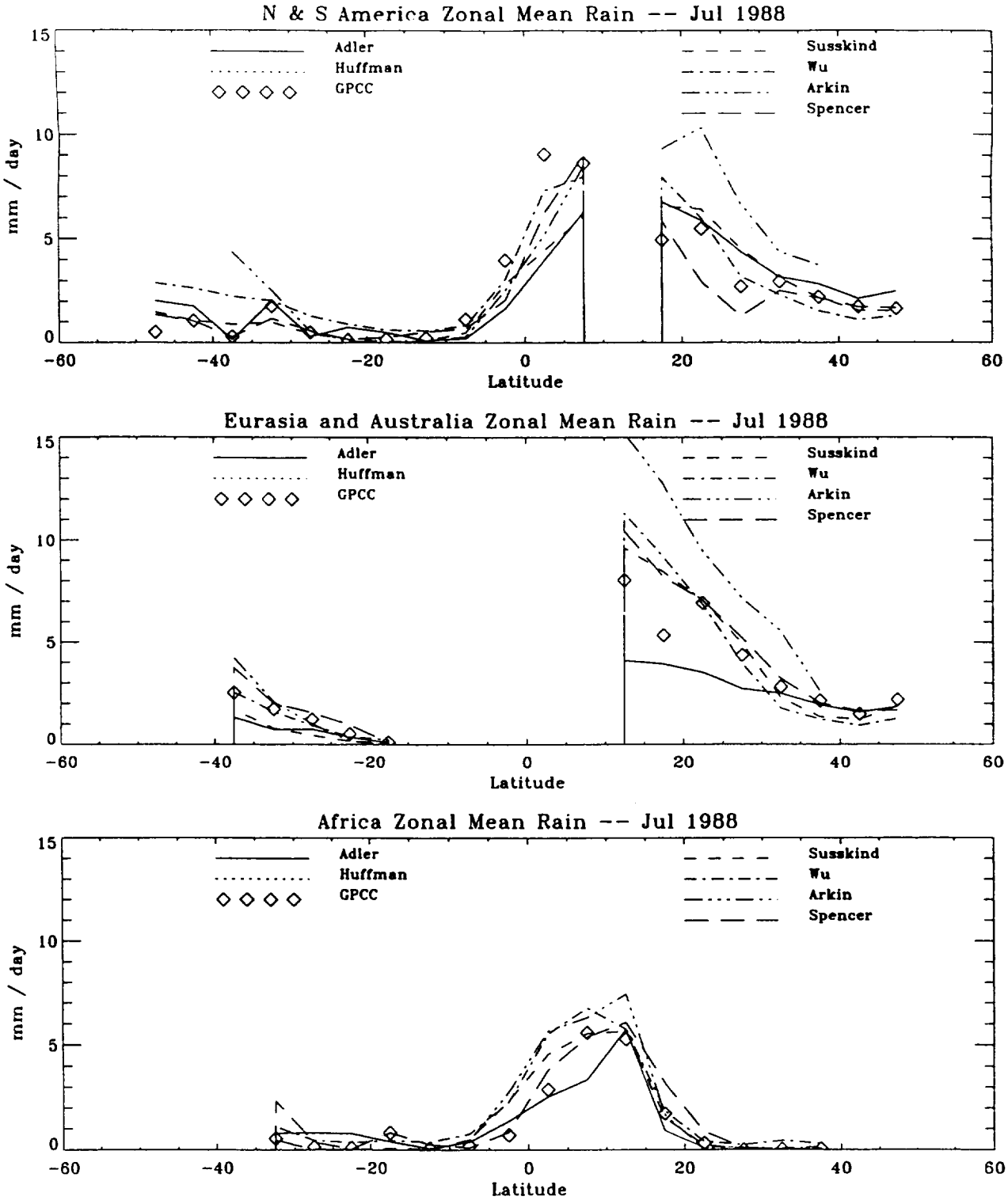

Figure 14.12: Zonal mean rain rate for the north and south American (upper panel). Australia and Eurasia (middle panel), and Africa land sector (lower panel) for July 1988.

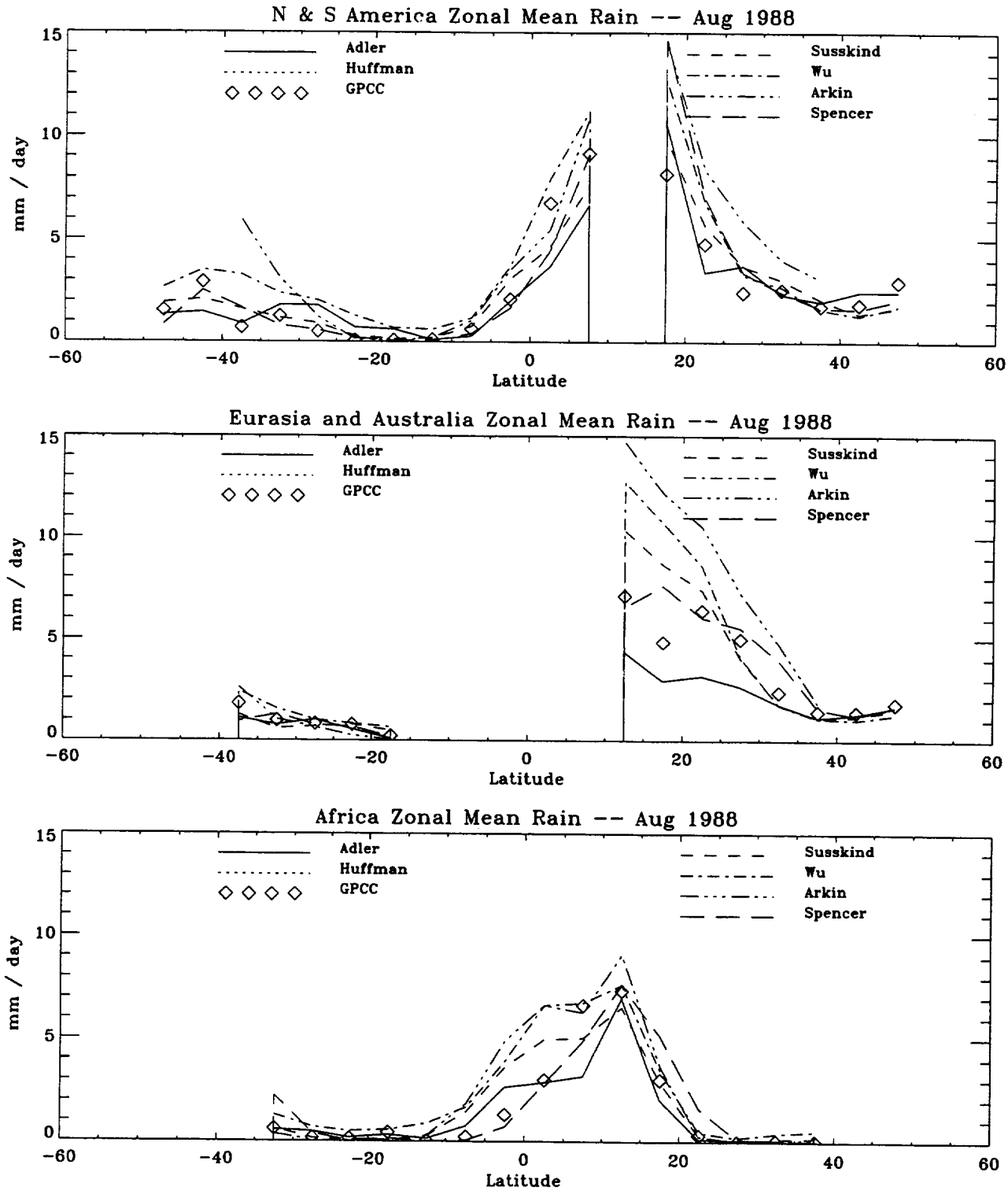

Figure 14.13: Zonal mean rain rate for the north and south American (upper panel), Australia and Eurasia (middle panel), and Africa land sector (lower panel) for August 1988.

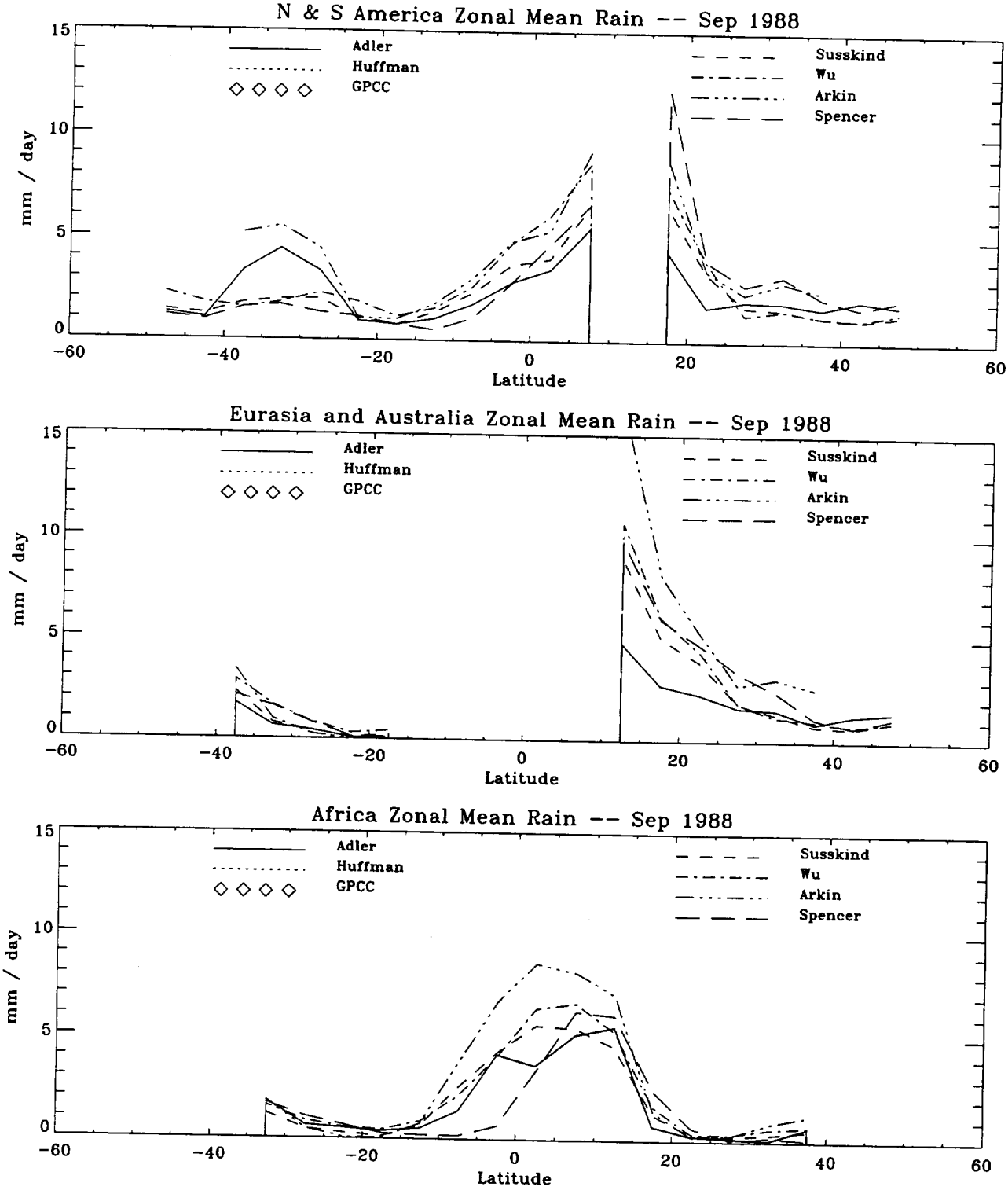

Figure 14.14: Zonal mean rain rate for the north and south American (upper panel), Australia and Eurasia (middle panel), and Africa land sector (lower panel) for September 1988.

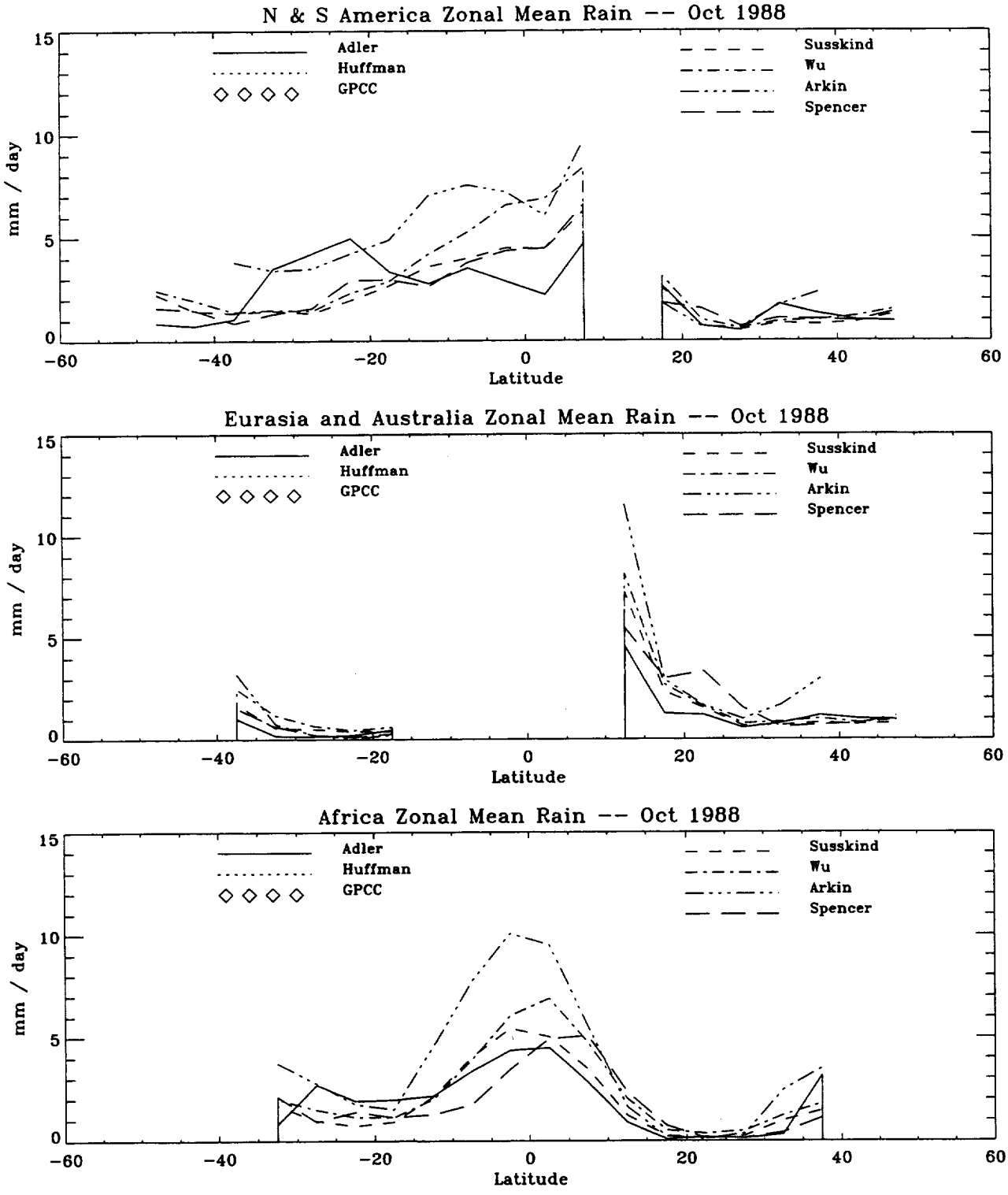

Figure 14.15: Zonal mean rain rate for the north and south American (upper panel), Australia and Eurasia (middle panel), and Africa land sector (lower panel) for October 1988.

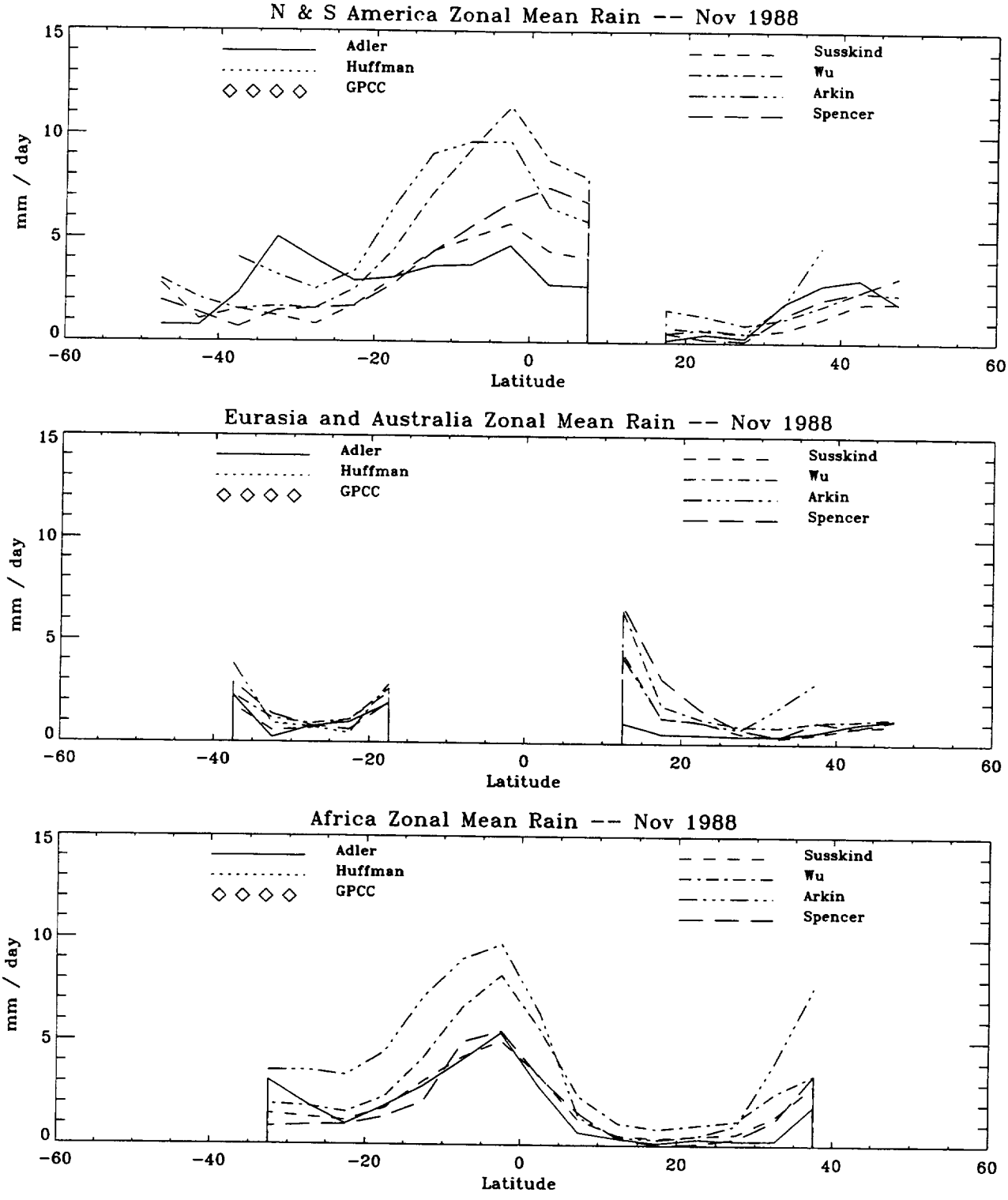

Figure 14.16: Zonal mean rain rate for the north and south American (upper panel), Australia and Eurasia (middle panel), and Africa land sector (lower panel) for November 1988.

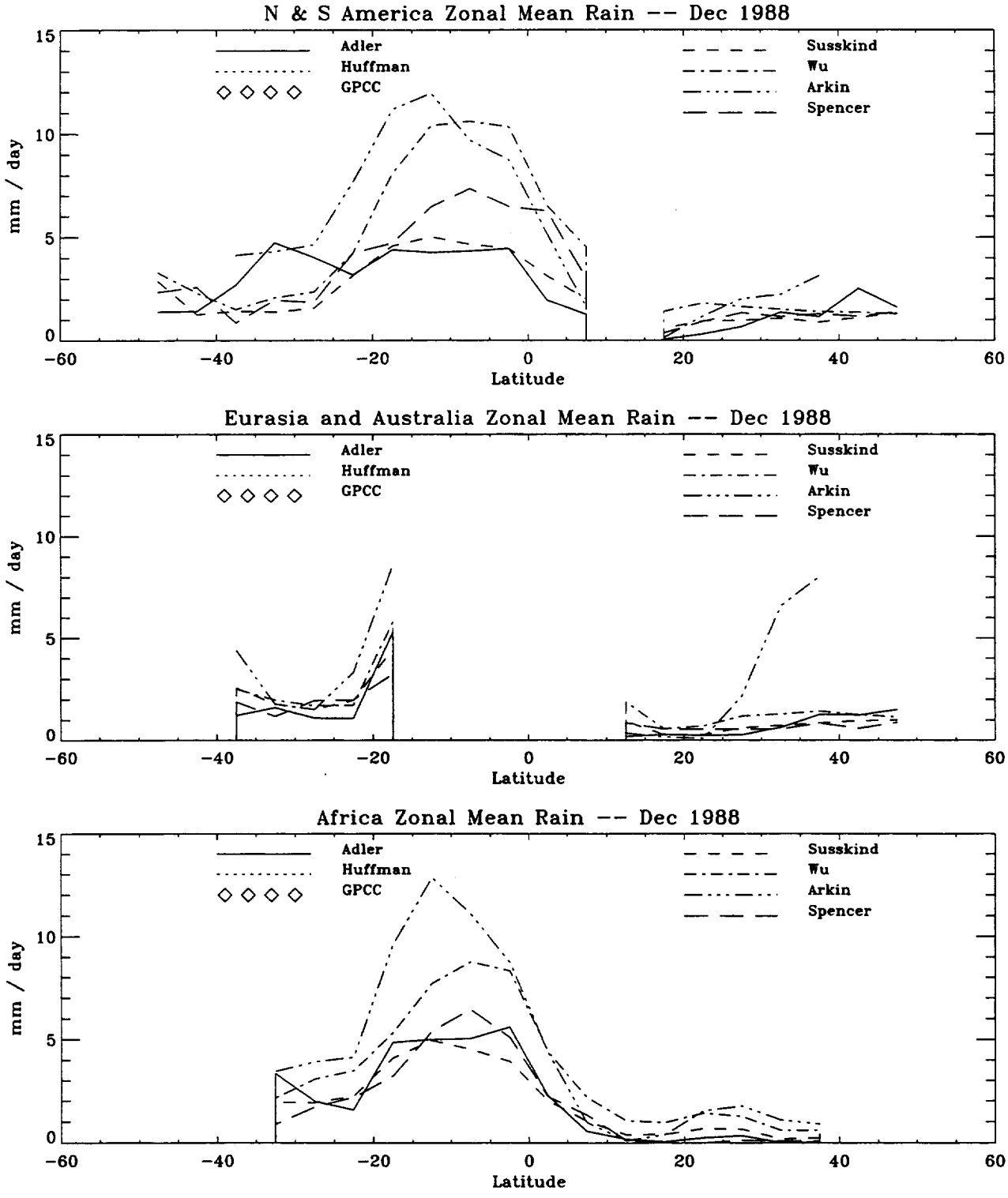

Figure 14.17: Zonal mean rain rate for the north and south American (upper panel), Australia and Eurasia (middle panel), and Africa land sector (lower panel) for December 1988.

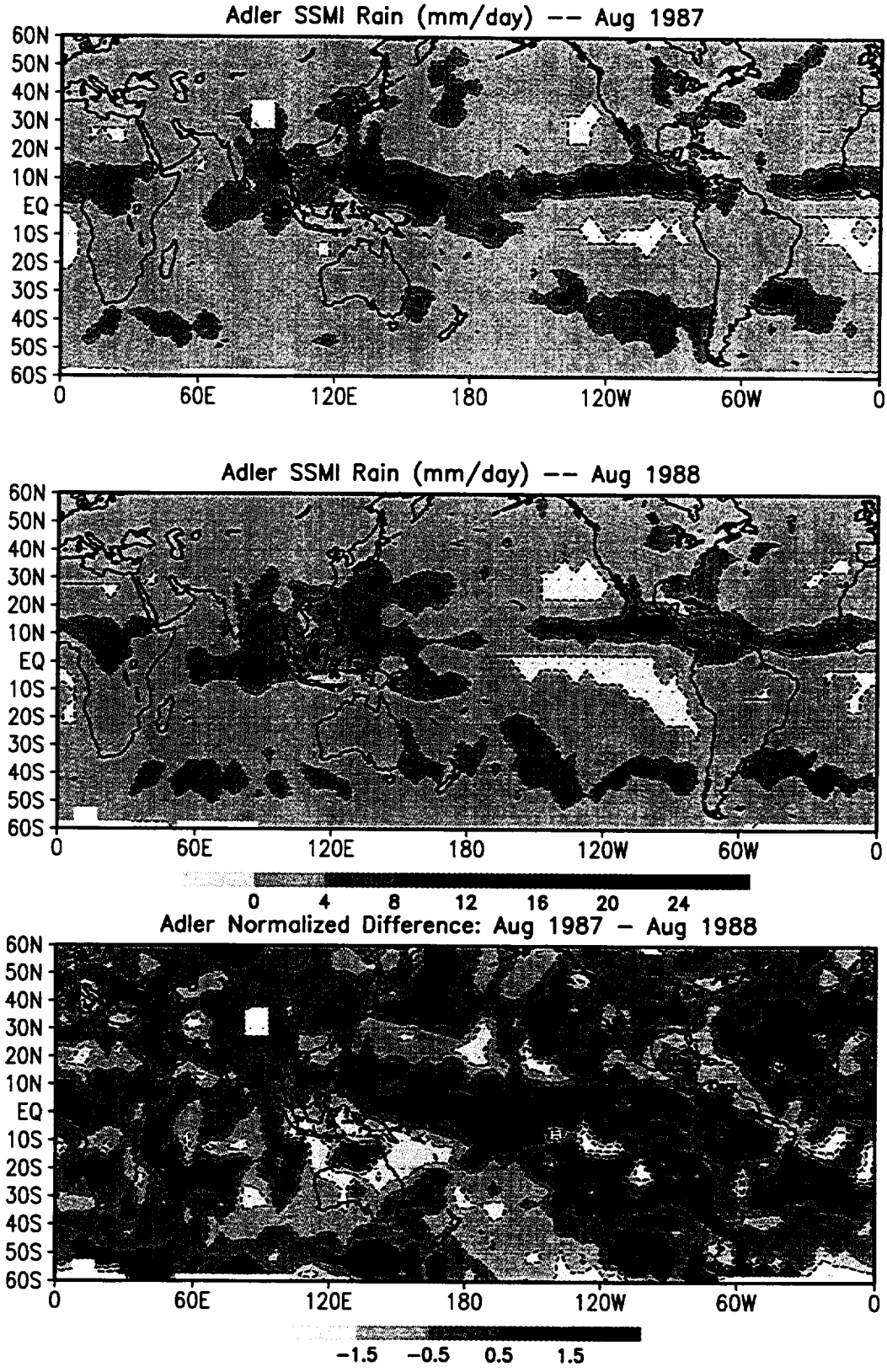

Figure 15.1: Rain rate distribution for August 1987 (upper panel), August 1988 (middle panel), and the normalized difference (difference between August 1987 and August 1988 divided by the average of these two months) (lower panel) for the algorithms of Adler.

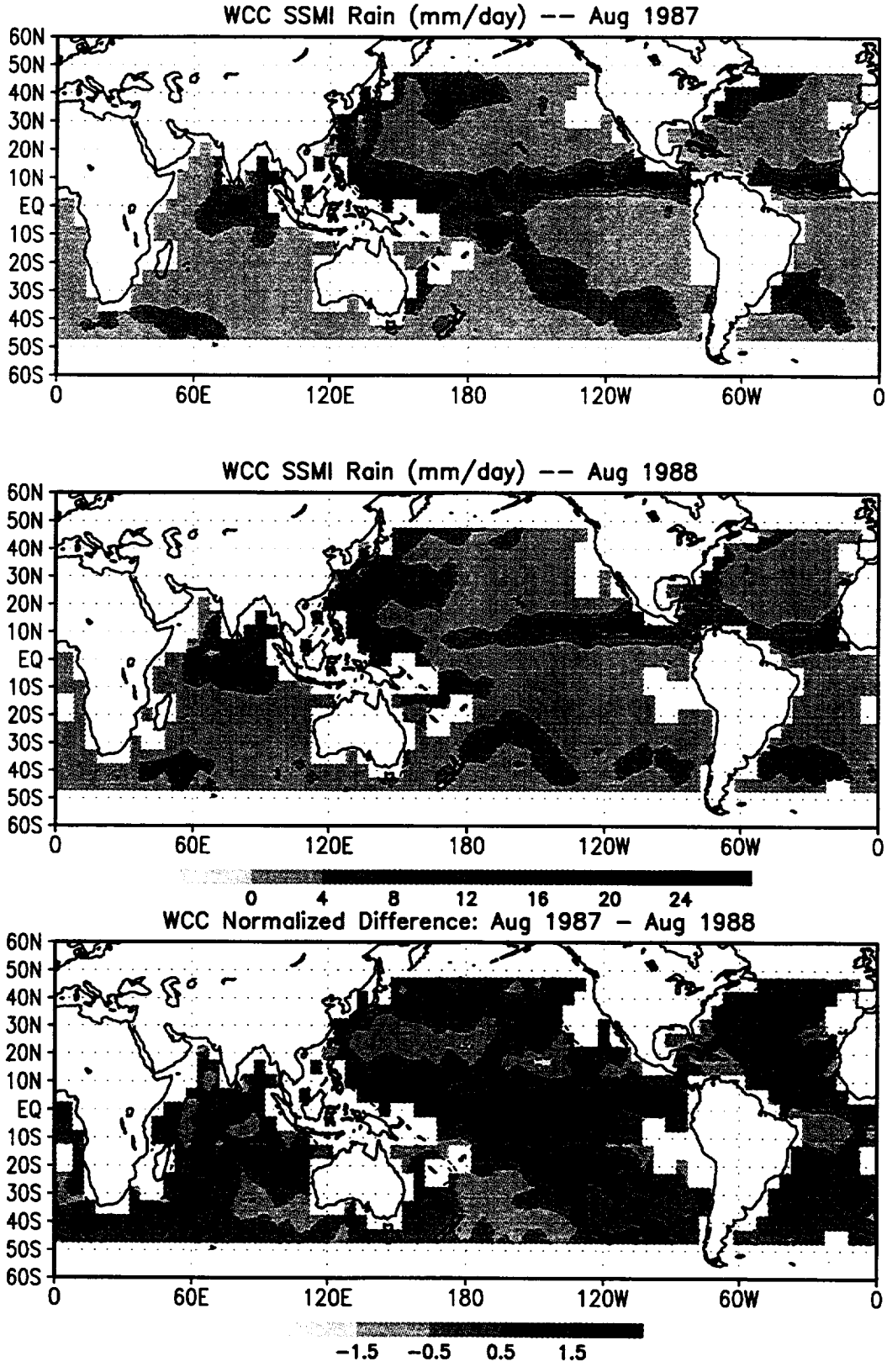

Figure 15.2: Rain rate distribution for August 1987 (upper panel), August 1988 (middle panel), and the normalized difference (difference between August 1987 and August 1988 divided by the average of these two months) (lower panel) for the algorithms of Chang.

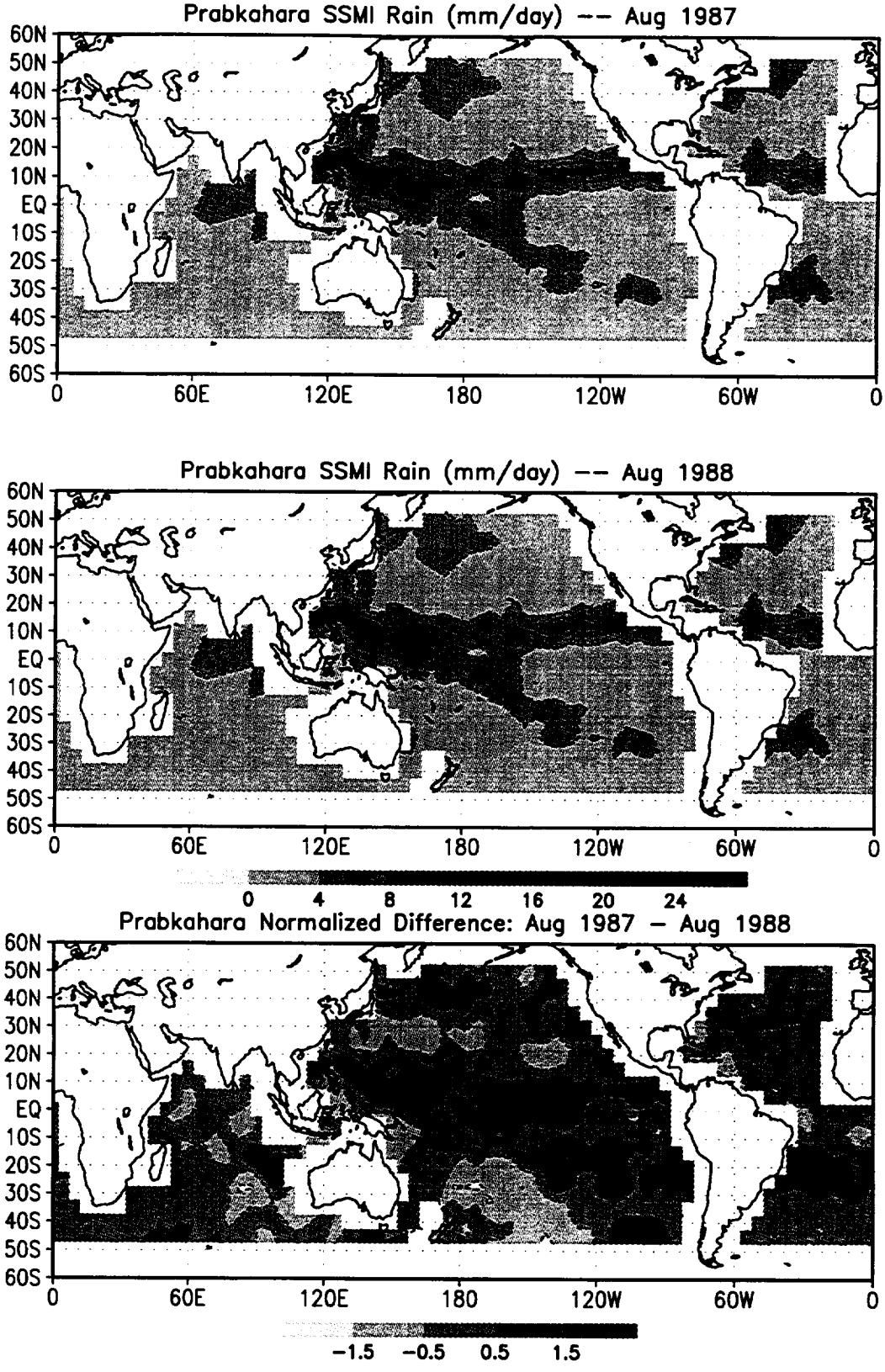

Figure 15.3: Rain rate distribution for August 1987 (upper panel), August 1988 (middle panel), and the normalized difference (difference between August 1987 and August 1988 divided by the average of these two months) (lower panel) for the algorithms of Prabhakara.

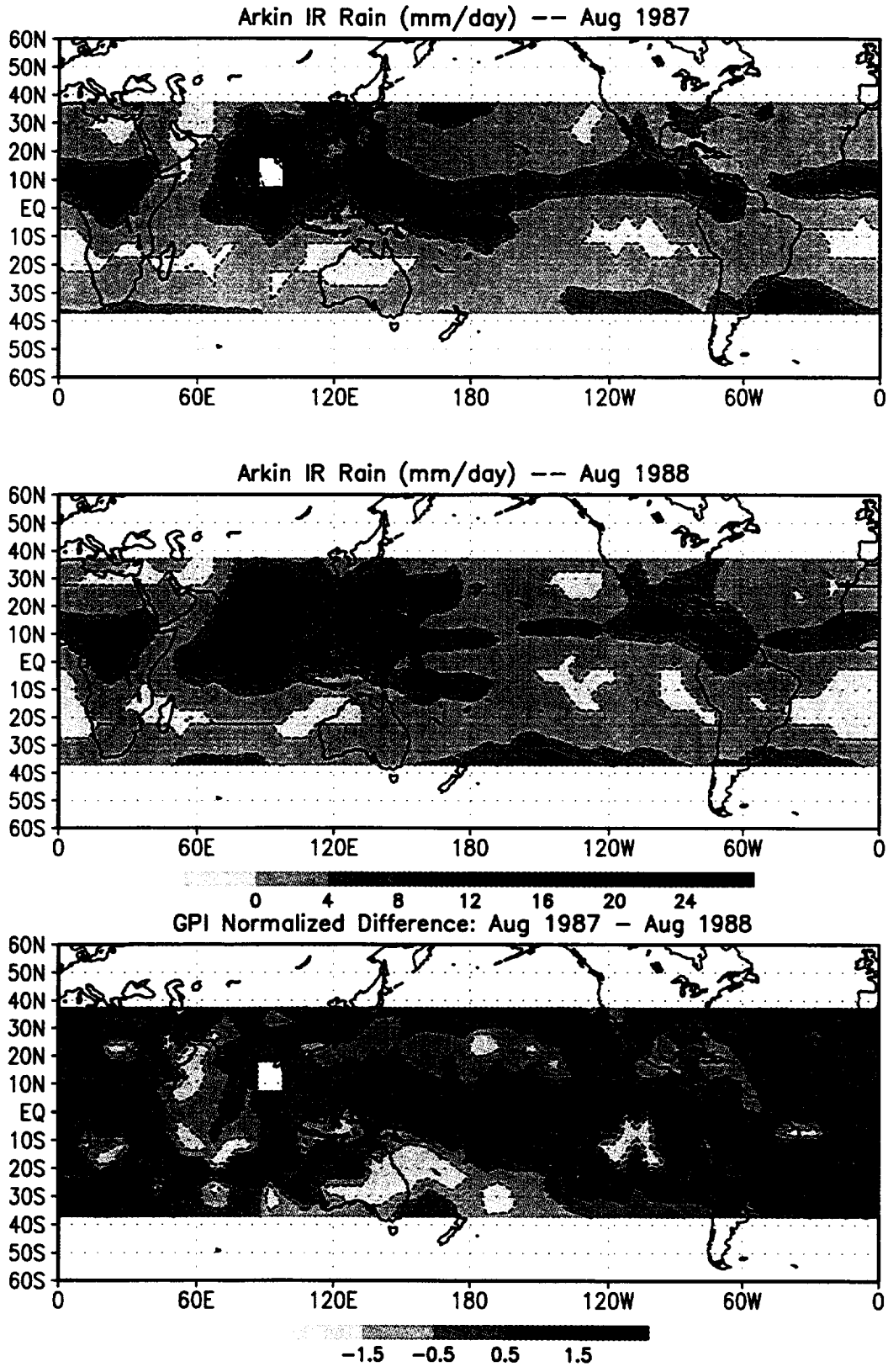

Figure 15.4: Rain rate distribution for August 1987 (upper panel), August 1988 (middle panel), and the normalized difference (difference between August 1987 and August 1988 divided by the average of these two months) (lower panel) for the algorithms of Arkin.

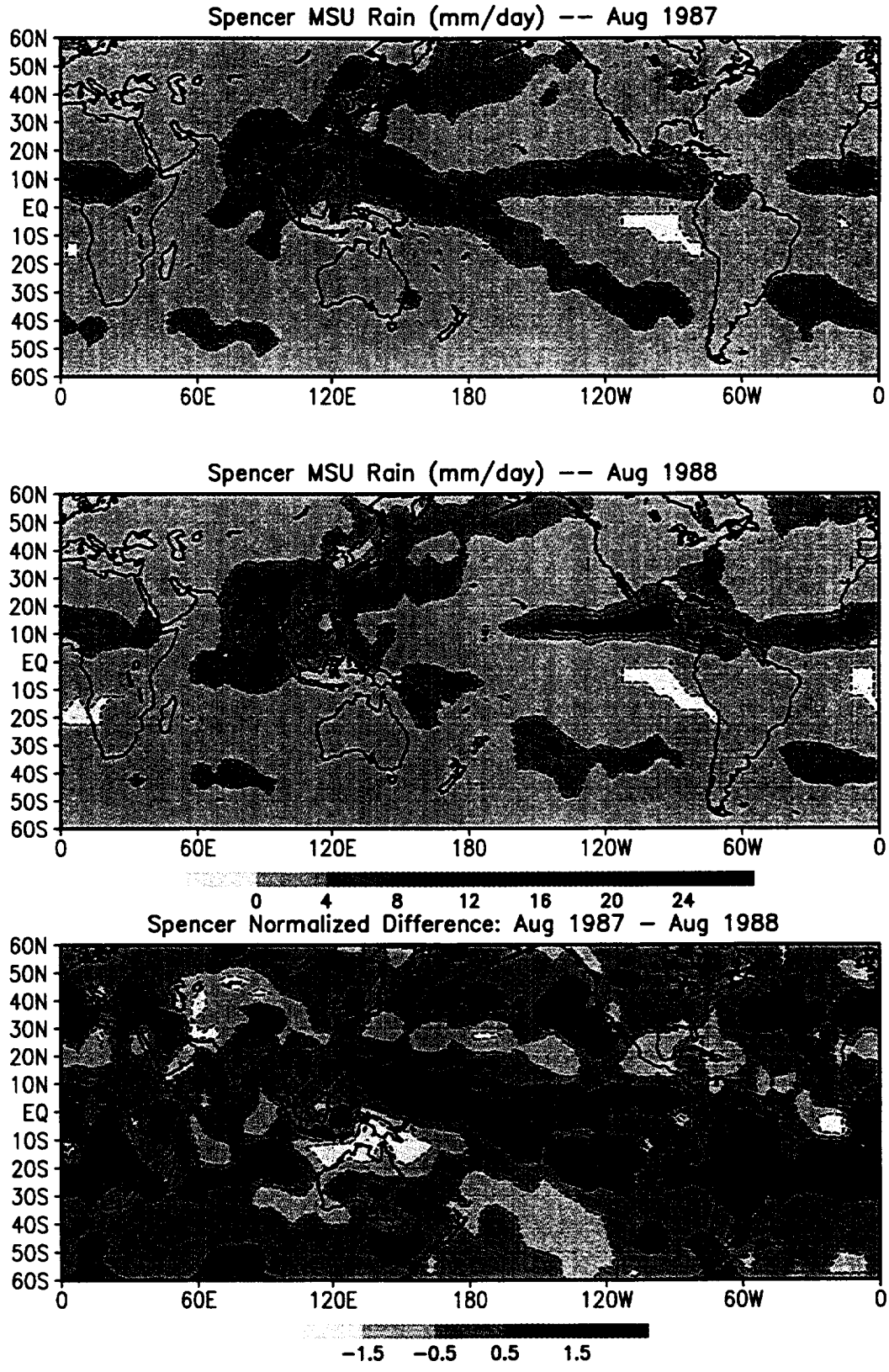

Figure 15.5: Rain rate distribution for August 1987 (upper panel), August 1988 (middle panel), and the normalized difference (difference between August 1987 and August 1988 divided by the average of these two months) (lower panel) for the algorithms of Spencer.

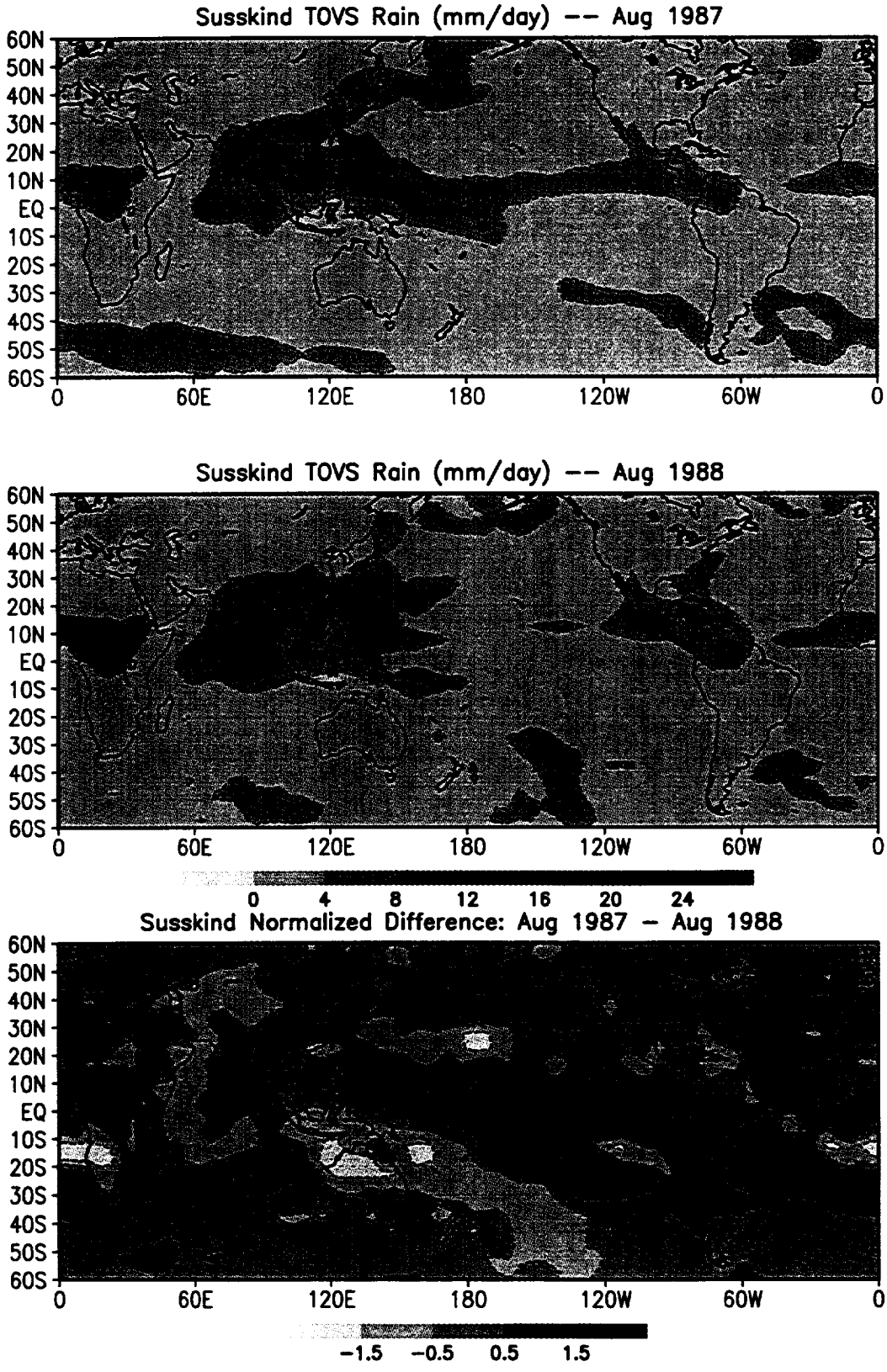

Figure 15.6: Rain rate distribution for August 1987 (upper panel), August 1988 (middle panel), and the normalized difference (difference between August 1987 and August 1988 divided by the average of these two months) (lower panel) for the algorithms of Susskind.

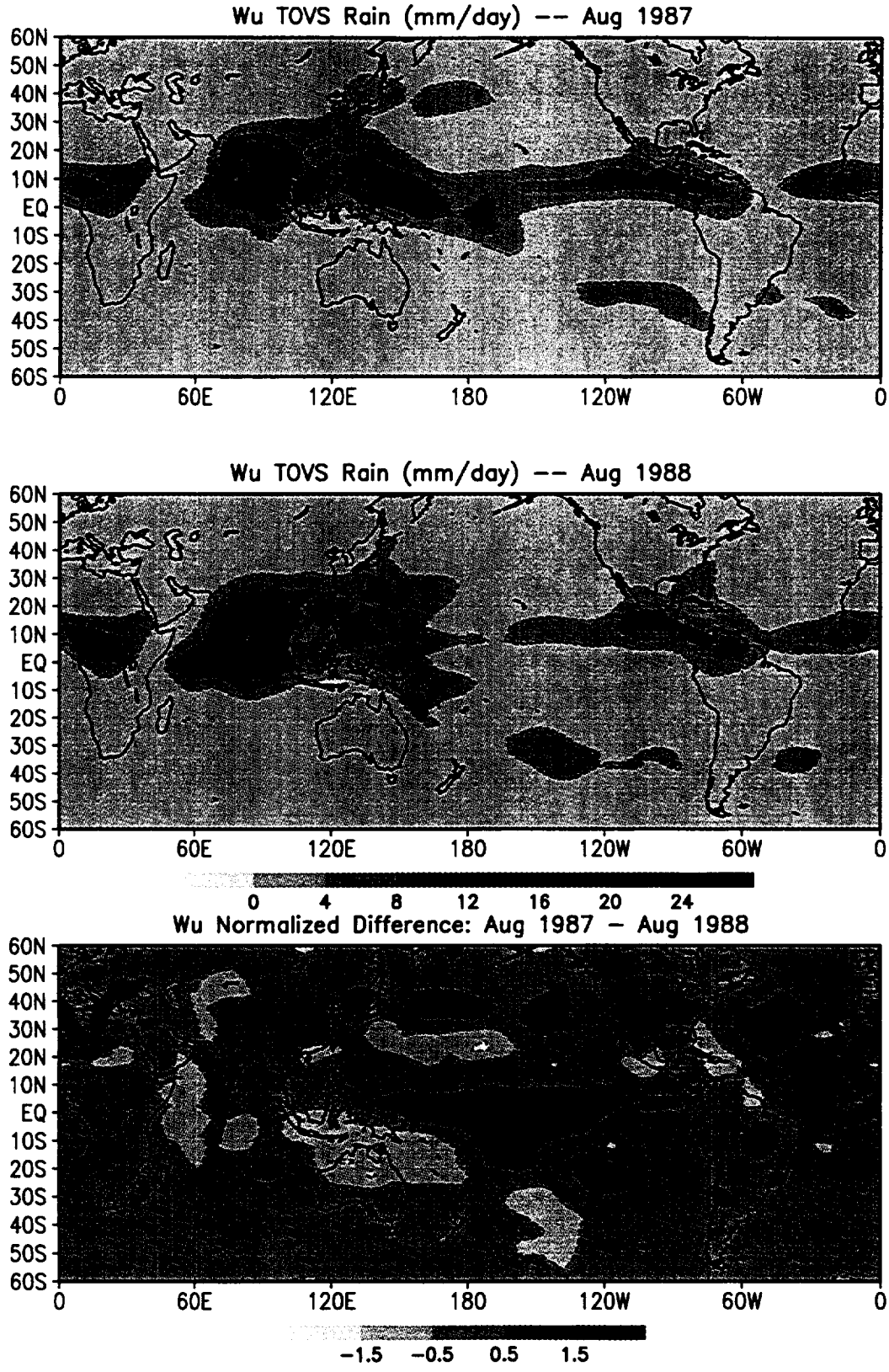

Figure 15.7: Rain rate distribution for August 1987 (upper panel), August 1988 (middle panel), and the normalized difference (difference between August 1987 and August 1988 divided by the average of these two months) (lower panel) for the algorithms of Wu.

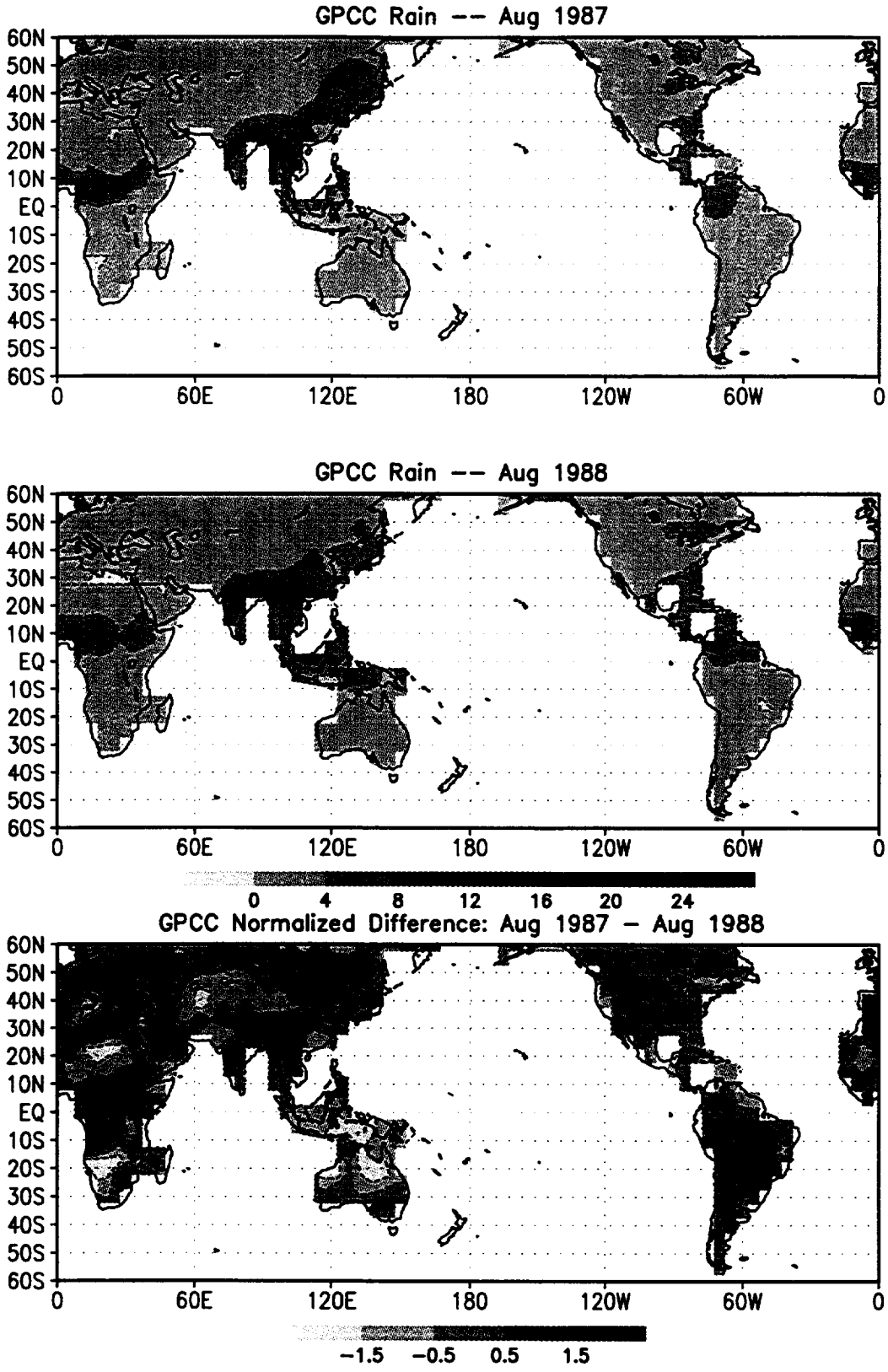

Figure 15.8: Rain rate distribution for August 1987 (upper panel), August 1988 (middle panel), and the normalized difference (difference between August 1987 and August 1988 divided by the average of these two months) (lower panel) for the algorithms of GPCC.

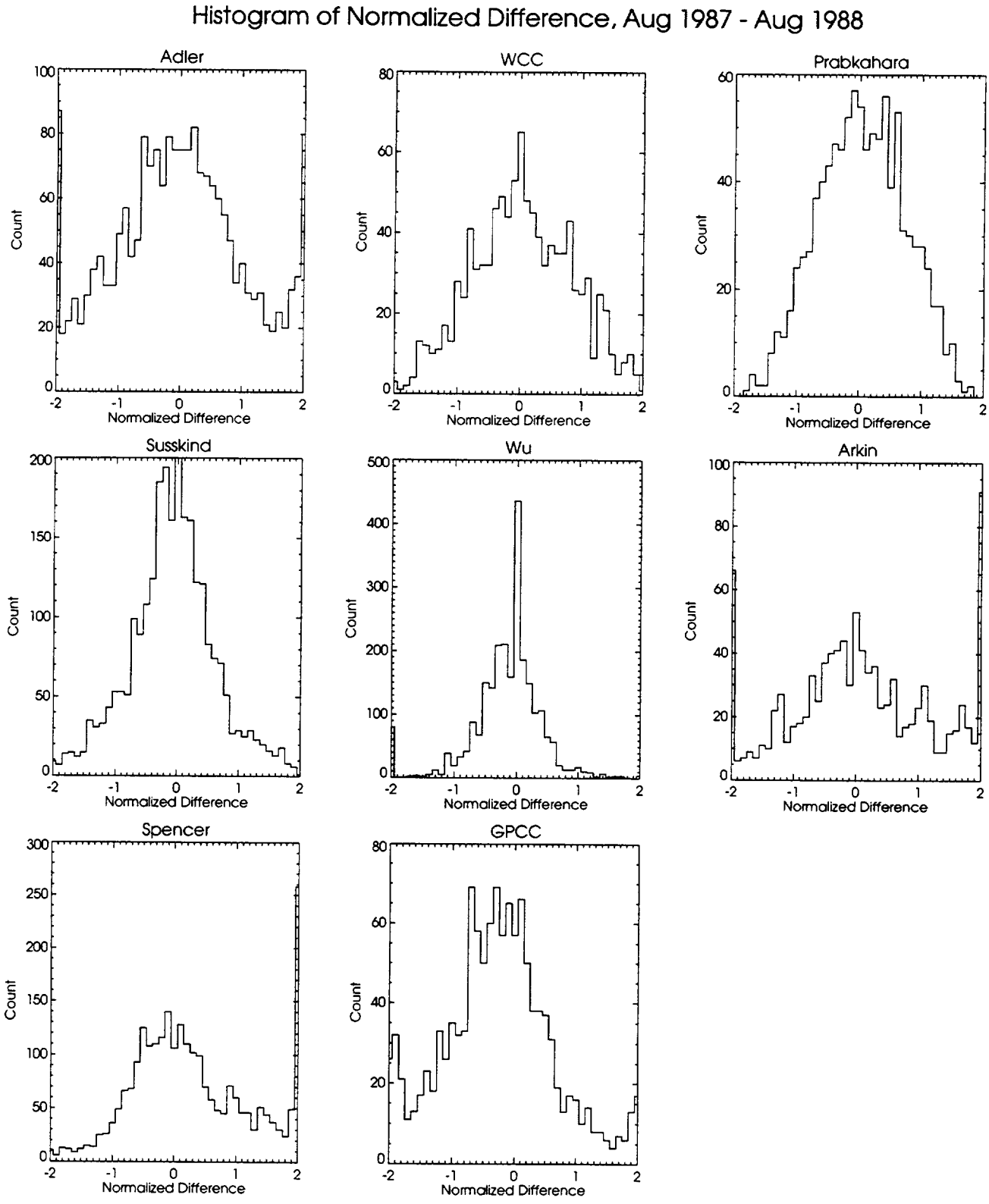

Figure 16: Histograms of the normalized difference for Adler, Chang, Prabhakara, Arkin, Spencer, Susskind, Wu, and GPCC.

Appendix A: Histogram of Rain Rate for All Algorithms															
Adler	Max	Min	ntot	nd	Bin 1	Bin 2	Bin 3	Bin 4	Bin 5	Bin 6	Bin 7	Bin 8	Bin 9	Bin 10	Bin 11
8708	21.9	0	2135	0	1468	363	151	71	41	19	11	6	3	1	1
8709	22.1	0	2095	1	1435	378	155	62	34	14	9	4	1	2	1
8710	18.3	0	1964	0	1181	397	179	90	54	28	14	13	3	4	1
8711	24.9	0	1870	0	1312	319	117	69	25	16	6	5	0	0	1
8712	0	0	0	0	0	0	0	0	0	0	0	0	0	0	0
8801	25.1	0	1874	1	1332	286	132	55	36	16	10	2	2	2	1
8802	17.5	0	1880	2	1156	341	155	94	53	32	19	17	11	1	1
8803	28.4	0	1901	0	1378	337	127	36	14	6	2	0	0	0	1
8804	21	0	1919	0	1207	371	171	92	43	20	8	3	2	1	1
8805	18.4	0	2005	0	1188	349	232	127	49	30	17	4	7	1	1
8806	27.6	0	2084	0	1467	374	157	52	21	8	1	1	1	1	1
8807	18.9	0	2112	0	1291	426	185	117	48	16	15	8	3	2	1
8808	23.3	0	2122	0	1463	390	152	67	23	14	7	3	2	0	1
8809	17.9	0	2101	0	1319	363	205	106	48	29	15	7	6	2	1
8810	20.1	0	1954	0	1216	364	203	84	45	21	12	4	4	0	1
8811	24.6	0	1843	0	1269	303	137	84	26	15	7	1	0	0	1
8812	20.6	0	1846	0	1190	303	174	78	53	25	6	7	5	4	1
Chang															
8708	24.7	0	1033	0	522	256	126	67	22	19	13	6	0	1	1
8709	29.9	0	1029	1	585	279	87	36	31	5	2	0	1	2	1
8710	20.5	0	1014	0	420	257	157	72	36	28	24	10	6	3	1
8711	22.6	0	1029	0	475	259	145	60	43	22	9	7	6	2	1
8712	0	0	0	0	0	0	0	0	0	0	0	0	0	0	0
8801	28.6	0	998	1	590	214	107	45	18	10	6	5	1	1	1
8802	29.9	0	1026	1	609	232	99	37	27	17	3	1	0	0	1
8803	27.6	0	1026	0	524	281	133	45	23	12	3	1	3	0	1
8804	20.2	0	1033	1	436	279	148	91	40	12	11	7	4	4	1
8805	21.3	0	1026	0	421	282	147	76	52	28	10	6	3	0	1
8806	24.4	0	1023	0	480	300	124	54	31	15	11	6	0	1	1
8807	17.2	0	1027	0	408	242	142	96	54	38	16	13	8	9	1
8808	28	0	1031	0	579	279	98	35	20	10	7	1	1	0	1
8809	22.5	0	1007	1	492	259	105	79	29	21	7	8	2	4	1
8810	27	0	1016	0	577	215	114	58	34	13	1	2	0	1	1
8811	23.4	0	1016	0	513	228	131	85	28	11	10	3	4	2	1
8812	26.1	0	1015	2	535	250	124	63	20	14	2	3	3	0	1
Kummerow															
8708	22.4	0	1440	0	939	244	145	52	26	14	9	2	7	1	1
8709	22.3	0	1440	0	941	269	128	49	22	17	8	3	1	1	1
8710	28.2	0	1425	15	962	286	101	45	18	7	2	1	0	2	1
8711	25.7	0	1412	28	878	323	117	40	20	13	11	3	1	5	1
8712	0	0	0	0	0	0	0	0	0	0	0	0	0	0	0
8801	0	0	0	0	0	0	0	0	0	0	0	0	0	0	0
8802	28.6	0	1373	67	884	289	114	38	19	7	8	4	6	3	1
8803	28.4	0	1397	43	866	324	116	46	12	8	6	9	5	4	1
8804	28	0	1428	12	904	304	142	32	16	14	6	3	4	2	1
8805	27	0	1437	3	913	323	131	47	9	8	3	1	1	0	1
8806	28.2	0	1438	2	980	302	109	28	13	3	1	1	0	0	1
8807	21	0	1438	2	887	282	144	68	27	12	8	6	3	0	1
8808	0	0	0	0	0	0	0	0	0	0	0	0	0	0	0
8809	0	0	0	0	0	0	0	0	0	0	0	0	0	0	0
8810	0	0	0	0	0	0	0	0	0	0	0	0	0	0	0
8811	0	0	0	0	0	0	0	0	0	0	0	0	0	0	0
8812	0	0	0	0	0	0	0	0	0	0	0	0	0	0	0

Huffman															
8708	23.9	0	2592	0	1899	378	152	74	42	23	10	8	4	1	1
8709	22	0	2592	0	1831	432	152	69	45	29	16	14	2	1	1
8710	27	0	2591	1	2013	331	135	52	31	18	6	3	1	0	1
8711	27.7	0	2592	0	2044	313	130	51	30	11	8	2	2	0	1
8712	0	0	0	0	0	0	0	0	0	0	0	0	0	0	0
8801	0	0	0	0	0	0	0	0	0	0	0	0	0	0	0
8802	23.7	0	2592	0	1968	326	150	71	34	25	11	3	1	2	1
8803	18.9	0	2592	0	1942	337	150	81	32	20	13	10	3	3	1
8804	20.1	0	2592	0	1833	382	192	82	41	32	20	6	1	2	1
8805	23.4	0	2592	0	1926	405	152	64	23	11	4	3	3	0	1
8806	22.1	0	2592	0	1841	370	187	91	51	21	18	6	4	2	1
8807	0	0	0	0	0	0	0	0	0	0	0	0	0	0	0
8808	0	0	0	0	0	0	0	0	0	0	0	0	0	0	0
8809	0	0	0	0	0	0	0	0	0	0	0	0	0	0	0
8810	0	0	0	0	0	0	0	0	0	0	0	0	0	0	0
8811	0	0	0	0	0	0	0	0	0	0	0	0	0	0	0
8812	0	0	0	0	0	0	0	0	0	0	0	0	0	0	0
Prabhakara															
8708	19.9	0	1000	0	445	294	128	58	39	8	12	7	3	5	1
8709	26.4	0	1000	0	543	260	115	45	22	7	2	2	1	2	1
8710	21.1	0	1000	0	420	276	138	87	39	25	9	4	1	0	1
8711	20.4	0	1000	0	394	288	164	71	36	19	13	9	4	1	1
8712	0	0	0	0	0	0	0	0	0	0	0	0	0	0	0
8801	28.3	0	999	1	547	283	91	43	16	6	4	6	1	1	1
8802	28.6	0	998	2	554	263	87	46	31	12	1	3	0	0	1
8803	24.7	0	998	2	460	299	128	58	29	11	7	5	0	0	1
8804	26.3	0	999	1	496	304	120	37	24	10	3	2	2	0	1
8805	19.8	0	998	2	388	293	137	81	46	39	6	2	4	1	1
8806	22.9	0	999	1	513	273	117	46	28	11	8	1	0	1	1
8807	19.4	0	998	2	461	276	112	67	38	25	14	2	1	1	1
8808	23.6	0	1000	0	548	257	109	49	21	10	3	2	0	0	1
8809	20.4	0	1000	0	482	241	121	70	56	15	8	2	3	1	1
8810	27.2	0	999	1	571	229	112	54	20	6	4	2	0	0	1
8811	29.6	0	999	1	567	259	108	39	15	4	3	2	1	0	1
8812	25.6	0	1000	0	520	265	128	43	24	7	6	3	2	1	1
Spencer															
8708	15.4	0	2592	0	1402	555	293	155	85	49	20	18	11	3	1
8709	18	0	2592	0	1555	482	278	141	69	40	24	2	0	0	1
8710	16.5	0	2592	0	1465	519	284	175	71	41	27	6	3	0	1
8711	18.3	0	2592	0	1511	578	258	126	69	34	9	3	2	1	1
8712	15.4	0	2592	0	1487	433	285	157	90	57	48	19	11	4	1
8801	14.8	0	2592	0	1460	449	311	158	87	58	33	21	9	5	1
8802	17.8	0	2592	0	1602	445	252	130	68	48	28	14	3	1	1
8803	19.5	0	2592	0	1632	481	275	101	58	30	12	1	0	1	1
8804	16.8	0	2591	1	1540	494	277	151	71	26	18	9	3	1	1
8805	14.8	0	2592	0	1521	453	302	162	67	37	29	12	3	5	1
8806	17.7	0	2592	0	1581	531	247	115	64	27	12	7	5	2	1
8807	15.6	0	2592	0	1440	515	287	156	92	44	21	18	11	7	1
8808	18.1	0	2592	0	1499	570	298	115	55	19	17	8	6	4	1
8809	15.7	0	2592	0	1421	545	294	141	85	40	27	21	11	6	1
8810	16.1	0	2592	0	1525	515	266	122	77	52	20	8	5	1	1
8811	17.4	0	2592	0	1554	480	284	142	76	24	19	7	2	3	1
8812	17.9	0	2592	0	1530	514	290	132	69	30	20	4	1	1	1

Arkin															
8708	24.5	0	1151	1	645	188	111	76	64	36	19	7	1	3	1
8709	24.3	0	1152	0	618	204	132	90	53	31	20	0	2	1	1
8710	24.4	0	1152	0	610	216	152	95	44	23	7	3	0	1	1
8711	18.7	0	1152	0	474	227	183	103	55	43	32	22	9	3	1
8712	22.8	0	1152	0	606	196	131	77	57	37	26	7	10	4	1
8801	22.3	0	1152	0	585	221	129	65	58	40	27	12	8	6	1
8802	21.5	0	1152	0	609	206	111	65	44	43	35	18	12	8	1
8803	22.5	0	1152	0	591	205	136	90	71	26	13	11	2	6	1
8804	18.6	0	1152	0	477	236	157	100	84	42	29	13	8	5	1
8805	26.8	0	1152	0	611	217	171	93	40	12	3	2	1	1	1
8806	25.2	0	1152	0	612	203	169	102	37	19	5	2	1	1	1
8807	23.3	0	1152	0	629	178	123	85	55	38	25	8	6	4	1
8808	21.3	0	1152	0	620	172	116	89	60	35	20	20	12	7	1
8809	23.9	0	1152	0	635	192	133	75	55	27	21	4	6	3	1
8810	26.4	0	1152	0	660	220	130	67	26	28	9	5	5	1	1
8811	29.5	0	1150	2	683	258	109	48	30	5	8	4	2	2	1
8812	25.7	0	1152	0	636	208	114	83	53	37	17	2	1	0	1
Susskind															
8708	13.7	0	2592	0	1323	556	313	205	87	56	25	16	8	2	1
8709	11.9	0	2592	0	1179	515	383	274	112	68	36	13	8	3	1
8710	13	0	2592	0	1256	495	418	191	103	66	39	13	9	1	1
8711	11	0	2592	0	1117	534	412	176	124	89	57	52	19	11	1
8712	15.1	0	2592	0	1359	545	322	158	105	50	26	18	6	2	1
8801	13.9	0	2592	0	1296	474	401	188	108	63	26	23	10	2	1
8802	14.1	0	2592	0	1337	511	342	176	98	48	36	21	18	4	1
8803	10.7	0	2592	0	1099	492	312	261	209	102	53	31	22	10	1
8804	12.2	0	2592	0	1121	583	362	255	142	79	31	14	4	0	1
8805	14	0	2592	0	1287	517	389	217	105	53	14	7	1	1	1
8806	13.9	0	2592	0	1308	514	395	194	87	54	21	15	2	1	1
8807	13.3	0	2592	0	1266	545	444	132	75	59	36	18	10	6	1
8808	13.7	0	2592	0	1288	568	362	188	67	57	27	21	8	5	1
8809	12	0	2592	0	1249	486	378	234	85	58	43	28	23	7	1
8810	17.3	0	2592	0	1487	599	289	126	44	23	13	6	3	1	1
8811	15.2	0	2592	0	1404	579	296	147	93	30	20	7	9	6	1
8812	15.4	0	2592	0	1417	533	321	146	72	46	28	22	4	2	1
Wu															
8708	16.5	0	2592	0	1361	727	258	76	57	55	36	13	6	2	1
8709	13.3	0	2592	0	1150	668	465	131	60	47	52	13	2	3	1
8710	13.1	0	2592	0	1172	738	403	105	69	54	35	10	4	1	1
8711	13.5	0	2592	0	1141	861	299	106	72	44	40	19	8	1	1
8712	15.6	0	2592	0	1395	793	171	69	65	34	28	18	10	8	1
8801	15	0	2592	0	1320	783	238	79	65	36	28	28	12	2	1
8802	14.3	0	2592	0	1306	832	178	101	58	32	29	20	26	9	1
8803	14.7	0	2592	0	1263	830	235	102	81	34	22	10	11	3	1
8804	13.1	0	2592	0	1159	801	332	113	56	54	34	27	13	2	1
8805	15.5	0	2592	0	1223	705	370	135	77	54	14	8	3	2	1
8806	13.6	0	2592	0	1283	642	356	105	98	67	21	15	2	2	1
8807	14.3	0	2592	0	1292	662	321	101	57	69	38	26	14	11	1
8808	16.7	0	2592	0	1370	741	210	91	64	39	28	23	20	5	1
8809	14.7	0	2592	0	1304	709	321	71	62	51	34	21	9	9	1
8810	16	0	2592	0	1366	817	208	84	44	34	16	12	6	4	1
8811	20	0	2592	0	1516	764	147	66	38	27	14	11	3	5	1
8812	18.7	0	2592	0	1572	641	172	74	44	39	23	11	13	2	1

First column shows the year and month yymm

Second column shows the maximum for the month in mm/day (max)

Third column shows the minimum rain rate in mm/day (min)

Fourth column shows the total number of pixels excluding pixels larger than 30 mm/day (ntot)

Fifth column shows the number of pixels in excess of 30 mm/day (nd)

Sixth -sixteenth columns show the histogram

Bin 1 = number of pixels between min and min + (max-min)/10, ...,

Bin 10 = number between max - (max-min)/10 and max

REPORT DOCUMENTATION PAGE

Form Approved
OMB No. 0704-0188

1. AGENCY USE ONLY *(Leave blank)*

2. REPORT DATE
August 1997

3. REPORT TYPE AND DATES COVERED
Technical Memorandum

4. TITLE AND SUBTITLE
Technical Report Series on Global Modeling and Data Assimilation Volume 12–
Comparison of Satellite Global Rainfall Algorithms

5. FUNDING NUMBERS
C - NAS5-32332
Code 974/913

6. AUTHOR(S)
Alfred T. C. Chang and Long S. Chiu

7. PERFORMING ORGANIZATION NAME(S) AND ADDRESS (ES)
Hydrological Sciences Branch
Climate and Radiation Branch
Goddard Space Flight Center
Greenbelt, Maryland

8. PEFORMING ORGANIZATION REPORT NUMBER
97B00055

9. SPONSORING / MONITORING AGENCY NAME(S) AND ADDRESS (ES)
National Aeronautics and Space Administration
Washington, DC 20546-0001

10. SPONSORING / MONITORING AGENCY REPORT NUMBER
TM-104606, Vol.12

11. SUPPLEMENTARY NOTES

12a. DISTRIBUTION / AVAILABILITY STATEMENT
Unclassified - Unlimited
Subject Category 46

Availability: NASA CASI (301) 621-0390.

12b. DISTRIBUTION CODE

13. ABSTRACT *(Maximum 200 words)*

Seventeen months of rainfall data (August 1987–December 1988) from nine satellite rainfall algorithms (Adler, Chang, Kummerow, Prabhakara, Huffman, Spencer, Susskind, and Wu) were analyzed to examine the uncertainty of satellite-derived rainfall estimates. The variability among algorithms, measured as the standard deviation computed from the ensemble of algorithms, shows regions of high algorithm variability tend to coincide with regions of high rain rates. Histograms of pattern correlation (PC) between algorithms suggest a bimodal distribution, with separation at a PC-value of about 0.85. Applying this threshold as a criteria for similarity, our analyses show that algorithms using the same sensor or satellite input tend to be similar, suggesting the dominance of sampling errors in these satellite estimates.

14. SUBJECT TERMS
Arkins algorithm, pattern correlation (PC), El Nino Southern Oscillation, Adlers algorithm, t statistics

15. NUMBER OF PAGES
96

16. PRICE CODE

17. SECURITY CLASSIFICATION OF REPORT	18. SECURITY CLASSIFICATION OF THIS PAGE	19. SECURITY CLASSIFICATION OF ABSTRACT	20. LIMITATION OF ABSTRACT
Unclassified	Unclassified	Unclassified	UL